Electric Field Directed Colloidal Self-Assembly, Crystallization and Annealing with Biomimetic Structural Color

by

Tianyu Liu

A dissertation submitted in partial fulfillment
of the requirements for the degree of
Doctor of Philosophy
(Chemical Engineering)
in the University of Michigan
2025

Doctoral Committee:

Professor Michael J. Solomon, Chair
Professor Sharon C. Glotzer
Professor Jay L. Guo
Professor Ronald G. Larson

Tianyu Liu

tyliux@umich.edu

ORCID iD: 0000-0003-4836-2265

© Tianyu Liu 2025

Dedication

To my beloved mother Jingcan Xiao (肖敬灿) and father Zhaohui Liu (刘朝辉) for their unwavering support, encouragement, and love.

Acknowledgements

The completion of my dissertation marks a significant milestone in my life, one that would not have been possible without the support, guidance, and encouragement of many individuals.

First and foremost, I would like to express my deepest gratitude to my advisor, Professor Mike Solomon. Your expertise, patience, and unwavering support have been invaluable throughout this journey. Your insightful feedback on my research plans, manuscript drafts, and career development has pushed me to sharpen my thinking and bring this work to fruition. I have learned not only the skills necessary to become a professional scientist but also essential soft skills. Thank you for consistently and patiently guiding me through the various stages of my Ph.D. journey. I always felt your encouragement in trying new ideas, and your guidance in preparing for publications, presentations, job interviews, and applications has been invaluable. It has truly been my privilege to be your student over the past years.

I am also profoundly thankful to the members of my dissertation committee: Professor Sharon Glotzer, Professor Jay Guo, and Professor Ronald Larson. Your time, constructive criticism, and guidance have greatly enriched my research. Professor Glotzer provided opportunities for intergroup collaboration and valuable technical insights into my simulation work. Professor Guo offered deeper explanations of my research from an optics perspective. Professor Larson shared fundamental knowledge of fluids and soft materials through coursework and provided critical suggestions for my research.

To my colleagues and alumni in the Solomon Group, thank you for the stimulating discussions, camaraderie, and shared commitment to scholarship. The collaborative environment we built has been both inspiring and motivating. Tianyu Liu, who shares the same name as me, led me through a project and helped me learn more about the group. She also introduced me to people and assisted with my career planning. Peng-Kai Kao trained me on various lab equipment and provided insightful suggestions on my resume and interview skills. Chih-Mei Young helped with simulation modeling to better understand experimental systems, while Syahidah Mohd Khairi assisted in designing a smart circuit to automate our experiments. Keara Saud brought positivity and encouragement to the group, and Clémence Abriat shared valuable insights inside and outside the lab. I am also thankful to my labmates—Mahesh Ganesan, Joanne Beckwith, Rachael Hamilton, and Alice Sneha George—for fostering a friendly and supportive group environment.

I also extend my gratitude to my collaborators: Charlotte Zhao, and Timothy Moore from the Glotzer Group. I appreciated your valuable input during meetings and your insightful ideas that moved the project forward. It was a privilege to work with you. I would also like to thank my undergraduate researcher, Owen-Matthew Snyder, for your meaningful contributions and for trusting me as your first research mentor.

Beyond the academic sphere, I want to thank my friends for bringing joy and emotional support to my life. Zongshun Zhang, I cherished our chats and video-watching sessions, where we shared both happiness and challenges. Fou He, I enjoyed playing games and cooking with you. Chengxin Yu, thank you for helping me set up my home and for our adventures exploring parks and photography. Ji Li and Xin Li, thank you for exercising with me, hanging out, and sharing good food. Xiangchen Cai, I enjoyed our badminton matches and hiking trips. Yufeng

Bai and Yingxia Chen, thank you for your guidance on school applications and future plans dating back to elementary school. Dr. Jifeng Zhang, your warm support has been a pillar in my life, from helping me settle my car to assisting with my new home.

I owe a special debt of gratitude to my family for their unyielding love and support. To my parents, thank you for instilling in me the values of hard work and perseverance. Your care and concern for my happiness have been constants in my life, whether near or far. To my partner, Zitong Wang, your love and understanding have been my anchor throughout this challenging yet rewarding period. I feel incredibly fortunate to have met you and cannot imagine this journey without your presence.

To everyone who has contributed to this work, whether directly or indirectly, please accept my heartfelt thanks. This achievement is as much yours as it is mine.

Lastly, I would like to acknowledge the financial support, including grants and fellowships provided by the University of Michigan. The research in this dissertation was funded and supported by the Department of Energy, Basic Energy Science under Award number DE-SC0013562.

Table of Contents

Dedication ii

Acknowledgements iii

List of Tables x

List of Figures xi

List of Appendices xix

Abstract xx

Chapter 1 Introduction 1

1.1 Motivation and research aims 1

1.2 Colloids 2

1.2.1 Colloidal dynamics 3

1.2.2 Pair potential of colloids 4

1.2.3 Colloidal self-assembly and crystallization 5

1.2.4 DC electric field directed colloidal assembly 6

1.2.5 AC electric field directed colloidal assembly 7

1.2.6 Structural visualization and characterization 9

1.2.7 Molecular dynamic simulation of self-assembly 11

1.2.8 Mie scattering theory 11

1.3 Biomimetic structural color 12

1.3.1 Structural color mechanisms 14

1.3.2 Optical modeling and simulation for photonic crystals 15

1.4 Organization of the dissertation thesis with specific research aims 17

Chapter 2 Direct Current Electric Field Assembled Colloidal Crystals with Reconfigurable Grating Diffraction Structural Color 19

2.1 Abstract 19

2.2 Introduction 20

2.3 Methods 24

2.3.1 Preparation of Colloidal suspensions and direct current (DC) electric field self-assembly device 24

2.3.2 Optical measurement and spectroscopy 25

2.3.3 CLSM imaging and analysis 26

2.3.4 Structural color characterization 26

2.3.5 Spectral modeling from scattering theory 26

2.4 Results and Discussion 28

2.4.1 DC induced colloidal assembly and crystallization creates prismatic coloration 28

2.4.2 Effect of particle size and the polycrystalline identity on structural color properties 30

2.4.3 Effect of crystalline layer thickness on structural color properties 33

2.4.4 Mie scattering modeling of diffraction spectral response 35

2.4.5 Modeling of grating diffraction over wide range of particle sizes and layer thickness 39

2.5 Discussion 42

2.6 Conclusions 46

2.7 Supplementary Information 47

Chapter 3 Defect Structures in Colloidal Crystals and Their Effect on Grating Diffraction Structural Color 51

3.1 Abstract 51

3.2 Introduction 52

3.3 Methods 55

3.3.1 Colloidal self-assembly by DC electric fields 55
3.3.2 Optical spectroscopy of structural color 57
3.3.3 Confocal laser scanning microscopy 57
3.3.4 Molecular dynamics simulation 58
3.3.5 Hexatic Order Parameter 59
3.3.6 Crystal grain analysis 60
3.3.7 Finite difference time domain (FDTD) simulation of optical spectra 61
3.4 Results 62
3.4.1 Setup of real-time structural and optical measurement 62
3.4.2 Electrophoretic deposition kinetics at various operating conditions 62
3.4.3 Structural color and spectral during crystallization 64
3.4.4 Structural and optical reversibility 65
3.4.5 State diagram of DC electric field assembled spheres 67
3.4.6 Crystal quality and grain property characterization of structures in state diagram . 69
3.4.7 MD simulation of the self-assembly process 71
3.4.8 Trade-off between structural color intensity and uniformity at various defect abundance 74
3.5 Discussion 77
3.6 Conclusions 80
3.7 Supplementary Information 81
Chapter 4 Colloidal Crystal Grain Boundary Annealing by Rotating Electric Fields with Six-Fold Symmetry 87
4.1 Abstract 87
4.2 Introduction 88
4.3 Methods 91
4.3.1 Fabrication of coplanar microelectrode device 91

4.3.2 Preparation of the colloidal suspension 91
4.3.3 Application of the rotating electric field 92
4.3.4 Characterization of the self-assembled colloids 92
4.3.5 Calculation of field strength and driven forces 94
4.4 Results 94
4.4.1 Experimental setup with automated AC electric field 94
4.4.2 Characterization of the microstructure during annealing process 95
4.4.3 Particle traveling velocity and triangle trajectory 97
4.4.4 Structural evolution under various AC frequencies 99
4.4.5 Annealing performance vs. operating conditions 101
4.4.6 Dielectrophoretic force and active energy injection 102
4.4.7 Transition of state for a single particle 105
4.5 Discussion 107
4.6 Conclusions 110
4.7 Supplementary Information 111
Chapter 5 Conclusions 114
5.1 Summary of research 114
5.2 Outlook and future directions 116
5.2.1 Further improvement of grating diffraction efficiency 116
5.2.2 Reversibility and durability in reconfigurable electrophoretic deposition 117
5.2.3 Categorizing defects using machine learning-aided image analysis 118
5.2.4 Effect of field symmetry on the annealing of defects in spheroid colloidal crystals 118
Appendices 120
Bibliography 141

List of Tables

Table 3.1: MD Simulation parameter κ. Estimated for different salt concentrations..... 86

Table 3.2: MD simulated electric field strength and lateral attraction potential. For different current density measured in the experiment..... 86

Table 4.1: Parameters used for force calculations at different field frequencies. ReCMω was determined by *Mittal et al.* by assuming that its value is log-linear between 1 kHz to 30 kHz following the equation $\mathrm{ReCM}\omega = -0.39\log\omega + 2$..... 111

List of Figures

Figure 2.1: Angular dependent structural color of a self-assembled colloidal crystal composed of three layers of 1.0 μm PS spheres. (a) Schematic of two limiting mechanisms of structural color – transmissive grating diffraction and Bragg reflection. (b) Coloration and structural change due to self-assembly and crystallization, electric field device with particle suspension and CLSM image of the structure, image captured before and after self-assembly. Scale bar: 10 μm (for CLSM images), 5 mm (for device cell); labeled angles are as defined in the next panel. (c) Schematic of the transmission optics, showing the definition of the polar angle θ used for imaging and spectrophotometry. (d) Spectral response of the structural color at angles varying from 25° to 60°. (e) CIE 1931 chromaticity diagram showing the spectral measurements at various θ. The data for angles 48-60° involve second order diffraction; these points overlap and are shown in a different color. 28

Figure 2.2: Angular dependence of the prismatic structural color. (a) CLSM image of the polycrystalline layer at the substrate for self-assembled 1.0 μm PS colloids. Scale bar: 50 μm. (b) A zoomed-in image of the boxed area in (a) showing the underlying close-packed structure of the crystal. The red dash line indicates different grain orientations of neighboring crystallites. Scale bar: 10 μm. (c) The 2D radial distribution function (RDF) of the crystal and its corresponding FFT image. (d) Polycrystalline structure that results in a white light diffraction pattern that is radially symmetric; single crystal structure results in a white light diffraction pattern with six-fold azimuthal symmetry. (e) Polycrystalline (CLSM image) vs. single crystal (SEM image) ordering that yields the differences in the previous panel. (f) The measured scattering intensity (at peak wavelength 435 nm) for both polycrystalline and single crystal structures as a function of azimuthal angle. (g) Schematic showing the polar angle θ, and azimuthal angle ϕ of the measured diffracted light beam, with the hyperbola depicting the shape of the light emission captured on a vertical reflection screen as specified by the intersection of the screen with the emission cone. (h) Grating structural color projected onto a vertical reflection screen as per the geometry of the previous panel, showing its prismatic effect for particle diameters varying from 0.37 to 1.3 μm. Scale bar: 5 cm. (i) The peak wavelength of the spectral response at a function of scattering angle for different particle diameters. 30

Figure 2.3: Layer dependence of the prismatic structural color. (a) CLSM images show the layered structure of the self-assembled crystal for, from left to right, 1, 3, and 7 layers, as generated by self-assembly of suspensions with volume fraction of 0.32%, 1.0%, and 2.3% respectively. Images are acquired in a plane perpendicular to the bottom substrate. Scale bar: 5 μm. (b) The grating structural color projected onto a vertical reflection screen, with number of layers as in panel A. Scale bar: 5 cm. (c) The spectral response measured at θ = 25° (green: 505 nm) as number of layers is varied from 1 to 15. (d) Spectrum-converted colormap shows structural color at θ varying from 25° to 40°, respectively. (e) CIE 1931 chromaticity diagram

showing the saturation loss by increasing the layer thickness. (f) Peak spectral intensity at different layer thickness for θ varying from 25° to 40°. 33

Figure 2.4: Light scattering modeling of the angularly dependent spectral response at different self-assembled particle sizes and layer thicknesses. Surface plots of scattering intensity at various polar angles (θ = 0-180°) and wavelengths (λ = 400-900 nm), with selected particle sizes of 0.2, 0.3 and 1.0 μm, and layer numbers of 1, 3 and 7, respectively. The regions of interest identified (boxes: grating diffraction; white arrows: Bragg reflection; and green arrows: discrete peaks) are described in the text. 36

Figure 2.5: Operating ranges for grating diffraction and Bragg reflection structural color. (a) The simulated spectrum for a three-layer colloidal crystal comprised of 1.0 μm particles (solid curves) plotted with the experiment measurements (dash curves). (b) Correlation of the experimentally measured peak wavelength with dimensionless groups suggested by the diffraction grating equation, for particle size of 0.37-1.3 μm, and for first and second diffraction orders. The inset plot shows the agreement between experiment and theory for the diffraction wavelength of crystals with 1.0 μm diameter colloids. (c) Structural color modeled intensity diagram shows the effect of particle size and number of crystal layers on structural color mechanism – Bragg reflection (BR) and grating diffraction (GD). The dash lines indicate the boundary between the three regions. In Region I: Only BR color is visible; GD is shifted into the UV (non-visible). In Region II: 1st order BR is shifted into the NIR, while the 2nd order BR is in the visible range (but with weak intensity); the 1st order GD yields visible color. In Region III: 1st and 2nd order BR are shifted into the NIR and multiple higher order BR are in the visible; the multiple reflections yield diffuse (milky) color; the 1st order GD generates full prismatic color, while the 2nd order GD provides such color but with lower intensity. 39

Figure 2.6: Experimental Setup. (a) Custom designed apparatus to measure optical spectrum from a colloidal sample at different angles, schematic diagram (left) and device image (right). Scale bar: 20 cm. (b) DC self-assembly device, schematic diagram (left) and device image on sample stage after self-assembly (right). Scale bar: 5 cm. 47

Figure 2.7: Reconfigurable Structural Color Spectral Response. The grating structural color (measured at θ = 30° for colloidal crystals assembled by 1 μm particle) shows high reconfigurability by switching the voltage between 0V, 3V, and 3.5V. 47

Figure 2.8: 3D Structure of DC Electric Field Assembled Colloidal Crystal. (a) Z-stack confocal image of the colloidal crystal structure from the bottom layer (Layer 1) to the top (Layer 7) for a 7-layer colloidal crystal. Scale bar = 10 μm. The cross-sectional image shows (110) plane of the FCC crystal structure. Arrow length = 2 μm. (b) 3D view of the structure. ... 48

Figure 2.9: Raw spectra of angle dependent structural color, measured for colloidal crystals with particle size d_p of 0.37, 0.53, 0.74, 0.90, and 1.3 μm, respectively. Light incident angle θ_i is fixed for each set of measurement, while the diffraction angle θ_d varies as in the legend. These spectra are converted to diffraction efficiency for main text plots as per the Methods 49

Figure 2.10: Performance of light scattering modeling. These figures report calculations that are components of the optical spectrum calculations reported in the main text. (a) Mie scattering form factor for 1.0 μm polystyrene spheres in DMSO. (b) Structure factor for a 3-layer FCC crystal with 183 particles (1.0 μm diameter), at scattering angle $\theta = 40°$ and azimuthal angle $\phi = 0°$. The interparticle distance is 1.13 μm and the volume fraction is 0.489. (c) Calculated scattering intensity from the product of the form factor and structure factor in (a) and (b), using Equation 2.1 and 2.3 of the main text. (d) Structural color spectrum plotted as scattering intensity vs. wavelength (converted from q by its definition), for the wavelength range 400-900 nm, indicating a red color predicted at $\theta = 40°$ and $\phi = 0°$. 49

Figure 2.11: Structural color regimes for normal and oblique light incidence. In colloidal crystals, Bragg reflection (BR) and grating diffraction (GD) structural color are both angularly dependent, but with different behaviors. BR appears at specular angles, with monochromatic coloration that varies with the incident angle, while GD shifts the prismatic color band to different angles when the incident light angle is varied. 50

Figure 3.1: Crystal property characterization by spectroscopy and microscopy. (a) Schematic of the electrophoretic deposition in the DC electric field device. (b) Measurement of prismatic structural color by spectroscopy. (c) Wide field, high resolution CLSM image of the colloidal crystal acquired by image stitching. (d) Analysis of the CLSM image identifies crystal grain orientation, grain boundaries, and the local hexatic order parameter. Here, the color coding in the left panel identifies individual crystal grains. In the right panel, regions in yellow have high hexatic order parameter characteristic of high crystal ordering; other regions have low hexatic order parameter, and follow grain boundaries. Scale bar: 20 μm. 62

Figure 3.2: CLSM images display the electrophoretic deposition, self-assembly and crystallization kinetics at various experimental conditions. Images were captured at the surface of ITO electrode. (a) c = 10 mM and i = 31 $\mu A/cm^2$, (b) c = 0.1 mM and i = 31 $\mu A/cm^2$, and (c) c = 0.1 mM and i = 3.1 $\mu A/cm^2$. Scale bar: 10 μm. 63

Figure 3.3: Time evolution of grating diffraction structural color. (a) Image time-series of the evolution of structural color in the self-assembled crystals at time 0, 30, 60, and 90s; the diffraction angle of observation is 30° from the axis of transmission of the source. (b) Time-evolution of the measured optical spectrum at 0, 30, 60 and 90s from the bottom to the top. The measurement conditions are c = 0.1 mM and i = 31 $\mu A/cm^2$. 64

Figure 3.4: Tunability of the interparticle spacing and grating diffraction structural color. (a) Radial distribution functions, g(r), of colloidal crystals self-assembled at c = 0.1 mM and current density varying from i = 3.1 to 160 $\mu A/cm^2$. Data are vertically offset for clarity. Inset figure shows the measured interparticle distance, as defined by the schematic, at the different current densities. (b) Corresponding structural color spectra for the same conditions, also for conditions varying (a) from 3.1 to 160 $\mu A/cm^2$. The spectral maximum shifts from green to blue as i increases. The left and right insets are camera-captured images of structural color at the highest and lowest i, respectively. The insets figure shows how i is applied stepwise to probe each condition. 65

Figure 3.5: State diagram of DC electric field assembled colloids. (a) Electrophoretic state diagram for operating conditions varying from c = 0.01 to 10 mM and i = 1.6 to 310 μA/cm^2. Regimes labeled with blue, green, and red are dense liquid, polycrystal, and adsorbed state, respectively. (b) CLSM images of the microstructures resulting from various operating conditions. Corresponding experimental conditions are labeled in panel (a). Scale bar is 10 μm. 68

Figure 3.6: Crystal quality and grain boundary analysis of self-assembled structures. (i) c = 0.1 mM, i = 3.1 μA/cm^2, (ii) c = 0.1 mM, i = 79 μA/cm^2, (iii) c = 10 mM, i = 7.9 μA/cm^2, and (iv) c = 10 mM, i = 310 μA/cm^2. (a) Images show particle positions derived from image analysis and are color-coded by individual ψ6, j values. The globally averaged hexatic order parameter ψ6 is also shown above each image. Scale bar: 10 μm. (b) Images show crystal grains identified by image analysis; they are color-coded by their Y coordinates. The number density of crystal grains (ng) per 0.01 mm^2 is provided. Scale bar: 10 μm. (c) ψ6 and (d) ng measured at the studied operating conditions with ranges of c = 0.01 to 10 mM and i = 1.6 to 310 μA/cm^2. Plots in pannel (a)-(b) were created by Chih-Mei Young. 70

Figure 3.7: MD simulation results of the deposition and assembly process. (a) Schematic of the deposition simulation box; red labels particles that have reached the bottom substrate. (b)-(c) Snapshots of structures from MD simulations at conditions that correspond to the conditions of Figure 3.2 case (b) and (c), respectively. (d) Substrate layer of the self-assembled structures at c = 0.1 mM and various i in μA/cm^2, as simulated by MD. (e) Comparison between experiment and simulation for i = 1.6 to 310 μA/cm^2 for globally averaged hexatic order paramter, ψ6. (f) Comparison between experiment and simulation for i = 1.6 to 310 μA/cm^2 for number density of crystal grains, ng. Liquid and crystal regions are identified and labeled. Plots in pannel (a)-(d) were created by Chih-Mei Young. 72

Figure 3.8: Correlation between defect abundance and structural color properties. (a) Measured structural color spectrum for different ψ6 corresponding to different positions on the state diagram. (b) Structural color peak intensity in different electrophoretic states and ψ6 values; including experimentally measured diffraction efficiency (left-axis) and FDTD simulated far-field diffraction efficiency (right-axis). The left-hand scale corresponds to the ○, □, and △ symbols; the right-hand scale corresponds to the ◇ symbols. (c) Crystal-grain structure (substrate layer) of the MD simulated crystal. The simulated structures vary in crystal quality and cluster number; the left-hand panel reports a single grain of high crystal quality. Scale bar: 10 μm. (d) Structural color spectrum calculated by the FDTD method (for polar angle θ = 30°) for the MD simulated structures of panel (c). The inset figure in each panel shows the diffraction pattern by far-field projection calculated by FDTD, also labeled by the ψ6 values. (e) Simulated structural color spectrum by calculating the diffraction intensity at θ = 30° for different azimuthal angles for the four cases in panel (c) and (d). (f) The average structural color intensity and azimuthal uniformity as a function of the number of grains in the simulated region. Structure in panel (c) is created by Chih-Mei Young. 74

Figure 3.9: Measured deposition rate at various conditions. (a) Measured conductivity of DMSO with different added TBAC concentrations. (b) Measurement and modeling of electrophoretic deposition kinetics. (a) Characterization of the deposition velocity for different

operating conditions is made by recognizing that mass conservation requires that the slope of a plot of haKϕoϕaϕo − 1 vs. t yields uo, the colloidal deposition velocity. Here ha is the height of the first (substrate) layer, ϕa is the volume fraction of that layer at time t, ϕo is the initial particle volume fraction in solution, and the constant K = 1 − ϕo6.55 addresses the volume fraction dependent retardation due to sedimentation. (c) The measured Peclet number (log scale) at different operating conditions, as function of salt concentration and applied current density. 81

Figure 3.10: Pair potentials in MD simulation. (a) Model for MD simulation of the self-assembly. Bulk (non-surface) particles (white spheres) interact repulsively through VDL, as per the Equation 3.1 illustrated in the main text; particles at the substrate (pink spheres) interact through a Lennard Jones potential, VLJ, which models the effective lateral attraction due to electrohydrodynamic flow. (b) Sample plots of the pair potential for the two types of interactions, at c = 0.1 mM and i = 79 μA/cm^2..... 82

Figure 3.11: Properties of crystal grains. Characterized from the confocal microscopy images of the substrate layer, as captured during the electrophoretic deposition and produced by cluster analysis (cf. Methods). Top rows identify crystalline particles as per the value of ψ6, j at different deposition times t; the bottom row plots how the number of crystal grains in the image changes with time. These structural kinetics are reported for operating conditions: (a) c = 10 mM, i = 31 μA/cm^2 c = 0.1 mM, (b) i = 31 μA/cm^2, and (c) c = 0.1 mM, i = 3.1 μA/cm^2. 82

Figure 3.12: Test of reconfigurability of the self-assembled crystals. (a) Cyclically applied current to the device during 10 cycles. (b) The measured potential across the solution cell is also stable during the 10 cycles (data for 10 cycles are overlaid). (c) Confocal microscopy images of the polycrystalline structure captured at the same position after each cycle, also showing reversibility in the structural and crystal grain properties. Scale bar: 10 μm..... 82

Figure 3.13: 2D and 3D confocal images of particles deposited in the adsorbed region of the state diagrams. (a) When the electric field is on, colloidal particles deposit and form a disordered layer. (b) When the electric field is off for more than 10 min, the bottom layer that is in contact with the ITO surface remains adsorbed. Scale bar: 10 μm..... 83

Figure 3.14: Defects categorized by type. Sample image showing different types of defects found in the self-assembled crystals. Image presents only particles with ψ6, j ⩽ 0.85, which is the criterion for a defect particle used in this paper. Grain boundary particles represent >90% defects in this image..... 83

Figure 3.15: Simulated state diagram. (a) State diagram produced by molecular dynamics simulation shows the effect of salt concentration and current density on the self-assembled structure. The units of salt concentration are mM and of the current density are μA/cm^2, and the simulation parameters are given in Table S1 and S2. (b) The calculated average order parameter ψ6 and (c) crystal grain density ng identified per 0.01 mm^2 area. Plots in pannel (a) were created by Chih-Mei Young. 84

Figure 3.16 Correlation between diffraction efficiency and defect density. (a) 3D schematics of FDTD far field projection symmetry. The MD simulated structure, labeled as the dark red square, is located at the center of the hemisphere that defines the scattering geometry. Incident light was propagated along the z-axis, perpendicular to the sample plane of the red square (xy plane). The diffraction intensity in the far field is a function of the polar and azimuthal angles, θ and ϕ, respectively. (b) The experimentally measured diffraction efficiency decreases as the fraction of defective particles increases ($\psi 6, j < 0.85$). (c) Confocal microscopy images showing the spatial distribution of defect ($\psi 6, j < 0.85$) particles. The fraction of defect particles for each case is indicated at the upper right corner of the image. Scale bar: 10 μm. 85

Figure 3.17 Diffraction color properties at different grain size. Larger grain size increases the color intensity but reduces the azimuthal uniformity..... 85

Figure 4.1: Rotating electric field device setup. (a) Schematic of device with six-fold electrode symmetry for application of rotating electric fields. A preprogrammed signal controller connected to an AC power generator produces an electric field that is cyclically rotated by sequentially energizing three pairs of counter-electrodes, shown as Channel 1, 2 and 3. Confocal microscopy (CLSM) was used to visualize the microstructure of the self-assembled crystal. (b) The applied electric field was cycled clockwise with a constant period τ. (c) Stitched CLSM images of the device before and after the application of the AC electric field. The dash line box marks the region of the self-assembled crystal that was imaged at high resolution. The green and red channels image the electrodes and colloids, respectively. Scale bar: 100 μm. The signal controller shown in panel (a) was built by Syahidah Mohd Khairi..... 94

Figure 4.2: Analysis of particle positions in the colloidal crystals as a function time during self-assembly and annealing. The experiment was performed at an applied voltage, frequency, and period of $A = 5V_{rms}$, $\omega = 5$ kHz and $\tau = 15$s, respectively. CLSM images of the colloidal crystal structure are shown in panel (a). Particle locations in each frame are coded by phase angle (b) and modulus (c) of $\psi 6, j$ and Voronoi tessellation (d). Panel (e), (f), (g) show the time evolution of the number of clusters, average hexatic order parameter, and number of different Voronoi polygons, respectively. In (g), polygons were categorized by the number of sides, here reported for N = 3, 4, 5, 7, 8 and 9..... 96

Figure 4.3: Particle trajectories induced by the rotating AC electric field. (a) The average velocity of all particles in the central region of the self-assembled colloidal crystals at t = 200 min. Data are for two cycles of field rotation at the experimental conditions of $A = 5V_{rms}$, $\omega =$ 5 kHz and $\tau = 15$s. The particles are shown at their average positions; they are colored by their average velocity. Boxed area corresponds to the area in panel (b). (b) The trajectories of particles during one cycle (at t = 200 min) are plotted. (c)-(f) The displacement and velocity of representative particles are shown. (c) and (d) are for a particle close to the center and (e) and (f) are for particles far from the center. In (c) and (e), the black points show the particle centroids, and the red arrows show the magnitude and direction of the velocity at each time step ($\Delta t = 1$ s). (d) and (f) The velocity magnitudes and directions labeled with orange and purple markers, for the particle shown in (c) and (e), respectively. Dash line labels show the beginning and end of a cycle. 98

Figure 4.4: Control of driving forces and the effect on annealing performance. (a) Time evolution of colloidal crystal structure at A = $5V_{rms}$, τ = 15s, and ω between 1-10 kHz. Particle centroids are colored by the phase angle of their hexatic order parameter, $\psi 6$. (b) Magnitude of the hexatic order parameter vs time for the different AC field frequencies. (c) The average velocity of particles as a function of distance from the center of the self-assembled colloidal crystal. 100

Figure 4.5: The effect of AC electric field operating condition on annealing performance. $\psi 6$ and crystal grain number are shown as frequency, amplitude and cycle time are varied. (a)-(b) A = 5 V_{rms}, ω = 1-10 kHz, and τ = 15s. (c)-(d) A = 3-7 V_{rms}, ω = 5 kHz, and τ = 15s. (e)-(f) A = 5 V_{rms}, ω = 5 kHz, and τ = 3-60s. 102

Figure 4.6: Annealing as an activated process. (a) computed electric field magnitude (color) and direction (white arrow) when the top-bottom electrodes were offset by 5V. (b) Calculated DEP force for the central region device, denoted by the box in (a). Vectors represent both direction and scaled magnitude of the force. (c) Active energy generated by the DEP work (c.f. text) of each particle when the electric field is applied for (i) 1s, (ii) 5s, and (iii) 15s, at ω = 5 kHz and A = 5V. (d) The correlation between active energy and number of crystalline grains after 3h of annealing experiment, for different cycling period (circle), amplitude (squares) and frequency (triangles). (e) The overall quality of the crystal, characterized by $\psi 6$ after 3h of operation, correlated with the average active energy input by the field conditions of varying period, amplitude, and frequency of the AC field cycle. The curve plotted is to guide the eye. 103

Figure 4.7: Transition state of a local particle. (a) Active energy landscape for one cycle of operation, calculated under conditions of A = $5V_{rms}$, ω = 5 kHz and τ = 15s. The points label the location of the particles at 50 min after the cyclic field was initiated. Defect particles in the grain boundary are identified (with the condition $\psi 6, j < 0.9$) and indicated in the image with a white border. (b) Track of a single particle (marked by red circle) before, during, and after it moved from one crystal grain to the neighboring grain, at a time of 25 min, 70 min and 110 min, respectively. (c) The $\psi 6, j$ of the tracked particle in panel (b) changes over time. The orange shaded area indicates the time in defect state (as per the condition $\psi 6, j < 0.9$). The inset of the figure labels the location of the tracked particle over the entire assembly and annealing process. (d) The probability distribution of the time needed for a defect state ($\psi 6, j < 0.9$) to transition from one crystal grain to the other, here plotted for three different cycle times/active energies. 106

Figure 4.8: Reaction coordinates of self-assembly and annealing process. This diagram illustrates the hypothesized annealing mechanism by activated process. 112

Figure 4.9: Characterization of time of a single particle in defect state. (a) Defects in colloidal crystals at the condition of A = $5V_{rms}$, ω = 5 kHz and τ = 15s, at 50 min after the field was turned on. Particles are colored based on the local $\psi 6$ values to identify the grain boundary. (b)-(c) Additional example particles located at the grain boundary as shown in panel (a). The local $\psi 6$ for two particles is plotted as a function of time. Shaded areas correspond to the time needed for the particle to traverse the defect state (Δtd). The inset figure plots the location of the particle through the entire process. 112

Figure 4.10: Defect structures at conditions of various active energy input. (a)-(b) At these low active energy levels, defects are primarily present as unresolved grain boundaries. (c)-(d) At these high active energy levels, defects are primarily observed as transient dislocations. Defect particles colored as per their non-crystalline $\psi 6, j$. 113

List of Appendices

Appendix A: Computer Code 120

A.1 Scattering modeling algorithm 120

A.1.1 Mie scattering algorithm (MATLAB) 120

A.1.2 Calculation of structure factor of crystal lattice using Euler's method (MATLAB) 125

A.1.3 Calculation of structure factor of amorphous structure (MATLAB) 125

A.1.4 Build FCC crystal lattice with cylinder shape (MATLAB) 126

A.1.5 Calculation of form factor and scattering intensity (MATLAB) 127

A.2 Confocal image analysis 128

A.2.1 Particle tracking by Trackpy (Python 3) 128

A.2.2 Crystal grain analysis (Python 3) 129

A.2.3 Radial distribution function using particle centroids csv file (Python 3) 131

A.2.4 $\boldsymbol{\psi 6}$ and Voronoi analysis (Python 3) 132

A.2.5 Particle trajectory and average velocity (Python 3) 135

A.2.6 Calculation of DEP force and active energy (MATLAB) 137

A.3 Optical spectrum from FDTD far field calculation 137

A.3.1 Calculation of farfield intensity profile using MD simulated structure (Lumerical Scripting Language) 137

A.3.2 Model structural color spectrum using farfield results (MATLAB) 138

Appendix B: Definitions and Units of Symbols 139

Abstract

Self-assembly is an effective method for fabricating ordered microstructures with diverse functional properties, such as colloidal crystals. However, practical self-assembly techniques often incorporate defects into the structures produced that can compromise the functional performance. In this dissertation, we investigated defect structures created by the electric-field-induced self-assembly of colloidal spheres and the impact of these defects on the optical properties of the colloidal crystals produced. We characterized and modeled the microstructure and defects of colloidal crystals as well as their structural color properties. Additionally, we explored annealing strategies to reduce defects and enhance crystal quality.

Our first study explores the mechanism of coloration in colloidal crystals. Differing from the more widely investigated structural color, colloids with ~1 μm in size show prismatic coloration under conditions of off-axis transmission. We self-assemble colloidal polystyrene spheres arrays in a dispersed phase by application of direct current electric fields. The measured spectral peak wavelength agrees with the diffraction equation, with a diffraction efficiency is about 2.5-4%. In addition, we find less crystal layer thickness improves the color saturation. For 1 μm sized particle, the optimized color intensity is found at number of layer equal to five. In addition, we constructed a scattering model using Mie theory. This modeling specifies the building block size and layer number effects and allows full prediction of coloration spectrum with expanded design space.

We next engineer the level of defects incorporated into the self-assembled colloidal crystals and explore the effect of their abundance on the grating diffraction response. We report that the state behavior, grain morphology, and hexatic ordering are well controlled by the applied current density and salt concentration of the solution. Moreover, we find that the structural color intensity decreases defect abundance following two regimes. Compared to the defect concentrated regime, the color intensity increases about ten times

faster than in the defect dilute regime, with turning point of the hexatic order parameter at ~0.87. Moreover, we demonstrate the structures simulated by molecular dynamics are consistent. The optical simulation reveals a unique trade-off between structural color intensity and the azimuthal uniformity.

In the following chapter, we look for effective ways to anneal defects in colloidal crystals. We design and fabricate a coplanar six-fold microelectrode device and operate it with a cyclically rotating electric field to dynamically resolve defects in a colloidal crystal. For various conditions, we characterize the evolution of the microstructure by the hexatic order parameter, number of grains, and Voronoi diagram. We report that the optimal condition is at AC field of $5V_{RMS}$, 5kHz and a cycling period of 15s, which removes >99% of defects and yields a hexatic order parameter of >0.98. Furthermore, we hypothesize and test a potential mechanism for the annealing. That is, the injected energy due to the AC field activates the defect rearrangement that progressively generates global annealing. This approach generates a master curve that collapses the annealing performance as a function of field amplitude, frequency, and cycle time. An active energy of ~65 k_BT per particle yielded successful annealing with the highest crystal quality.

Chapter 1 Introduction

1.1 Motivation and research aims

Natural organisms create intricate and adaptable microstructures that enable diverse macroscopic functions. One example is the coloration that results from periodic microarrays in organs and tissues. Inspired by these natural designs, both scientific and engineering methodologies have sought to replicate these functional properties in synthetic materials. However, the performance of human-made materials often falls short, as achieving high-quality fabrication remains challenging. For example, micro-scaled assembly of these structures can yield defects that degrade functional properties. The gap between the quality of natural made biomaterials and human-made biomimetic materials requires deeper investigation into the relationship between engineered microstructure and its functional performance.

This dissertation presents a study of fundamental optical mechanisms of structural color in self-assembled colloidal crystals, the effect of defects on this structural color performance, and the development and testing of strategies to anneal defects in colloids. The interdisciplinary nature of this research combines principles from colloidal science, self-assembly, fluid mechanics, optics, and image analysis. The study addresses three key research aims:

1. What is the mechanism and properties of structural color in self-assemblies of colloidal microparticles, and can we predict the color spectral response of a such microstructures?
2. Can we control the self-assembly behavior and defect structure of self-assembled colloidal crystals by apply external fields? How do defects incorporated through these operations affect optical properties?

3. How and why do orientation-dependence of external fields promote accelerated annealing of defect structures present in self-assembled colloidal crystals, on both local and global scales?

In this introductory chapter, we describe fundamental concepts related to colloids, self-assembly, and structural color in separate sections. We further address the research aims of this work and conclude with a description of the organization of the dissertation chapters.

1.2 Colloids

The term colloidal refers to a state of matter in which particles are dispersed in a medium. This definition of colloids has been generalized to include a broad range of materials consisting of particles in a size range typically between 10^{-8} to 10^{-6} meter[1,2]. Colloids are classified depending on the state (solid, liquid, or gas) of the dispersed phase and the dispersion medium. They are important to a variety of industries. For example, paints are liquid sols with solid pigment particles dispersed in a solvent. In food science, liquid droplets are stably suspended in aqueous solution to form a colloidal emulsion[3]. Whipped cream is an example of a colloidal foam, where tiny air bubbles of colloidal size are trapped in a liquid medium. In addition, colloidal gels are widely used as products in personal care, cosmetics and pharmaceuticals[4] because of their unique rheological properties[5,6]. Finally, colloidal crystals exhibit distinct optical phenomena that can be used for materials like photonic pigments[7].Colloidal science and engineering are important fields whose goals include the design of novel materials with targeted functional properties. To address the research aims, this part of the introduction focuses on the self-assembly and crystallization of colloidal microspheres, with an in-depth discussion of colloidal interactions, dynamics, field induced assembly, and its interaction with light. Here we define colloidal microspheres as particles with size ranging between 0.1 and 5 μm.

1.2.1 Colloidal dynamics

Free colloidal particles suspended in liquid undergo Brownian motion. Brownian motion is the random fluctuation of a particle's position in the medium due to the thermal energy k_BT of that medium. Here k_B is the Boltzmann constant, and T is the temperature. In dilute solution, the movement of colloidal particles is described as a random walk due the balance of thermal motion and viscous drag of the fluid. The mean square displacement, $\langle \Delta r^2(\Delta t) \rangle$ is a measure of the time-dependence of the position of a particle relative to a reference position[5]. The 2-dimensional Brownian motion for a passive colloid is $\langle \Delta r^2(\Delta t) \rangle = 4D\Delta t$, where D is the Brownian diffusivity, and Δt is the lag time. The Brownian diffusivity of a free, spherical particle at low Reynolds number is given by the Stokes-Einstein equation[5],

$$D = \frac{k_B T}{6\pi\eta a} \tag{1.1}$$

where η is the viscosity of the medium, and a is the radius of colloidal sphere. Tools such as dynamic light scattering[8], or microscopic particle tracking[9] are commonly used to measure the particle diffusivity.

The motion of a particle is sometimes driven by external forces. In this case, the terminal velocity u is determined by balancing the external force F_{ext} and the drag force due to the friction between particle and fluid, F_d, where $F_d = 6\pi\eta a u$ for the case of a spherical particle at low Reynolds number. For example, consider the effect of gravity under these conditions. The sedimentation velocity of a free particle due to gravity is equal to $F_{eff}/6\pi\eta a$. The effective force due to gravity is determined by the relative density of particle ρ_p and medium ρ_m, which is $\frac{4}{3}\pi a^3(\rho_p - \rho_m)$ for dilute spheres[10,11]. This implies that colloidal particles with larger size and density mismatch have a greater sedimentation velocity. Similar balances can describe the

convective motion of colloidal particles under other kinds of fields, including electric and magnetic fields.

1.2.2 Pair potential of colloids

For a concentrated system, the potential interactions between particles become important; they may have a large effect on the structural properties. Differing from molecules and atoms, a macroscopic interaction between colloidal particles is the summed effect of all molecules in the body. For example, the net interaction energy is proportional to the size of the particles, and the energy and force decay much more slowly with the absolute separation distance, but much faster compared to the size. In this part of the introduction, we discuss the pair potential from common interparticle interactions including the van der Waal forces and electrostatic forces.

The pair potential due to the Van der Waals force between spherical particles can, for small separations, be expressed as, $W_{VDW} = -\frac{A_H a}{12\pi D}$, where A_H is the Hamaker constant, including the contribution from Keesom, Debye, and dispersion (London) forces, and D is the interparticle separation[5,12]. This potential model is used in molecular dynamic simulations reported in this work.

Synthetic colloids are usually charged. Electrostatic forces are repulsive due to the electrical double layer formed at the surface of colloidal particles in fluid. The electrical double layer consists of a layer of adsorbed ions and a layer composed of ions attracted to the surface charge due to Coulomb force. From a free energy perspective, this attraction is balanced by the entropic penalty of concentrating ions close to the colloidal surface. Specifically, the characteristic thickness of the electrical double layer is called the Debye screening length κ^{-1}. Debye-Hückel theory indicates that κ^{-1} is strongly correlated with the ion concentration in electrolyte. For a monovalent 1:1 electrolyte, it can be expressed as following[13],

$$\kappa^{-1} = \sqrt{\frac{\varepsilon_m k_B T}{2e^2 n^0}} \quad 1.2$$

where ε_m is the dielectric constant of the fluid, e is the electron charge, and c is the mean concentration of charge of the ion. The surface potential of each particle as function of separation distance x is $\psi(x) \approx \psi_s e^{-\kappa x}$. The calculation of electrostatic potential for small interparticle separation D is accomplished by means of the Derjaguin approximation[12], which is $W_e = 2\pi a \varepsilon_m \psi_s^2 \exp(-D/\kappa^{-1})$.

One commonly used method to model for the net pair potential of colloid is by Derjaguin-Landau-Verwey-Overbeck (DLVO) theory. This theory adds the van der Waals and electrostatic term, $W_{DLVO} = W_{VDW} + W_e$ to model the colloidal pair potential. The forces for particles separated by a distance r can then be determined from these pair potentials,

$$\boldsymbol{F} = -\frac{dW}{d\boldsymbol{r}} \quad 1.3$$

Other forces in colloidal systems, which we do not directly focus on in this thesis, include depletion forces, hydrogen bindings and hydrophobic interactions[5].

1.2.3 Colloidal self-assembly and crystallization

The phase diagram of colloidal hard spheres may be determined by computer simulation or by experiment[14,15]. Driven by the system free energy, which includes potential energy and entropic contributions, a phase transition from fluid to crystalline structure happens when the particle volume fraction reaches about 0.49. Compared with random close packing, which has a maximum packing density of 0.64, crystalline packings give a larger free volume, corresponding to large maximum packing density. Hard spheres are preferably packing into face-centered cubic

(FCC) structure or hexagonal close-packed (HCP) structure; the FCC close packed particle volume fraction to 0.74[5].

Self-assembly describes a spontaneous transition from a disordered system to organized structure. A colloidal crystal can be obtained by self-assembly. The natural self-assembly of colloids, although spontaneous, is a slow process. However, accelerating the self-assembly is possible by external stimuli, such as applied fields. Examples include evaporative deposition, [16,17], electric fields[18–20], magnetic fields[21–23], gravitational fields[24], and optical fields[25,26]. Applied fields induce a driving force that can both concentrate colloids and produce phase transitions. For example, acoustic waves produce energy which assembles colloidal particles into 2D arrays at water-air interface[27]. Magnetic fields can manipulate the dipole of superparamagnetic colloids and produce structures such as elongated clusters[22]. Comparing with other approaches, self-assembly by electric fields is controllable, reconfigurable, and easily implemented for common dielectric colloids. The work reported in this thesis includes the use of two type of electric fields—direct current (DC) electric fields and alternating current (AC) electric fields.

1.2.4 DC electric field directed colloidal assembly

DC electric fields represent the one directional flow of electric charge, which can be created by a voltage offset across a conducting capacitor. Particles with charged surfaces migrate and deposit onto a liquid-electrode interface under a DC electric field. This process is called electrophoretic deposition (EPD)[28–31]. DC electric fields induce an electroosmosis flow which can concentrate colloidal particles to a volume fraction sufficiently high to for crystallization[32]. A stable crystalline structure is therefore self-assembled through the balance of the EPD force and osmotic pressure.

Physically, the induced dc field magnitude E is determined by the applied current density i following the equation, $E = i/\sigma_m$, where σ_m is the ion conductivity of the solution[19,32]. When the field is applied, colloidal particles displace at a terminal velocity u, which depends on the field strength E and zeta potential ζ, following the formula: $u = \frac{\varepsilon_m \zeta E}{\eta}$, valid in the Smoluchowski limit[19]. This DPE velocity can be calculated experimentally by microscopic image analysis[32,33]. In DC electric field assembly system, particles dynamics include both EPD motion and Brownian motion. The relative magnitude of convection due to EPD and diffusive transport from Brownian dynamics is defined by the Péclet number, which is scaled by the particle radius as,

$$Pe = \frac{2au}{D_o} \tag{1.4}$$

where D_o is the free Brownian diffusivity. A Peclet number of 0.1 - 1 is needed for phase transition from dilute to crystalline of colloidal spheres[19].

Another driving force for nucleation and crystallization at the electrode surface is the effect of electroosmosis flow at the substrate boundary. This flow is parallel to the electrode; it induces a lateral attraction which brings deposited particles into crystalline clusters[30]. This lateral attraction is relevant to the crystallization kinetics in a EPD process.

1.2.5 AC electric field directed colloidal assembly

Differing from DC electric fields, the strength of an AC electric field varies in a regular pattern, with a periodic maximum amplitude A and frequency of f. For colloids in a high frequency AC field (f > 1kHz), charges on the surface of a dielectric sphere and in the Debye layer will be shifted, causing polarization and a temporary dipole moment. In this work, the self-

assembly by AC electric fields is driven by two major factors: field-induced dipole-dipole interactions and the dielectrophoretic (DEP) force.

The induced dipole of a single particle is aligned with the field direction. Dipolar interactions between two such polarized particles are attractive. Particles can assemble into "chains" (1D crystal) initially and form 2D crystals due to dipolar interactions between chains if the concentration is high enough[34]. AC induced a temporary delay in materials dielectric constant, which is called dielectric relaxation. The polarization and dielectric relaxations depend on the frequency of the applied AC field, which is captured by the real-part of the Clausius-Mossotti (CM) factor expressed as following[34,35],

$$\mathrm{Re}|\mathrm{K}(\omega)| = \frac{\varepsilon_p - \varepsilon_m}{\varepsilon_p + 2\varepsilon_m} + \frac{3\left(\varepsilon_m\sigma_p - \varepsilon_p\sigma_m\right)}{\tau_{MW}\left(\sigma_p + 2\sigma_m\right)^2(1 + \omega^2\tau_{MW}^2)} \qquad 1.5$$

where ε_p and ε_m are the permittivity of particle and solution, respectively, σ_p and σ_m are the conductivity of particle and solution, respectively, ω is the angular frequency of polarization, and τ_{MW} is the Maxwell-Wagner charge relaxation time. τ_{MW} is defined as $\frac{\varepsilon_p+2\varepsilon_m}{\sigma_p+2\sigma_m}$. The upper and lower bound of $\mathrm{Re}|\mathrm{K}(\omega)|$ is determined by the material properties of particle and medium. In the polystyrene/water system, the range of τ_{MW} is between -0.5 and 1.0. A comprehensive model for the dipolar interaction of a particle is[35],

$$\boldsymbol{F}_{dip} = \frac{3}{4}\pi a^2\varepsilon_{\mathrm{m}}\left(\frac{2a}{r}\right)^4(\mathrm{Re}|\mathrm{K}(\omega)|)^2 \cdot |\boldsymbol{E}|^2\left[(3\cos^2\theta - 1)\hat{r} + (\sin 2\theta)\hat{\theta}\right] \qquad 1.6$$

where $\boldsymbol{E}$ is local voltage of AC, θ is the polar angle relative to the field direction. The functional form shows that the dipole force decays quickly (as r^{-4}) and is maximized when align with the field (θ = 0 or π).

The DEP force can also induce particle motion. Dielectrophoretic force acting on a particle is due to interfacial polarization between the particle and the medium in a non-uniform electric field[36]. Under conditions of a spatially varying electric field, a particle flow occurs with a direction of $-\boldsymbol{\nabla E}$. The expression for the DEP force under such a non-uniform AC field is[34],

$$\boldsymbol{F}_{DEP} = 2\pi a^3 \varepsilon_{\mathrm{m}} \mathrm{Re}|\mathrm{CM}(\omega)| \cdot \boldsymbol{\nabla}|\boldsymbol{E}|^2 \qquad 1.7$$

DEP forces can be used to regulate, transport, and separate different types of particles in fields such as medical diagnostics and cell therapeutics. For example, cells with various sizes and properties can be separated using microelectrodes built into a microfluidic device which control the direction and magnitude of DEP forces[37]. Equation 1.7 also specifies the active force injected into a self-assembled material due to DEP.

1.2.6 Structural visualization and characterization

The microstructures of self-assembled colloid can be visualized and analyzed by application of confocal laser scanning microscopy (CLSM). Particle identification and tracking algorithms can identify the centroid of each sphere in space and time so structural and dynamic behavior may be characterized. Common approaches to analysis in colloidal science research include measuring the radial distribution function g(r), order parameters ψ_6, and the structure factor $S(\boldsymbol{q})$.

The g(r) describes how particle number density varies as a function of distance r from a reference particle. It is proportional to the probability of finding a particle within a distance r to $r + dr$. The g(r) can be used to identify the phases of a colloidal self-assembly, including whether it is disordered, glassy, liquid crystalline, crystalline or a gel. The largest peak for a compact structure defines the nearest neighbor contact. A shaper peak also indicates a higher ordered crystalline packing. The Fourier transform of the second-order RDF is called the

structure factor. For a system consisting of spherically symmetric particles, the static structure factor is defined as[38,39],

$$S(\boldsymbol{q}) = \frac{1}{N}\sum_{j=1}^{N}\sum_{k=1}^{N} e^{-i\boldsymbol{q}\cdot(\boldsymbol{R}_j-\boldsymbol{R}_k)} \quad 1.8$$

Where N is the number of particles and $\boldsymbol{R}$ is the positional vector of particle, here indexed by subscripts *j* and *k*. The relationship between $S(q)$ and g(r) is $S(\boldsymbol{q}) = 1 + \rho \int e^{-i\boldsymbol{q}\cdot\boldsymbol{r}} g(r) d\boldsymbol{r}$, where $\rho = N/V$ is the average number density of particles and $\boldsymbol{r} = \boldsymbol{R}_j - \boldsymbol{R}_k$[40]. Experimentally, $S(\boldsymbol{q})$ can be determined by a measurement such as light scattering[41]. For example, small-angle light scattering of a crystalline colloidal suspension will generate a six-fold diffraction pattern. The sharpness of the diffraction peak is an important criterion in identifying the overall quality of a colloidal crystal[42,43]. The structure factor can also be calculated from a real space image if the particle centroidal locations have been identified. From the scattering perspective, $S(\boldsymbol{q})$ describes the correction to the ensemble average intensity due to the relative configurations of the scattering objects in the system.

An alternative way to quantify the degree of crystalline order in a system is by computing order parameters. For a 3D colloidal crystal with FCC or HCP structure or a hexagonally packed 2D colloidal crystal, its orientational order in a plane may be determined by the local director field of a particle at R_j, which has an angle θ_{jk} relative to particle at R_k. This hexatic orientational order is calculated by the following equation[44,45],

$$\Psi_{6,j} = \frac{1}{N_j}\sum_{k=1}^{N_j} e^{i6\theta_{jk}} \quad 1.9$$

where N_j is the number of neighbors around particle j. $\Psi_{6,\mathrm{j}}$ is a complex number. The magnitude of $\Psi_{6,\mathrm{j}}$ is hexatic order parameter $\psi_{6,j}$, which represents the local crystalline order of the particle

j based on its neighbor locations, with a value between 0 (disordered) and 1 (perfectly ordered). For a structure with multiple particles, the average hexatic order parameter is the average of individual $\psi_{6,j}$ in the system. Moreover, the orientation of the local order is represented by the phase angle calculated by $\delta_{6,j} = \arctan\left(\frac{\mathrm{Re}(\Psi_{6,\mathrm{j}})}{\mathrm{Im}(\Psi_{6,\mathrm{j}})}\right)$, which has a range from $-\pi$ to π, and is defined relative to a reference angle specified for the system. $\psi_{6,j}$ and $\delta_{6,j}$ are important parameters that characterize both local and global crystal properties. They can also be used as input to other characterization methods, such as cluster analysis[46,47].

1.2.7 Molecular dynamic simulation of self-assembly

The dynamics and self-assembly of colloids can be efficiently predicted by computational simulation; the method we use in this study is molecular dynamics (MD) simulation in the colloids are modeled as particles that interact through forces in equilibrium at a fixed temperature. For a fixed time period, the forces and potential energy of particles in the system that drives the dynamics are calculated. MD simulation has been widely used in areas including protein structural engineering[48], nano/colloidal science[49–51], and drug discovery[52]. In this work, MD simulation is specifically used to model the field induced assembly, crystallization, and assembled structures. The simulation is conducted using open-source engine called HOOMD-blue[53].

1.2.8 Mie scattering theory

The interaction between spherical particles and light with different refractive indexes is well studied. Light scattering theory represent solutions of Maxwell's equations under particular conditions of particle size and refractive index. Mie scattering is a special case of the light scattering from a single, homogeneous object with a size comparable to the light wavelength and

described by a (potentially complex) refractive index[54]. Colors are produced during such single particle scattering because the scattered field in the visible spectrum is wavelength dependent for such particles. Researchers have observed different scattering colors from dilute suspension of polystyrene colloids of variable sizes[55]. The measured backscattering cross-section, which is related to reflectivity, is well-modeled with Mie scattering theory. The Mie form factor $F(\boldsymbol{q})$ represents the intensity distribution for scattering from a single particle. It can be computed by the following equation for a unpolarized light[54],

$$F(\boldsymbol{q}) = \frac{I_s}{I_o} = \frac{1}{k^2 r^2}\left[\frac{1}{2}(\boldsymbol{S}_1\boldsymbol{S}_1^* + \boldsymbol{S}_2\boldsymbol{S}_2^*)\right] \quad 1.10$$

In this equation, the form factor is the intensity ratio of scattered light I_o and incident light I_s. It is a function of q, the scattering vector, equal to $\frac{4\pi}{\lambda}\sin\left(\frac{\theta_s}{2}\right)$, where λ is the wavelength of light in solvent medium, and θ_s is the angle of scattering. k is the norm of wave vector, which is equal to $\frac{2\pi}{\lambda}$. S are the elements of the electric field amplitude scattering matrix, as computed using Mie algorithm (code written by Prof. Mike Solomon for class CHE 696, 2003). The Mie algorithm determines the components of the scattering matrix S with the inputs of the particle size a, wavelength of light λ, the ratio of particle/medium refractive index n_p/n_m, and the scattering angle θ_s.

1.3 Biomimetic structural color

Color is the visual perception of light that has interacted with color receptor cells in the human eye. The range of electromagnetic wavelength that can be perceived by humans ranges from about 380 nm to 750 nm, called the visible spectrum[56]. Colors can be generally produced in several ways. One is through additive mixing of different wavelengths of Red-Green-Blue (RGB) light[57]; this is the way color is displayed in televisions and computers. Light emitted from

objects is commonly produced by the other method, called subtractive coloring[58]. For example, pigments and dyes can absorb certain wavelengths of light because of their chemical composition[59]. Light that is not absorbed can pass through the object and be detected by the human eye. The wavelength dependence of the absorption determines the subtractive color. Color can also be generated due to electronic relaxations from a high energy to a lower energy state, yielding fluorescence and phosphorescence[60,61]. Finally, and differing from the coloration methods mentioned above, a material with a microstructure that causes interference of light as it is transmitted, can also produce coloration. This interference mechanism is equivalent to light scattering and can be modelled by the theory of light scattering. This physical coloration mechanism is called structural color[62–64]. Compared to chemical coloration mechanism, such as from materials containing pigment or dyes, structural color materials are more sustainable and can persist for long time without suffer degradation of coloration due to effects such as UV-induced degradation[18,65]. Structural color also exhibits unique properties including tunability[18,65], high saturation[66], and angular dependence[17,31].

Structural colors are commonly found in natural objects and organisms. A well-known instance is the brilliant and iridescent blue color of *morpho* butterfly wings. A microscope reveals the highly ordered microstructure in single scale of the *morpho* wing[67]. The ridges were packed into gratings, with each ridge containing multiple layers of lamella[63,68]. The overall blue coloration was generated from light interference by the multilayered microstructure resulting in selectively reflected blue light. This coloration mechanism originates from Bragg's reflection [7,63]. However, the brilliance of butterfly wings is also caused by another mechanism. A recent study found that the grating pattern of ridges can also produce prismatic color because of the effect of diffraction grating[62,63]. These two mechanisms have different spectral properties and are

widely used in artificial structural color materials research and fabrication. The subject of this dissertation will engage both of these mechanisms for structural color.

1.3.1 Structural color mechanisms

Reflective structural color due to Bragg reflection is abundant in nature, including natural opals[64], the exoskeleton of insects[69], and the feather of peacocks[70]. Some structural colors are reconfigurable via manipulation of the microstructure that generates the interference, such as in cephalopods[71] and chameleons[72,73]. These organisms can change their skin color to adapt to different environments. For multilayered structures, Bragg theory allows one to predict the wavelength of light reflected form a multilayer structure as the following[16,18],

$$m\lambda_p = 2d\sqrt{n_{eff}^2 - \sin^2\theta} \tag{1.11}$$

where m is the order of diffraction (m = 1, 1st order, m = 2, 2nd order…), λ_p is the reflected spectral peak wavelength, d is the interlayer distance, n_{eff} is the effective refractive index, and θ is the light incident angle relative to the normal of layer plane. For a binary, multilayered material with alternating refractive index, n_{eff} is determined by the relation $n_{eff}^2 = \Phi_1 n_1^2 + \Phi_2 n_2^2$, where Φ_1 and Φ_2 are the volume fraction of the two components, and n_1 and n_2 are refractive index of these materials, respectively. Bragg's reflection occurs when the wavelength of light is comparable to the periodicity of a multilayer stacking. The reflection is in phase with the incident light in specular angle θ relative to the stacking plane. Bragg reflection structural colors yield high reflectivity and color saturation, with broad applications such as automotive coatings[74], anticounterfeiting codes[75], and photonic pigments[23], etc.

An alternative way to produce color is through the mechanism of grating diffraction[7,76,77]. In a spectrophotometer, optical gratings consist of periodic microarrays in 2D structure that

diffract light[78]. The angle and wavelength of diffracted light depend on the angle of incidence and the grating periodicity. A diffraction grating can split an incident beam of white light into prismatic colors propagated to off-axis angles. This type of structural coloration is less recognized and even believed to exist in nature until the late 20th century[79]. This diffraction grating effect is less common in nature because it requires very ordered and long-range structure. which are apparently hard to achieve in natural due to irregularity of shape of these creatures[77]. However, there natural examples do exist. For example, shrimp *Azygocypridina lowry*[77], peacock spiders *Maratus*[80], and bacterial colonies[81] show grating diffraction structural color. These 2D periodic grating structures create structural colors following the diffraction equation[7,82],

$$m\lambda_p = d(\sin\theta_i + \sin\theta_d) \qquad 1.12$$

where d is the grating periodicity in 1D, θ_i and θ_d are, respectively, the incident light angle and diffracted light angle relative to the plane normal. Based on this equation, for light at fixed incidence, prismatic color at different wavelengths appears at a range of offset angles. Comparing and contrasting with the Bragg's reflection mechanism: both mechanisms give angular dependent color, with wavelength dependent on either the multilayer or grating periodicity. However, in Bragg's reflection where a specific monochromatic light is specularly reflected, grating diffraction structural colors are usually multichromatic and rainbow-like.

Structural color can also be produced through other mechanisms such as coherent scattering and thin-film interference[7]. In addition, a thin film of material such as a soap bubble[83], oil slick, and some the wings of beetles reflects prismatic color[62]. This dissertation thesis focuses on grating diffraction and Bragg's reflection in self-assembled colloidal crystals.

1.3.2 Optical modeling and simulation for photonic crystals

If colloids are packed into a crystalline structure with a periodic refractive index, they can induce constructive and destructive interference. This type of material is sometimes called a photonic crystal[82,84]. Visible structural color in Bragg's reflection or grating diffraction described in the prior section can be produced from these crystals. The research conducted in this dissertation thesis involves the fabrication of 3D photonic crystals with 2D periodicity using micron sized colloidal spheres as the building block. Experimentally, the optical characterization can be completed through spectrophotometry in modes that include total reflection, transmission, and diffraction. From a theoretical point of view, Mie scattering theory can model this spectral response[55,85]. For a dense particle structure, such as crystalline and glassy colloidal phases, the normalized scatter light intensity is the net effect of Mie scattering and static structure factor[85],

$$I_s = NF(\boldsymbol{q})S(\boldsymbol{q}) \tag{1.13}$$

Where N is the total number of scatters. The optical spectrum of a photonic crystal is thus generated by computing $I_s(\lambda)$.

However, to include additional effects such as multiple scattering and reflection or scattering at phase interface, a more comprehensive way to solve the Maxwell's equation is use the Finite-Difference Time-Domain (FDTD) method[86]. In this method, a time dependent electromagnetic wave is discretized by central-difference approximations to space-time partial derivatives. The Maxwell equation is solved in each mesh cell over time and complex geometries. A structure of the colloidal crystals, its material properties, and a specified light input are needed for the FDTD calculation. A far-field projection calculation simulates the spectral response of structural color as would be measured in experiment.

1.4 Organization of the dissertation thesis with specific research aims

The research objective of this dissertation thesis is to investigate the control of defects in electric field assembled colloidal crystals and its effect on grating diffraction structural color properties. The main results of the thesis are presented in three chapters.

In Chapter 2, we demonstrate a way to produce reconfigurable grating diffraction structural color using large, microparticle colloids. We observed an angular dependent prismatic structural color that appeared at an off-axis angle after electric-field induced self-assembly was conducted. We measured and explained the relationship between microstructural properties, such as the size of particle and layer of deposited crystalline layer, and the structural color properties, including the angular dependency, intensity, and saturation. In addition, we understood the experimentally found trends by modeling with Mie scattering theory.

In Chapter 3, we report the discovery of an approach to control the crystal quality of a colloidal polycrystal assembly by means of a direct current electric field. We build a phase diagram that shows how the applied current density and solution salt concentration affect the self-assembly dynamics and final structure. We perform image analysis on the defect structures and correlate their abundance to the grating diffraction structural color performance, focusing on the intensity and azimuthal uniformity of the response. We implemented simulation tools including MD simulation and FDTD to further reveal features of the relationship between defects and the structural color response.

In Chapter 4, we designed a multi-electrode device and operated it with AC electric field to anneal defects in colloidal crystals. We optimize the annealing performance by varying the operating conditions, including the AC frequency, amplitude and cycling period. We provide a set of conditions for operation that can successfully convert a colloidal polycrystal into a defect-

free single crystal. Analysis of the particle dynamics allow us to describe the defect migration mechanisms as an activated process.

Finally, this dissertation concludes with a summary of the major findings and the future directions in the field suggested by the results presented here.

Chapter 2 Direct Current Electric Field Assembled Colloidal Crystals with Reconfigurable Grating Diffraction Structural Color

2.1 Abstract

Self-assembled colloidal crystals display structural colors due to light diffracted from their microscale, ordered structure. This color arises due to Bragg reflection or grating diffraction; the latter mechanism is much less explored than the former. Here we identify the design space for generating grating diffraction structural color and demonstrate its relative advantages. We use electrophoretic deposition to self-assemble crystals with fine crystal grains from colloids of diameter 1.0 mm. The structural color in transmission is tunable across the full visible spectrum. The optimum optical response – represented by both color intensity and saturation – is observed at low layer number (≤ 5 layers). The spectral response is well predicted by Mie scattering of the crystals. Taken together, the experimental and theoretical results demonstrate that vivid grating colors with high color saturation can be produced from thin layers of micron-sized colloids. These colloidal crystals extend the potential of artificial structural color materials.

This chapter was adapted from the publication[31]: T. Liu, M. J. Solomon, Reconfigurable Grating Diffraction Structural Color in Self-Assembled Colloidal Crystals. *Small* 2023, 19, 2301871. DOI: https://doi.org/10.1002/smll.202301871. Tianyu Liu and Michael J. Solomon conceived this research. Tianyu Liu designed the experiment, built the optical setup and conducted the measurements. Tianyu Liu constructed the scattering modeling based on Professor Michael J. Solomon's class materials: CHE 696, 2003.

2.2 Introduction

Inspired by the vivid color of natural organisms such as the *morpho* butterfly[62,67], beetles[87], and fruits[88], one approach to produce color in artificial materials is to generate microscale periodicity that interferes constructively and destructively with incident light. This optical response is called structural color. In structural color, particular wavelengths of light are selectively propagated upon interaction with periodically arranged micron- or submicron-structures. Ordered arrays thereby can create iridescent colors[7,89], while amorphous structure produce non-iridescent colors[85,90,91]. Compared to synthetic dyes and pigments, materials displaying structural colors are relatively insensitive to photochemical degradation[92]. Some creatures such as chameleons[73] and squid[93] can manipulate their skin color using reversible structural color to serve biological purposes. Structural colors with high resolution and reversibility can lead to applications in displays[94–96], decorative patterns[82], automotive coatings[74], and sensors[97]. In these applications, structural color materials represent a coloration strategy with potential advantages in durability and sustainability[98].

Self-assembly is a promising method to produce structural color materials because it is scalable and versatile. Colloidal crystals, where the size of the building blocks is comparable to the wavelength of the visible light, can produce rich structural colors via constructive interference[7,64,82]. At both laboratory and manufacturing scales, self-assembly can be accelerated and controlled by the application of external fields, including DC electric fields[18,99,100], alternating current (AC) electric fields [20], and magnetic fields[21]. Evaporation can also drive deposition[16,17]. Among these methods, the application of DC electric fields – electrophoretic deposition – is an attractive self-assembly method because it performs well at low voltage and power. The microstructures produced are also reversible.

The most-common way in which colloidal self-assembly is used for structural color is in the production of three-dimensional crystals from particles of size 0.1-0.3 μm. The structural color is generated by Bragg reflection from the stacked crystal layers. In reflection, structural color intensity saturates as the number of layers grows. For polystyrene (PS) colloidal latex in air, for instance, the number of layers for saturation of the optical response is about fifty[16]. Liquid phase colloidal self-assemblies can be reconfigured by the controlled application of an external force. However, the optical intensity of these materials is commonly weaker than the structural color from fixed structures because of the relatively modest refractive index contrast between the particles and solvents commonly used for self-assembly[18]. For a light incident upon a crystal plane at a fixed angle, the structural color generated due to the Bragg condition is monochromatic; the power of the reflected ray is at that wavelength is concentrated at the corresponding specular angle[90,101].

An alternative method to produce structural color is through the mechanism of grating diffraction[7,82]. Grating diffraction structural color is iridescent, and multichromatic at a single incident light angle. It produces structural color at off-axis angles through a prismatic effect (cf. **Figure 2.1**a). In a study of *morpho* butterfly wings, a multichromatic band was observed in transmission because of grating diffraction by regularly arranged micro-ridges[62]. Similarly, a dual coloration mechanism – involving both Bragg reflection and grating diffraction – has been observed in beetles[102]. Gratings also function as anti-reflective surfaces in moth eyes[67,103]. Physically, grating diffraction differs from Bragg reflection in several critical ways[7,82]. In the former, the periodic spacing of the structure is in a direction normal to the incident light while in the latter the periodicity is parallel to the direction of incident light propagation. This difference is not fundamental to the interference mechanisms that underly the optical response; however, it

does lead to grating diffraction generating off-axis color for particle sizes that are significantly greater – in the range of 1 mm – than for Bragg's color, which is associated with sizes of about 0.1-0.3 mm. This difference in the required building block size is a critical feature; it opens the possibility of using new techniques for self-assembly and characterization for grating diffraction structural color relative to what is possible for Bragg reflection.

The application of self-assembly techniques to generate grating diffraction structural color has received less attention than the case of Bragg reflection; however, there are some reports in the literature. For example, colloidal crystals manufactured by direct-write assembly exhibit rainbow-like color via the grating diffraction mechanism[104]. Photonic balls, synthesized by self-assembly of colloids with different sizes on a sphere emulsion droplet, show optical patterns generated by a combination of Bragg reflection and grating diffraction[105].

Grating structural color therefore differs from Bragg's structural color. The structures are self-assembled from large sized particles and the optical response yields off-axis, prismatic structural colors. These differences are potentially advantageous and useful. For example, the larger particle size exceeds the Rayleigh resolution limit of optical microscopy (~ 200 nm in the object plane and ~500 nm along the axial dimension)[106]; using larger particle sizes can enable direct, microscopic characterization of the colloidal structures that generate the optical response. These self-assembled structures can also split wide-spectrum light into monochromatic beams propagating along different angles[107]. This prismatic effect is the function of a diffraction grating, and these optical components are widely used in spectrometers and monochromators[108,109]. Ways to manufacture diffraction gratings using soft matter include colloidal crystal films[110], liquid crystals[111–114] ,and microfluidic devices[115]. By herein using

electrophoretic deposition, we expand the capabilities of these materials to produce diffraction gratings with tunable structural color response.

The specific features of grating diffraction structural color from self-assembled colloidal crystals have not been the subject of fundamental investigation or modeling; the objective of this paper is therefore to address that gap and produce scientific understanding that can be used to design grating diffraction structural color by engineering the specific conditions of self-assembly. Colloids can interact with visible light and produce colors by Mie scattering[116]. Direct calculation of the structural color response from self-assembled materials has recently been demonstrated for structures varying from dilute[55] to compact[85]. Light scattering by colloidal crystals has also been well studied[117], but not been applied to predict this type of structure color. In this paper, we measure the grating diffraction structural color response of colloidal crystals and explain its characteristic features – including the particle size, layer thickness, and angular response – by modeling the results with scattering theory. By systematically varying the layer thickness and size of the building block as well as the angle of viewing, we also directly characterize the transition between the dominance of the Bragg reflection and the dominance of the grating diffraction mechanism. We thereby produce an operating diagram that can be applied to produce reconfigurable, self-assembled diffraction gratings from self-assembled colloidal crystals. The self-assembled structures are polycrystalline, and – interestingly – this property is critical to the azimuthal uniformity of the prismatic structural color. The unique features of grating structural color here demonstrated can be exploited in a variety of applications.

2.3 Methods

2.3.1 Preparation of Colloidal suspensions and direct current (DC) electric field self-assembly device

Sulfate modified polystyrene (PS) colloidal spheres were used for self-assembly and structural color measurement. As received, 1.0 μm particles (Thermo Fisher Scientific, S37498, Lot #2377255, 1.01 ± 0.02 μm in diameter, calculated surface charge density 0.6 μC/cm^2) were stabilized in water with sodium azide and surfactants. Before each experiment, particles were washed three times with deionized (DI) water by centrifugation. Then the particles were resuspended in dimethyl sulfoxide (Fisher Scientific) with 0.1 mM tetrabutylammonium chloride (TBAC), resulting in a stock solution volume fraction of 1.0%. TBAC was added to regulate the Debye length of the solution. To visualize the particles during self-assembly by confocal microscopy, we use fluorescent sulfate modified PS (Red 580/605) microspheres (Thermo Fisher Scientific) of the same size and surface chemistry.

An indium tin oxide (ITO) coated glass coverslip (~0.15 mm thickness, 70-100 W, SPI Inc.) were sonicated in acetone and isopropyl alcohol (Fischer Scientific) for 10 min, sequentially. The ITO slides were coated with poly(sodium 4-styrenesulfonate) (Sigma-Aldrich) by 15 min incubation in a 5 mg/mL aqueous solution of the polymer with 0.5M potassium chloride, followed by a rinse in DI water to remove residual salt. This step minimizes sticking of the particles to the substrate[99].

The device for electrophoretic deposition of the colloids (**Figure 2.6**b) was built following the method described in *Shah et al*[18]. The prepared particle suspension was injected until the chamber was filled (~10 μL). By wiring the two electrodes with stable DC voltage supply (Agilent E3616A), an electric field was generated by faradaic reactions at the electrode

surfaces. Deposition of the colloidal particles occurs by electrophoresis. For the present experiments, the applied voltage was 3.5V. This voltage was selected because it generates a rate of electrodeposition that promotes good quality crystallization, as per the analysis discussed in Kim et al.[33] and Ferrar & Solomon[32]. The number of layers was determined by the volume fraction of the solution loaded into the chamber, which varied between 0.32 vol.% and 4.8 vol.% in this study.

2.3.2 Optical measurement and spectroscopy

A spectrometer (HDX-VIS-NIR, Ocean Optics, Inc) was integrated into a custom designed apparatus allowing for simultaneous self-assembly and spectral characterization (**Figure 2.1**a). Briefly, unpolarized light generated by a Tungsten halogen illuminant (4.5 mW, HL-2000-FHSA-LL, Ocean Optics) was transmitted through an optic fiber and collimated (f = 15.01 mm, NA = 0.17) to provide a parallel beam (λ = 360-2400 nm). An anti-reflection arm that holds the fiber was connected to an optical rotation mount (Newport), which allows adjustment of the angle of the incident illumination. Similarly, a detection probe connected with the spectrometer was fixed on another optical rotation stage. The colloidal sample contained in the electric field self-assembly device was aligned with the center of rotation stage, with a fixed radial distance of ~20 mm between the sample and lens. By controlling both light incidence and detection positions, spectral data were acquired at variable angles relative to the sample. Spectra were collected 5 minutes after the application of the DC field, to allow for self-assembly to occur and for the structural color response to reach steady state. The spectral intensity was reported as diffraction efficiency, which normalized for the 2D scattering geometry and the incident light power with a factor of $2\pi r \sin(\theta_s) / d_{detc}$, where r is the distance between sample and the detector, and d_{detc} is the aperture diameter of the collimating lens.

2.3.3 CLSM imaging and analysis

CLSM (Nikon A1R, 100X oil immersion objective, NA=1.40) was used to visualize and characterize the self-assembly process and the colloidal crystal structures produced. Fluorescent sulfate-modified PS spheres suspended in DMSO are excited at 561 nm. The laser was turned off during self-assembly to eliminate laser-induced effects on self-assembly, as previously reported in the literature[33]. Images were captured in a shutter-flash mode to avoid this effect. The pixel size was 0.062 μm and the image size was of the 512 x 512 square pixels. Image volumes were also acquired to resolve the 3D crystal structure. Typically, 5 slices at a spacing of 1 μm were collected. The centroidal coordinates were determined by the open-source program trackpy[118],which was based on the method of *Crocker and Grier*[119]. The 2D radial distribution function (g(r)) was determined by five images captured at random lateral positions in the specimen (512 x 512 pixel), using Freud (open-source package) with a bin width of 0.8 pixel. In addition, the crystal diffraction pattern was determined by fast Fourier transform with Fiji.

2.3.4 Structural color characterization

The tristimulus values in CIE 1931 color space (X, Y, and Z) and the coordinates (x, y) in chromaticity diagram were calculated using the experimentally measured visible spectrum by open-source software (CIE1931xy.V.1.6.0.2). The color panel was plotted by the RGB triplet, which was converted from the determined CIE XYZ value by MatLab.

2.3.5 Spectral modeling from scattering theory

Light scattering modeling was performed by computing the form factor, $F(a, \boldsymbol{q})$, and structure factor, $S(\boldsymbol{R}, \boldsymbol{q})$. $F(a, \boldsymbol{q})$ was by direct calculation from Mie theory for the case of unpolarized incident illumination, and as implemented in Matlab (Section A.1). The form factor is calculated based on the following equation,

$$F(a, \boldsymbol{q}) = \frac{I_s}{I_o} = \frac{1}{k^2 r^2}\left[\frac{1}{2}(\boldsymbol{S}_1\boldsymbol{S}_1^* + \boldsymbol{S}_2\boldsymbol{S}_2^*)\right] \quad 2.1$$

Here, $\boldsymbol{S}_1$ and $\boldsymbol{S}_2$ are elements of the electric field amplitude scattering matrix. They depend on the scattering vector, $\boldsymbol{q}$, defined as $\boldsymbol{q} = \boldsymbol{k}_s - \boldsymbol{k}_i$, where $\boldsymbol{k}_i$ and $\boldsymbol{k}_s$ are the wave vectors of the incident and scattered light, respectively. $\boldsymbol{k}$ has a magnitude of $2\pi n/\lambda_o$, where n is the refractive index of the medium and λ_o is the light wavelength in vacuum. Therefore, $q = \frac{4\pi n}{\lambda_o}\sin\frac{\theta_s}{2}$, which is also a function of the scattering angle θ between $\boldsymbol{k}_i$ and $\boldsymbol{k}_s$. In this modeling approach, scattering angle and the particle size were independent variables. In addition, the number of terms computed in the Mie expansion was $\alpha + 4.05\alpha^{1/3} + 2$, where the dimensionless number $\alpha = k_i a$, as per Barber and Hill[120].

The structure factor $S(\boldsymbol{R}, \boldsymbol{q})$ was likewise computed by direct calculation of Equation 2.1, using the basis vectors of a FCC crystal lattice: $0, \frac{A}{2}(\hat{x} + \hat{y}), \frac{A}{2}(\hat{y} + \hat{z}), \frac{A}{2}(\hat{z} + \hat{x})$. Here, A, the cell length, is equal to $\sqrt{2}d$. Based on the interparticle spacing d and number of crystal layers, a perfect hexagonal packed layered lattice was constructed (i.e., inside **Figure 2.5**a). For other particle sizes modeled in **Figure 2.4**, the same ratio of d/d_p was kept constant at 1.13, while light incident angle θ_i and diffraction angle θ_d were varied, as shown in **Figure 2.6**b. One example of calculated structure factor using the definition (Equation 1.10) for a 1.0 μm PS, FCC, 3-layer crystal is shown in **Figure 2.5**.

To compute the spectral response in **Figure 2.5**a from Equation 2.2 we applied corrections based on the device geometry. These accounted for light reflection and refraction at the air-ITO glass interface; these corrections were computed from Fresnel's equation and Snell's law.

2.4 Results and Discussion

2.4.1 DC induced colloidal assembly and crystallization creates prismatic coloration

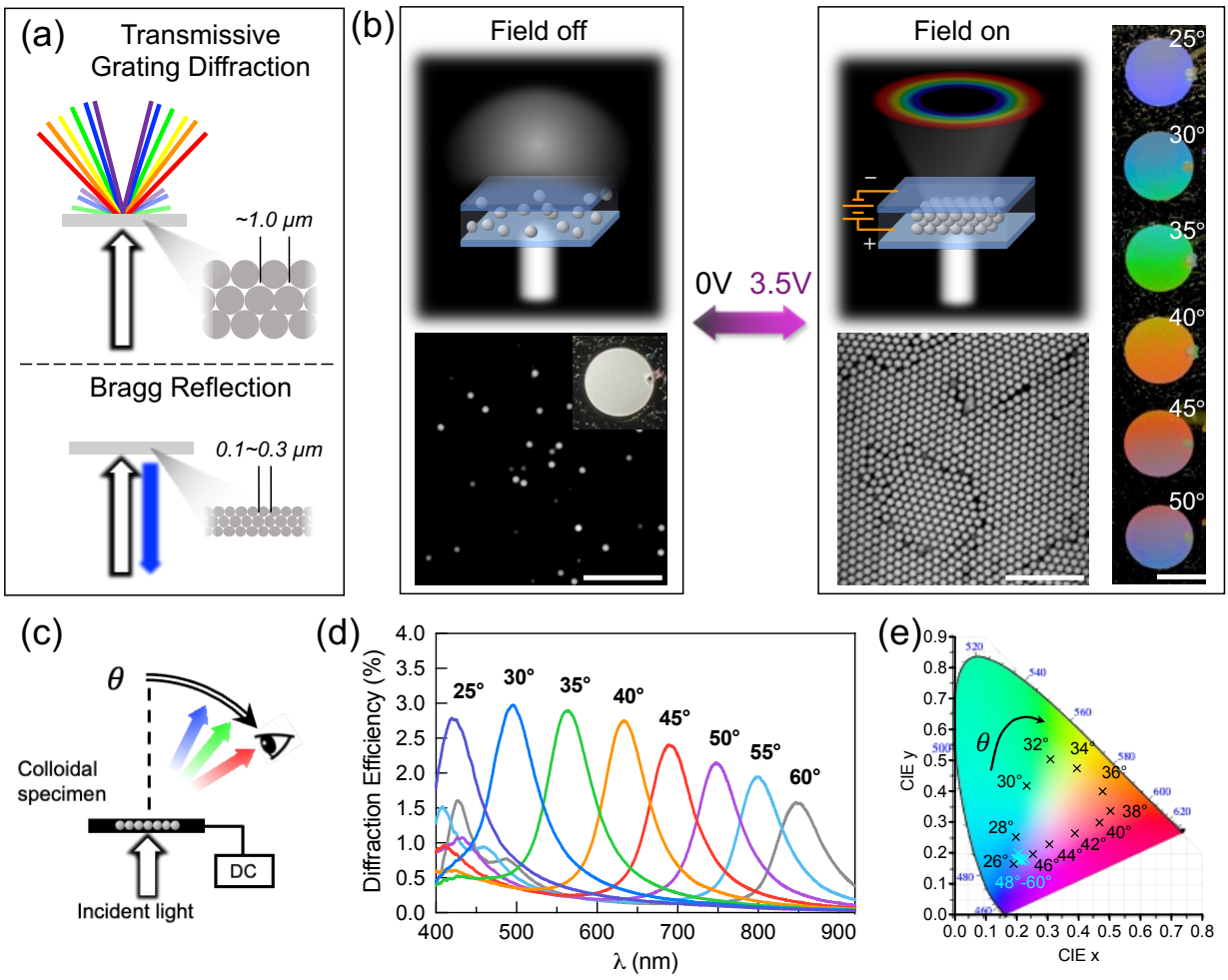


Figure 2.1: Angular dependent structural color of a self-assembled colloidal crystal composed of three layers of 1.0 μm PS spheres. (a) Schematic of two limiting mechanisms of structural color – transmissive grating diffraction and Bragg reflection. (b) Coloration and structural change due to self-assembly and crystallization, electric field device with particle suspension and CLSM image of the structure, image captured before and after self-assembly. Scale bar: 10 μm (for CLSM images), 5 mm (for device cell); labeled angles are as defined in the next panel. (c) Schematic of the transmission optics, showing the definition of the polar angle θ used for imaging and spectrophotometry. (d) Spectral response of the structural color at angles varying from 25° to 60°. (e) CIE 1931 chromaticity diagram showing the spectral measurements at various θ. The data for angles 48-60° involve second order diffraction; these points overlap and are shown in a different color.

The DC electric field (3.5V) induced self-assembly of 1.0 μm PS colloids yields ordered structures at the substrate after approximately 60 s of deposition (**Figure 2.1**b). The particles are initially dispersed at 1.0 vol.% in DMSO (with 0.1 mM TBAC), resulting in a three-layer crystal.

Transmission of collimated, unpolarized white light along an axis perpendicular to the device yields prismatic color. Prior to self-assembly, the specimen displays milky white color, due to scattering of the initially dilute colloidal dispersion. Upon application of the electric field, particles rapidly deposit and self-assemble into a highly ordered array, indicative of colloidal crystallization. Iridescent structural color is observed about 20 seconds after the field is applied. The structural color is reconfigurable by switching the potential between 0V and 3.5V. It can also be reconfigured between different peak wavelengths by changing the voltage (cf. **Figure 2.7**). By varying the polar angle θ – also the viewing/detection angle – the color response spans the full visible spectrum. At this particle size, the colors vary from violet to red as θ varies from 25° to 50° (**Figure 2.1**b; polar angle θ is defined in **Figure 2.1**c).

The specimen's transmission spectrum as a function of θ is reported in **Figure 2.1**d. The absolute diffraction efficiency, $\eta(\lambda, \theta)$, is the ratio of the diffracted beam intensity, $I_s(\lambda, \theta)$, to the total light incident power I_o (as described in Method). Here l is the wavelength of the spectral response. The peak wavelengths of the spectra agree well with the viewing angle dependent colors observed in **Figure 2.1**b. In addition, the intensity of the spectrum changes with θ. The diffraction efficiency of the device varied between 2.5 – 3.0% for this three-layer colloidal crystal over the angular range. The spectra display only a single peak – characteristic of first-order diffraction – at low viewing angles; however, for θ > 50° the primary diffraction peak shifts into the infrared (λ > ~780 nm) and a second peak (located at half the wavelength of the first order peak) emerges in the lower range of the visible region. The intensity of the second order peak is weaker than the primary peak by about 40% at the same wavelength. In **Figure 2.1**e, the chromaticity of the structural colors is displayed on a CIE 1931 diagram. The color

coordinates shift clockwise around the central (white) point of the diagram as the viewing angle is increased, ultimately completing one revolution around the diagram.

2.4.2 Effect of particle size and the polycrystalline identity on structural color properties

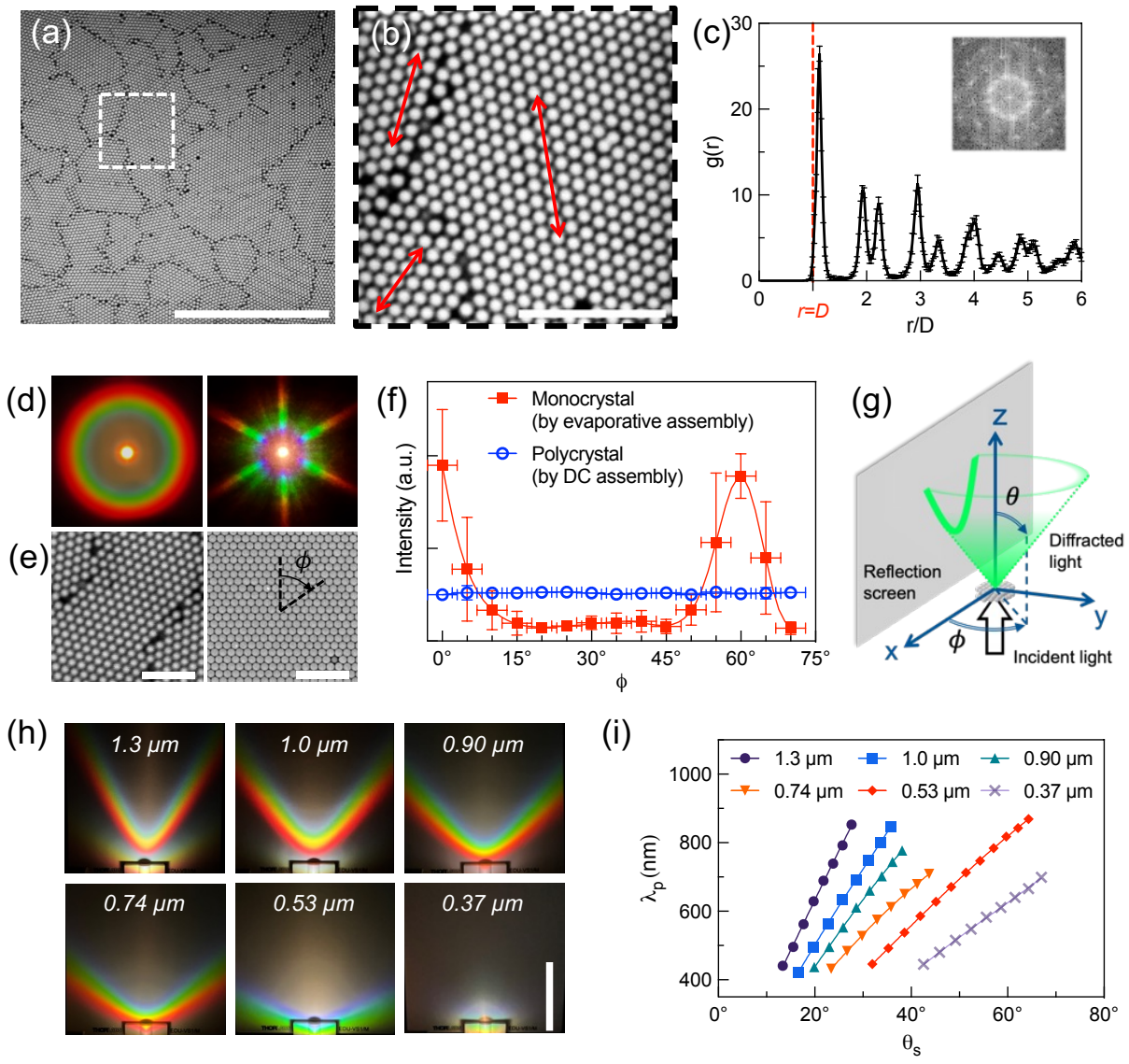


Figure 2.2: Angular dependence of the prismatic structural color. (a) CLSM image of the polycrystalline layer at the substrate for self-assembled 1.0 μm PS colloids. Scale bar: 50 μm. (b) A zoomed-in image of the boxed area in (a) showing the underlying close-packed structure of the crystal. The red dash line indicates different grain orientations of neighboring crystallites. Scale bar: 10 μm. (c) The 2D radial distribution function (RDF) of the crystal and its corresponding FFT image. (d) Polycrystalline structure that results in a white light diffraction pattern that is radially symmetric; single crystal structure results in a white light diffraction pattern with six-fold azimuthal symmetry. (e) Polycrystalline (CLSM image) vs. single crystal (SEM image) ordering that yields the differences in the previous panel. (f) The measured scattering intensity (at peak wavelength 435 nm) for both polycrystalline and single crystal structures as a function of azimuthal angle. (g) Schematic showing the polar angle θ, and azimuthal

angle ϕ of the measured diffracted light beam, with the hyperbola depicting the shape of the light emission captured on a vertical reflection screen as specified by the intersection of the screen with the emission cone. (h) Grating structural color projected onto a vertical reflection screen as per the geometry of the previous panel, showing its prismatic effect for particle diameters varying from 0.37 to 1.3 μm. Scale bar: 5 cm. (i) The peak wavelength of the spectral response at a function of scattering angle for different particle diameters.

The microstructure of the self-assembled colloidal crystal is instrumental to the establishment of the prismatic color. Interestingly, this microstructure can be directly observed using confocal laser scanning microscopy (CLSM) because of the 1.0 mm size of the colloid used in the self-assembly. **Figure 2.2**a reports CLSM images of the crystal structure; this image shows the bottom layer of the crystal. The ordered array is polycrystalline; different grain orientations are observable in the large-scale image of **Figure 2.2**a; the particle-level detail is available in **Figure 2.2**b. This panel shows that the packing has hexatic order. Crystallites with different orientations are separated into grains. The red lines depict the lattice orientations of three crystallites separated by grain boundaries. The 2D radial distribution function, g(r), of the colloidal crystal is shown in **Figure 2.2**c. The inset image is the fast Fourier transform (FFT) of the structure in **Figure 2.2**b; the 6-fold symmetry of the scattering is apparent. The periodic variation of g(r) and symmetry of the scattering pattern further confirm the hexatic ordering. From the first peak of the RDF, the average pair separation d, is determined to be 1.13 ± 0.05 μm for the 1.0 μm diameter colloids, as labeled in **Figure 2.2**e. This non-close packed configuration is consistent with the presence of screened repulsive interactions between the negatively charged particles.

We find that specimens with polycrystalline order yield structural color that is independent of the azimuthal angle ϕ of observation. This uniform color as shown in **Figure 2.2**d. On the other hand, single crystals, as self-assembled by the different method of evaporative deposition and imaged by scanning electron microscopy (SEM) (described by *Liu et al.*[16]),

exhibit strong azimuthal variation in the structural color intensity. The variability has six-fold symmetry, consistent with the Fourier transform of the single crystal structure (**Figure 2.2**e).

To quantify this difference, we report in **Figure 2.2**f the scattering intensity for blue color (435 nm peak wavelength) over the azimuthal angular range ϕ = 0°-70° (angle defined in **Figure 2.2**g). The results confirm that polycrystals exhibit uniform coloration. However, the single crystals show intensity variation, with peaks located at 0° and 60°. The uniformity of the azimuthal dependence of the structural color is useful and this property is predicated on the presence of polycrystallinity. Evidently the ensemble of grains in the polycrystalline specimens are randomly oriented; the resulting uniform distribution of lattice orientations leads to the uniform color intensity.

Figure 2.2i reports the effect of particle size on the prismatic structural color. In this experiment, we applied a DC electric field to self-assemble colloids with diameters varying from 0.37 μm to 1.3 μm. The initial particle concentration is fixed at 1.0% and an electric potential of 3.5 V was applied, except for the 0.53 μm and 0.37 μm particles, which required application of 4.0 V to produce stable crystallization. The measured spectra can be found at **Figure 2.9**. **Figure 2.2**h shows the resulting structural color projected onto a vertical screen. As shown in **Figure 2.2**g, the geometry yields a hyperbola-shaped rainbow, as expected for the intersection of a plane with the emission cone of the prismatic color. The specimen is located 1.5 cm away from the bottom of the image; higher vertical position on the image corresponds to lower scattering angle. The slope of the hyperbola's asymptotes decreases with smaller particle size. The vertex also moves downward, indicating that the prismatic band shifts to a greater scattering angle as the particle size is decreased. For large particle diameters (1.0 and 1.3 μm), a second order prismatic rainbow also appears. For smaller sizes, the primary prismatic rainbow appears lower on the

screen, until it almost vanishes for the 0.37 µm particle size. Quantitatively, **Figure 2.2**i reports the measured color peak locations for crystals consisting of different particle sizes. It shows that the peak wavelength of the structural color increases with the scattering angle. The slope of the effect is greater for larger particle diameters, yielding a spectral response over a narrower range of angles.

2.4.3 Effect of crystalline layer thickness on structural color properties

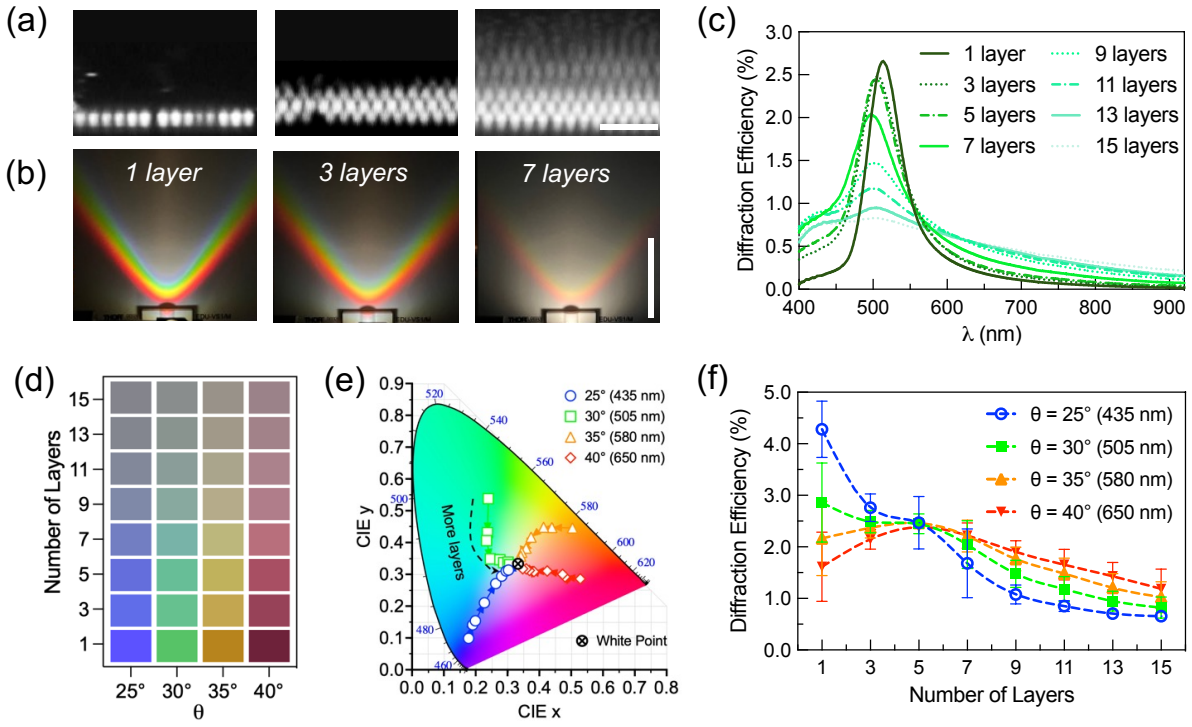


Figure 2.3: Layer dependence of the prismatic structural color. (a) CLSM images show the layered structure of the self-assembled crystal for, from left to right, 1, 3, and 7 layers, as generated by self-assembly of suspensions with volume fraction of 0.32%, 1.0%, and 2.3% respectively. Images are acquired in a plane perpendicular to the bottom substrate. Scale bar: 5 µm. (b) The grating structural color projected onto a vertical reflection screen, with number of layers as in panel A. Scale bar: 5 cm. (c) The spectral response measured at θ = 25° (green: 505 nm) as number of layers is varied from 1 to 15. (d) Spectrum-converted colormap shows structural color at θ varying from 25° to 40°, respectively. (e) CIE 1931 chromaticity diagram showing the saturation loss by increasing the layer thickness. (f) Peak spectral intensity at different layer thickness for θ varying from 25° to 40°.

The crystalline layer thickness of the self-assembled structure can be precisely controlled by varying the initial concentration of the suspension that undergoes self-assembly. **Figure 2.3**a reports cross-sectional confocal microscopy images of the microstructure generated by the DC

electric field self-assembly of 1.0 μm spheres. We also characterized the structure of each layer for a 7-layer crystal (**Figure 2.8**). It shows that the quality of crystal ordering in the top layer is less than the bottom layers. The deposited structures are crystalline with layer thickness proportional to the initial concentration of the loaded solution, which varies in volume fraction from 0.32% to 4.8%. The layer thickness affects the structural color, as reported in **Figure 2.3**b. The images again show the diffracted light projected onto a vertical screen. The color bands become less intense and distinguishable with increasing layer thickness. At the same time, the intensity of the diffuse scattering above and below the diffracted color band increases. Roughly, for this particle size, the colors blue (435 nm), green (505 nm), yellow (580 nm) and red (650 nm) appear at polar angles of 25°, 30°, 35° and 40° respectively, independent of layer thickness. **Figure 2.3**c reports the measured spectral response at θ = 30° (505 nm) for specimens with layer number ranging from 1 to 15. We observe that by increasing the layer thickness, the peak wavelength (λ_p) remains almost unchanged (variability of less that 5%), while the intensity drops nonlinearly. Thus, the hue (λ_p) is independent of the layer number; however, the brightness (diffraction efficiency) is dependent.

To show the color appearance, we convert the spectral response at angles of 25-40° to the RGB color space and plot them in **Figure 2.3**d. As layer number is increased color appearance transitions from high to low saturation. We can also discover this feature from **Figure 2.3**c, as higher peak intensity and narrow band width indicate higher color saturation. This trend is quantitatively shown in the CIE 1931 color space of **Figure 2.3**e. A point closer to the boundary indicates higher color saturation, while the central white point means zero saturation. For all channels, the CIE coordinates move towards the white point as the layer thickness increases. This behavior supports the trend of structural color saturation variation. However, as reported in

Figure 2.3f, brightness, as quantified by the peak spectral intensity, varies with scattering angle. At θ = 25° (blue) the peak intensity monotonically decreases. At θ = 30° (green), a plateau in intensity at 3-5 layers appears; this plateau transitions to an intensity maximum at about five layers for θ = 35° (yellow) and 40° (red). Although the layer thickness yielding the brightest color varies with the scattering angle (and therefore color channel), the monolayer crystal always provides the highest saturation. These data allow precise design of color brightness and saturation through the control of layer thickness.

2.4.4 Mie scattering modeling of diffraction spectral response

Because the prismatic color is observed for colloidal crystal monolayers and generally decreases in intensity as layer number is increased, we hypothesize that the mechanism for the effect is grating diffraction. To substantiate this hypothesis, we model the optical response by light scattering theory. The approach has the benefit of quantifying size, angle, and layer number effects. Briefly, total scattered light intensity I_s is given by (vectors and matrices are bolded),

$$I_s = N \cdot F(a, \boldsymbol{q}) \cdot S(\boldsymbol{R}, \boldsymbol{q}) \qquad 2.2$$

where N is the total number of particles in the structure, $F(a, \boldsymbol{q})$ is the Mie form factor, calculated as per Equation 1.10 and $S(\boldsymbol{R}, \boldsymbol{q})$ is the structure factor, calculated as per Equation 1.8. Details of the modeling approach can be found in the methods shown in **Figure 2.10**.

Here, the Mie form factor $F(a, \boldsymbol{q})$ describes the scattering of light by a single dielectric sphere, where a is the particle radius and $\boldsymbol{q}$ is the scattering vector. $\boldsymbol{q}$ is determined by the characteristics of the incident illumination, including its scattering angle and wavelength. $S(\boldsymbol{R}, \boldsymbol{q})$ is the structure factor, determined by the crystalline lattice structure,

$$S(\boldsymbol{q}) = \frac{1}{N}\sum_{j=1}^{N}\sum_{k=1}^{N} e^{-i\boldsymbol{q}\cdot(\boldsymbol{R}_j - \boldsymbol{R}_k)} \qquad 2.3$$

Here, $\boldsymbol{R}$ are the positions of the lattice sites. The detailed lattice modeling and structure factor calculation, using face centered cubic (FCC) lattice vectors, can be found in methods and **Figure 2.10**.

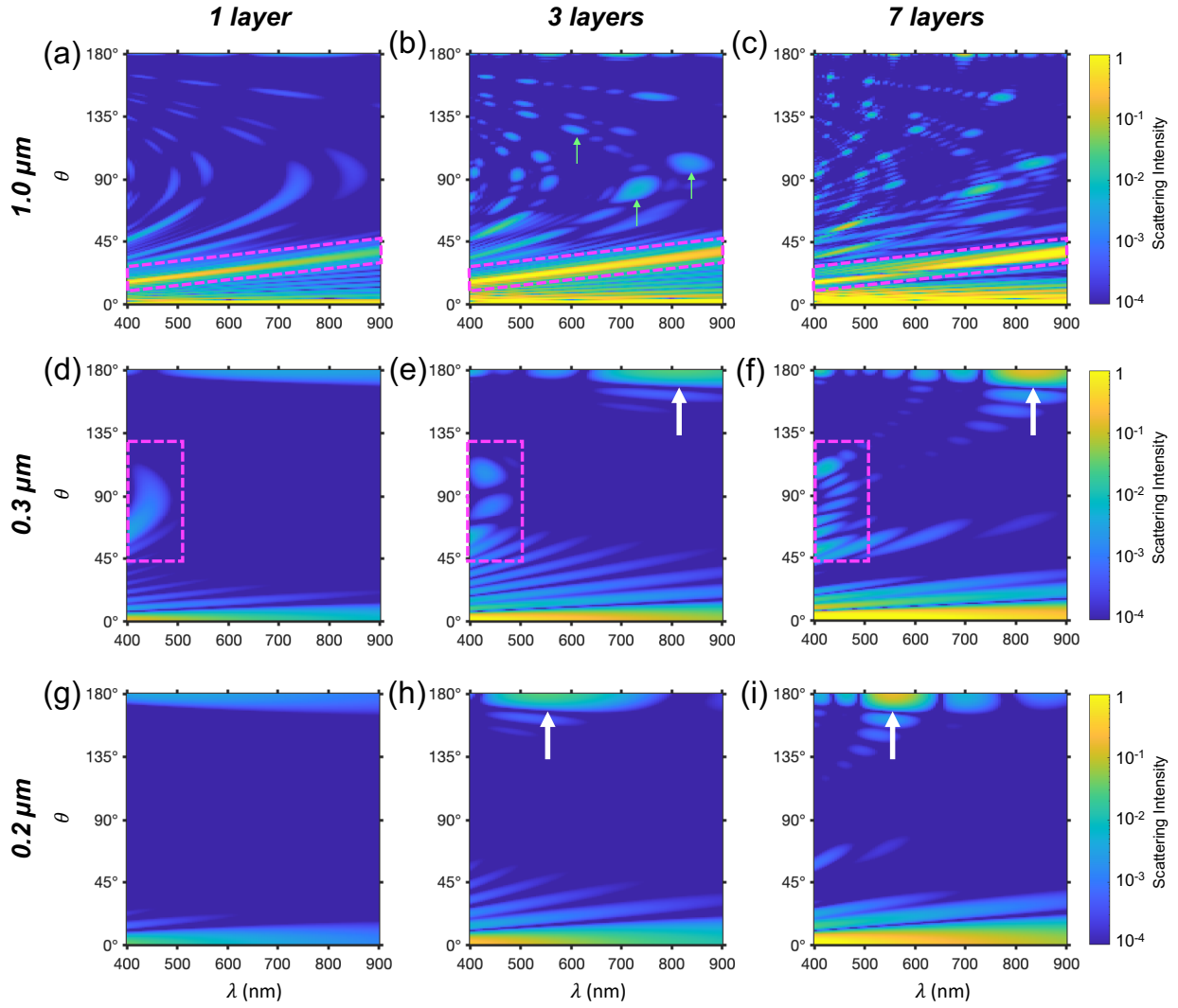


Figure 2.4: Light scattering modeling of the angularly dependent spectral response at different self-assembled particle sizes and layer thicknesses. Surface plots of scattering intensity at various polar angles (θ = 0-180°) and wavelengths (λ = 400-900 nm), with selected particle sizes of 0.2, 0.3 and 1.0 μm, and layer numbers of 1, 3 and 7, respectively. The regions of interest identified (boxes: grating diffraction; white arrows: Bragg reflection; and green arrows: discrete peaks) are described in the text.

To account for the polycrystalline structure of the specimens (**Figure 2.2**a), the intensity is integrated and averaged over all azimuthal angles (ϕ), consistent with a uniform probability distribution of the crystallite orientation. Results of the modeling are reported in **Figure 2.4**i. The panels report a matrix of representative cases of $d_p = 2a$ = 1.0, 0.3 and 0.2 μm and layer number of 1, 3 and 7. Each panel maps the scattered intensity, I_s, in arbitrary units, on a log scale as a function of polar angle θ (varying from 0-180°) and wavelength λ (varied from 400-900 nm).

In **Figure 2.4**a (1.0 μm diameter), there is a line of high scattering intensity (indicated by the region of interest bounded by the pink dash line). This line is consistent with first order grating diffraction. Specifically, it displays an off-axis and iridescent optical response; the peaks occur neither at the reflection (θ = 180°) nor transmission (θ = 0°) angles.

The region of high scattering intensity is also apparent at greater number of layers (cf. **Figure 2.4**b and c). However, in this case the grating effect is modulated by multilayer interference; the result is a set of discrete peaks within the grating diffraction band. A sampling of these peaks is labeled by green arrows in **Figure 2.4**b. The discrete peaks observed at angles larger than about 40° are more than 100 times weaker than the primary band; they arise due to constructive interference at other grating spacings. The resulting structural color response is thus the net effect of grating diffraction and multilayer interference. Within the visible wavelength range of ~380-750 nm, the first order peaks are located at a transmission angle of 20°-40° for all layer thicknesses, and their peak wavelengths (λ_p) are independent of layer thickness (**Figure 2.4**a-c). However, the intensity of the response does vary with thickness. We also note that a bright band always appears at the transmission angle (θ = 0°), due to forward scattering. Even though the intensity is strong, the scattered is non-selective, and therefore devoid of coloration.

Reducing the particle size to 0.3 mm (cf. **Figure 2.4**d-f) has the following effects: First, the angularly dependent band of high intensity – consistent with grating diffraction – is observed, as for large size particles; however, the peak locations are shifted to wavelengths less than 500 nm. The intensity also decreases. Second, the spectral response of multilayer effect appears, as labeled by the white arrow. This effect is most intense at the specular angle (θ = 180°); the effect also increases with layer thickness. Interestingly, the two coloration mechanisms – grating diffraction and multilayer effect coexist in this size range.

If the particle diameter is further reduced 0.2 μm (**Figure 2.4**g-i), which is a typical size selected to generate the usual kind of Bragg reflection structural color in a colloidal crystal, further changes are observed. First, a strong Bragg's peak is now observed in the visible region, as indicated by the white arrow. This reflection peak is at around 570 nm, and at the specular angle of 180°. (This is close to 575 nm, the Bragg's law prediction for first order diffraction.) Second, the first order grating diffraction band observed for larger particle sizes moves from the visible region to the UV region. Third, comparing **Figure 2.4**g-i, the optical intensity grows rapidly with layer thickness; this growth is the opposite of grating diffraction observed for larger size particles.

Figure 2.4 therefore offers a comprehensive view of interference effects yielding structural color in thin colloidal crystals of variable particle size. It bridges between the two limiting cases of Bragg reflection and grating diffraction. This transition from a predominant grating effect (**Figure 2.4**a) to a purely multilayer effect (**Figure 2.4**i) depends sensitively on particle size and number of layers. The optical phenomena discussed in this manuscript are all different limits of the general solution to the scattering of light from ordered, colloidal structures. These optical phenomena manifest at specific strengths and wavelengths based on the size of the

colloids and the refractive index properties of the system. The results provide theoretical understanding of the interrelationship between these structural coloration mechanisms in colloidal crystals, and therefore are generally applicable to the design of structural color materials. For example, the refractive index of materials used for particles and solvent can be tuned to identify its effect on structural color.

2.4.5 Modeling of grating diffraction over wide range of particle sizes and layer thickness

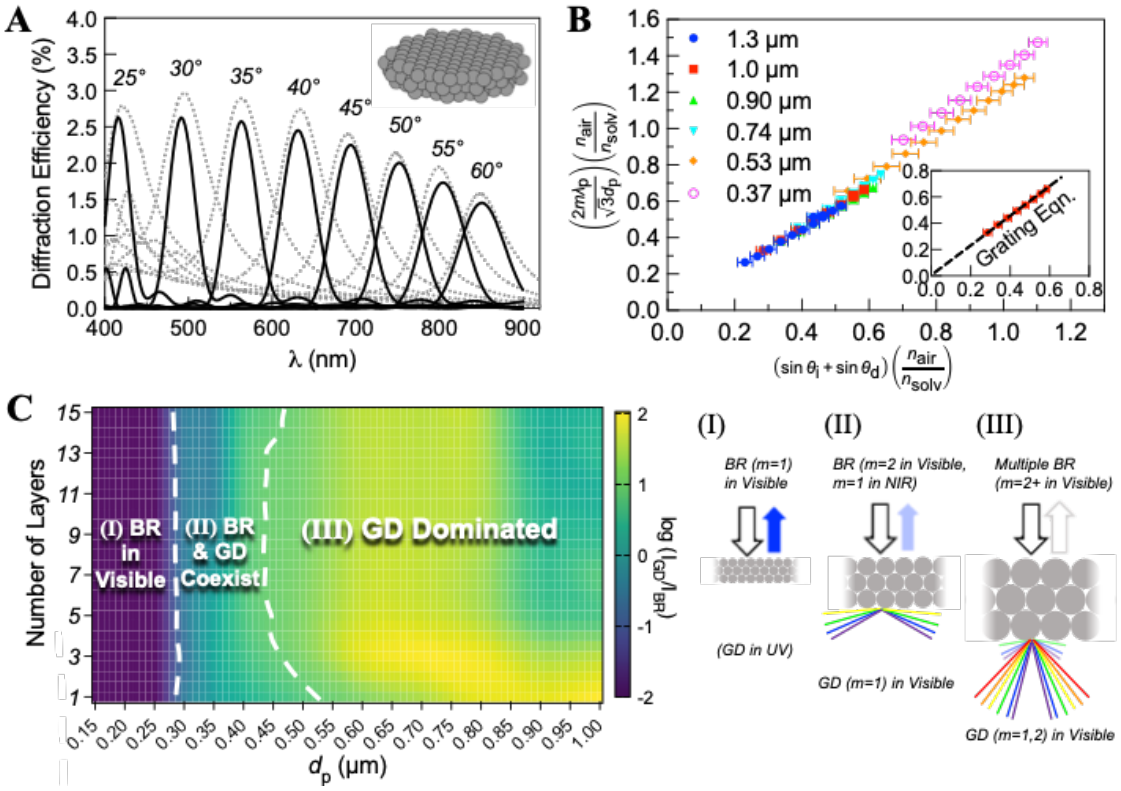


Figure 2.5: Operating ranges for grating diffraction and Bragg reflection structural color. (a) The simulated spectrum for a three-layer colloidal crystal comprised of 1.0 μm particles (solid curves) plotted with the experiment measurements (dash curves). (b) Correlation of the experimentally measured peak wavelength with dimensionless groups suggested by the diffraction grating equation, for particle size of 0.37-1.3 μm, and for first and second diffraction orders. The inset plot shows the agreement between experiment and theory for the diffraction wavelength of crystals with 1.0 μm diameter colloids. (c) Structural color modeled intensity diagram shows the effect of particle size and number of crystal layers on structural color mechanism – Bragg reflection (BR) and grating diffraction (GD). The dash lines indicate the boundary between the three regions. In Region I: Only BR color is visible; GD is shifted into the UV (non-visible). In Region II: 1st order BR is shifted into the NIR, while the 2nd order BR is in the visible range (but with weak intensity); the 1st order GD yields visible color. In Region III: 1st and 2nd order BR are shifted into the NIR and multiple higher order BR are in the visible; the multiple reflections yield diffuse (milky) color; the 1st order GD generates full prismatic color, while the 2nd order GD provides such color but with lower intensity.

In **Figure 2.5** we quantitatively compare the experimental and theoretical results to establish grating diffraction as the mechanism for the observed prismatic color and to provide a comprehensive explanation of how this structural color varies with particle size, scattering angle, and number of crystalline layers. The full spectral response of the theoretical model is reported in **Figure 2.5**a. It reports the angularly dependent structural colors for a three-layer colloidal crystal with an interparticle spacing of 1.13 μm. (This spacing is determined from the RDF in **Figure 2.2**c). The computed optical response (solid curves) agrees well with the experimental results (dash curves).

The 2D colloidal crystal itself can be conceptualized as a hexagonal, evenly spaced multiple-slit 2D grating. Because of the hexatic ordering, major gratings with a spacing of d are in three diffraction orientations. The diffraction of light by 1D gratings, described by the Huygens-Fresnel principle in the multi-slit geometry, is modeled by the grating equation[75],

$$m\lambda_p = D(\sin\theta_i + \sin\theta_d) \qquad 2.4$$

This equation is characterized by dimensionless variables: $2m\lambda_p/\sqrt{3}d_p$ and $(\sin\theta_i + \sin\theta_d)$, where $d_p = 2a$ is the particle diameter, and $D = \sqrt{3}/2d_p$ is the close-packed grating spacing due to hexagonal geometry. Even though the grating equation describes diffraction from a 1D structure, the prismatic structural color observed is also a good description for the 3D crystals studied here. That is because each plane functions as its own grating and – as discussed in **Figure 2.4** – interference between the different layers is not the dominant contribution to the optical response.

As shown in **Figure 2.5**b, the variation of the peak wavelength with particle diameter collapses onto a master curve by means of Equation 2.4. The master curve behavior is quite precise; however, the results for the smaller particle sizes show some deviation. This discrepancy

is because the particle spacing is slightly larger than d_p, as assumed in the theory comparison. The particle spacing is expanded (cf. **Figure 2.2**b-c) because of repulsive charge interactions between the self-assembled particles. For example, the interparticle separation of the colloidal crystal self-assembled from 1.0 μm diameter particles is 1.13 μm, as per the RDF of **Figure 2.2**c. When this separation is used in Equation 2.4, the agreement between theory and experiment is nearly exact; the average relative error is just <3%.

Figure 2.5c identifies the conditions under which Bragg reflection or grating diffraction is the dominant contribution to the optical intensity in visible structural color. When referenced to a particular range of the optical spectrum – here the visible range – whether the intensity of one optical phenomenon dominates the other will depend sensitively on the size and refractive index. That is, when referenced to a specific wavelength range, some of the optical phenomena will not be observed, because their contribution to the scattering response occurs outside the wavelength range of visible light. The data for **Figure 2.5**c is extracted from calculations based on experiment, for a macroscopic, cylindrical FCC colloidal crystal, with a specimen diameter of 6 mm. The incident light direction is fixed and perpendicular to the FCC (1,1,1) plane. The plot is an interpolated heat map of the relative intensity ($I_r = I_{GD}/I_{BR}$) as a function of particle size and layer thickness for self-assembled PS colloidal crystals in DMSO. Here, we define the structural color as dominated by grating diffraction if $I_r > 10$; Bragg reflection is dominant if $I_r < 0.1$. In the intermediate case, $0.1 < I_r < 10$ both coloration mechanisms are important. **Figure 2.5**c shows that the transition between the different regimes is primarily a function of particle size. Based on the modeling, GD is in UV wavelength when the particle size is in range about 0.15-0.28 μm (regime I), therefore all visible structural colors are produced by BR. As size is increased, the regime transitions from BR to the intermediate case (regime II) to GD (regime III).

However, the transition to a GD dominant response is more dependent on layer number than the other two transitions. In regime II and III, 1st order BR shifts to Near-Infrared Light (NIR); higher order BR is still in the visible range but with weaker intensity. Note the extent of the BR and GD regimes; there are broad ranges of particle sizes in which GD dominates. The extent of the contribution of GD to the structural color response has been unrecognized in the literature. We note that for crystals of larger particle sizes and thickness (region surrounded by the white dash line), the response here is complex; although the GD peak continues to dominate, the overall intensity is modulated by multiple higher order BR peaks. The diffuse color likely results from multiple BR peaks in the visible region. The combined response is therefore a GD signal on a multispectral BR background.

Figure 2.5c modeling maps the two limiting structural color mechanisms onto an operating diagram; the diagram could be easily generated for different types of combinations of solvent and particle material composition.

2.5 Discussion

This study has demonstrated reconfigurable structural color generated via grating diffraction of a thin colloidal crystal as self-assembled by a low-power DC electric field. We report the effect of the particle size, layer thickness, and polycrystallinity on the prismatic response, including the intensity, wavelength, and saturation of the structural color. Unique features of the colloidal crystal microstructure – both the micron-scale size of the self-assembled particles and the polycrystalline nature of the ordered lattice – promote high quality structural color by grating diffraction.

The 3D crystals self-assembled by the applied DC electric field exhibit prismatic structural color. This optical response differs from the more common type of structural color

from Bragg reflection. Grating diffraction structural color is dominant in crystals self-assembled from colloids with particle size of ~0.4-1.0 μm; this is more than twice the typical size for Bragg's structural color. This difference is directly related to the physics of the constructive interference that generates the optical response. The condition for constructive interference occurs for periodicity of ½λ for Bragg's reflection, while it is λ for grating diffraction (cf. Equation 2.4). This is because different optical path lengths are required for constructive interference by these two mechanisms. This difference in the required particle size for grating diffraction and Bragg reflection is of critical importance to structural color applications. Larger particles (d_p > 0.4 μm) produce prismatic effect and off-axis transmissive color through grating diffraction; smaller particles produce monochromatic and specular reflective color through Bragg reflection. Both types of structural color are angularly dependent with distinct features (**Figure 2.11**).

This study has focused on prismatic structural color in thin films of self-assembled colloids. While both transmissive and reflective prismatic response were observed, we focused our study on the transmissive color because its intensity was the strongest. **Figure 2.3**f showed that the diffraction efficiency progressively declined with layer number. Although some of this decline is captured in the model (cf. **Figure 2.4**) as a combination of grating diffraction and multilayer effects, an additional contribution that is not modeled is multiple scattering; this effect is likely the major contributor to the diffraction efficiency decline, especially for crystals of five or more layers. As illustrated by **Figure 2.8**a, we believe that the bottom crystal layers adopt an FCC structure. Some disorder is observed in the of top layer. This disorder likely contributes to reduced saturation and peak prominence. The degree of ordering of the thicker crystal remains strong; however, the optical response becomes less intense and more diffuse. As the crystal layer

thickness increases the optical path length increases, and multiple scattering becomes more prevalent. Multiple scattering decreases the peak diffraction efficiency and increases the diffuse background, resulting in a lower prominence of the peak optical response. It is certainly a factor to consider in designing high quality structural color produced in transmission. The approach of directly computing the structure factor used in this study, could, in future work, be extended to include the calculation of multiple scattering[91,121]. However, the light scattering modeling satisfactorily determines the structural color response of thin films.

This modeling method incorporates both the Form factor and structure factor. By comparing **Figure 2.10** a and b to c, the peak location across various aq is primarily determined by structure factor. This observation indicates that the peak wavelength measured in the colloidal crystal is more closely related to the arrangement of particle positions, as described by the structure factor. However, Mie scattering also plays a significant role in influencing the absolute intensity of the diffracted light and the relative peak heights observed at different angles. This effect can be discerned by comparing spectra measured for particles of varying sizes shown in **Figure 2.9**. For example, when comparing spectral peaks at low wavelength (~450 nm) and higher wavelength (~650 nm), smaller particles (e.g., 0.37 μm) can diffract relatively more blue light than the red light. This behavior likely arises due to differences attributed to Mie scattering effects.

An additional effect that could be addressed in future work is the role of defects. Defects produced during self-assembly may affect the grating diffraction optical response in ways that are analogous to the case of Bragg reflection.[16] Effects in the latter instance have been studied using finite-difference time domain (FDTD) methods, and that approach could in future work be applied to grating diffraction colloidal crystals. It would also be beneficial in future work to

model the optical response of imperfect crystals to predict the effects of defect structure on the structural color produced by the grating diffraction mechanism.

A key feature of the structural color reported here is that the spectral response is azimuthally uniform. **Figure 2.2** demonstrates that the polycrystallinity of the self-assembled crystal is responsible for this uniformity. Crystal growth, initiated by the random sequential deposition of colloids as they deposit under the electric field, yields ordered arrays nucleated at different sites and with various orientations. The simultaneous growth of these regions yields the confluent, polycrystalline structure observed in this study. Randomly oriented crystal grains of finite size are therefore advantageous to the optical effects. This is noteworthy because the goal of self-assembly is often to achieve a crystal of the highest possible quality – ideally a single crystal. However, in the present case polycrystallinity is actually a desired outcome. The situation suggests that here is a level of polycrystallinity representing an optimal balance of color uniformity (promoted by polycrystallinity) and color intensity (hindered by polycrystallinity). Finding this optimum in color performance could be the subject of future study. This effect, as well as other consequences of crystal quality on optical response, could be studied by varying the applied voltage. Such a change would affect the rate of electrodeposition, which would in turn affect crystal quality.

The use of larger particles for structural color application – here 1.0 mm in size – also yields some notable advantages. They include: the ability to directly visualize with CLSM the time-dependent, particle-level structure that generates the color; and, the applicability of the DC electric field deposition method, which is both programmable and reconfigurable. This deposition method performs well for micron sized colloids because in this regime the convective effect of electrophoresis is slightly greater than the randomizing effect of Brownian motion. A

final advantage of the grating diffraction mechanism of coloration is that the colloidal crystal film that generates the effect is thin; less than five layers is needed to reach maximum diffraction efficiency.

There are various ways to produce gratings, including using lithography[109] and self-assembly of soft matter[110–114]. Gratings produced from soft matter in liquid media are reconfigurable but display relatively modest diffraction efficiency[112] For example, after optimizing applied voltage, illumination, and cell thickness, electrically controlled liquid crystals with nematic order have generated diffraction efficiency as large as 12.5%[113] and 30%[114] depending on grating design. For the electrophoretically deposited gratings using spherical colloids studied here, the maximum diffraction efficiency is about 4.5%, likely due to low refractive index contrast and energy loss at device interfaces. Additional optimization would be possible, particularly by varying the properties of the solvent and colloid, as well as potentially, the crystal spacing and lattice structure[25].

2.6 Conclusions

In conclusion, grating diffraction structural color with high brightness and saturation can be produced in thin films (1-5 layers) from large particles (~ 1 μm) by a self-assembly method that can be finely tuned (electrophoretic deposition). These tailored features of self-assembly method, particle size, and layer thickness can lead to structural color materials useful in applications such as anticounterfeiting, antireflection coatings, filters, and spectrometer gratings. The experiments, modeling, and operating diagrams reported here can be applied to design grat

2.7 Supplementary Information

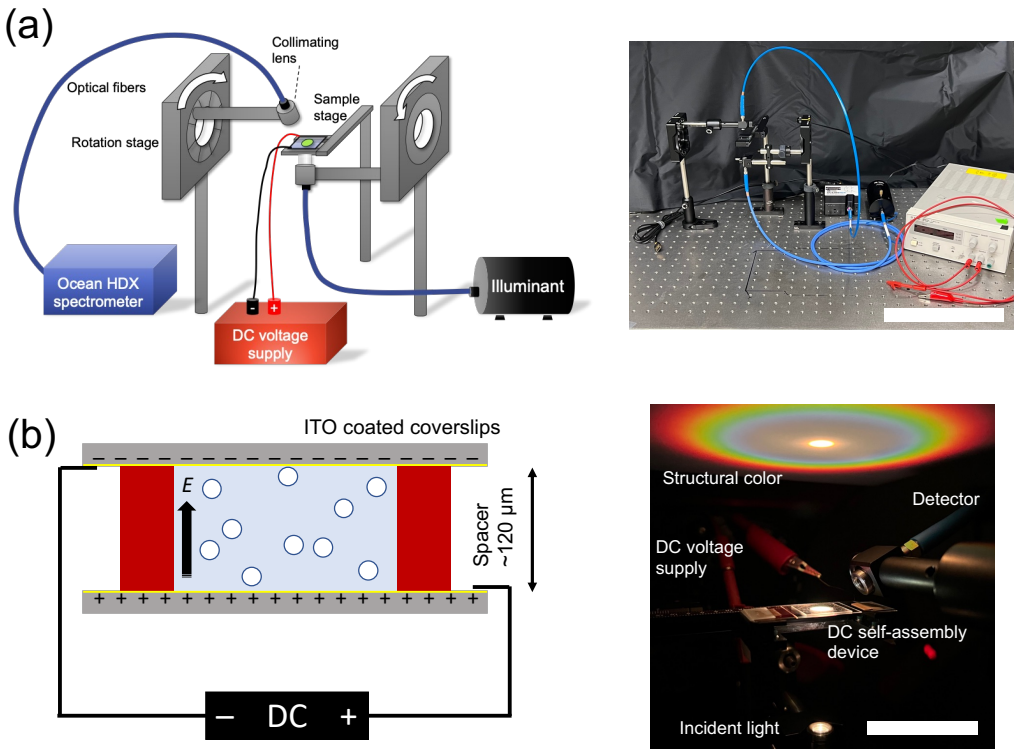


Figure 2.6: Experimental Setup. (a) Custom designed apparatus to measure optical spectrum from a colloidal sample at different angles, schematic diagram (left) and device image (right). Scale bar: 20 cm. (b) DC self-assembly device, schematic diagram (left) and device image on sample stage after self-assembly (right). Scale bar: 5 cm.

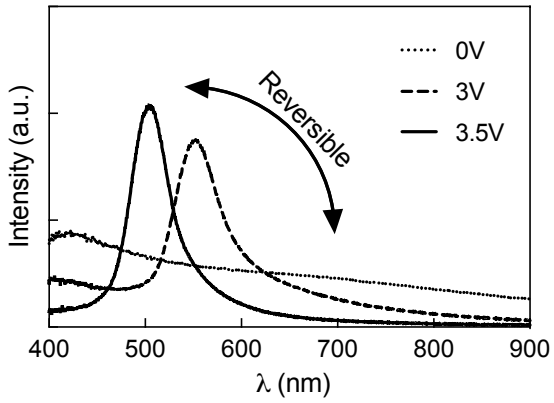


Figure 2.7: Reconfigurable Structural Color Spectral Response. The grating structural color (measured at θ = 30° for colloidal crystals assembled by 1 µm particle) shows high reconfigurability by switching the voltage between 0V, 3V, and 3.5V.

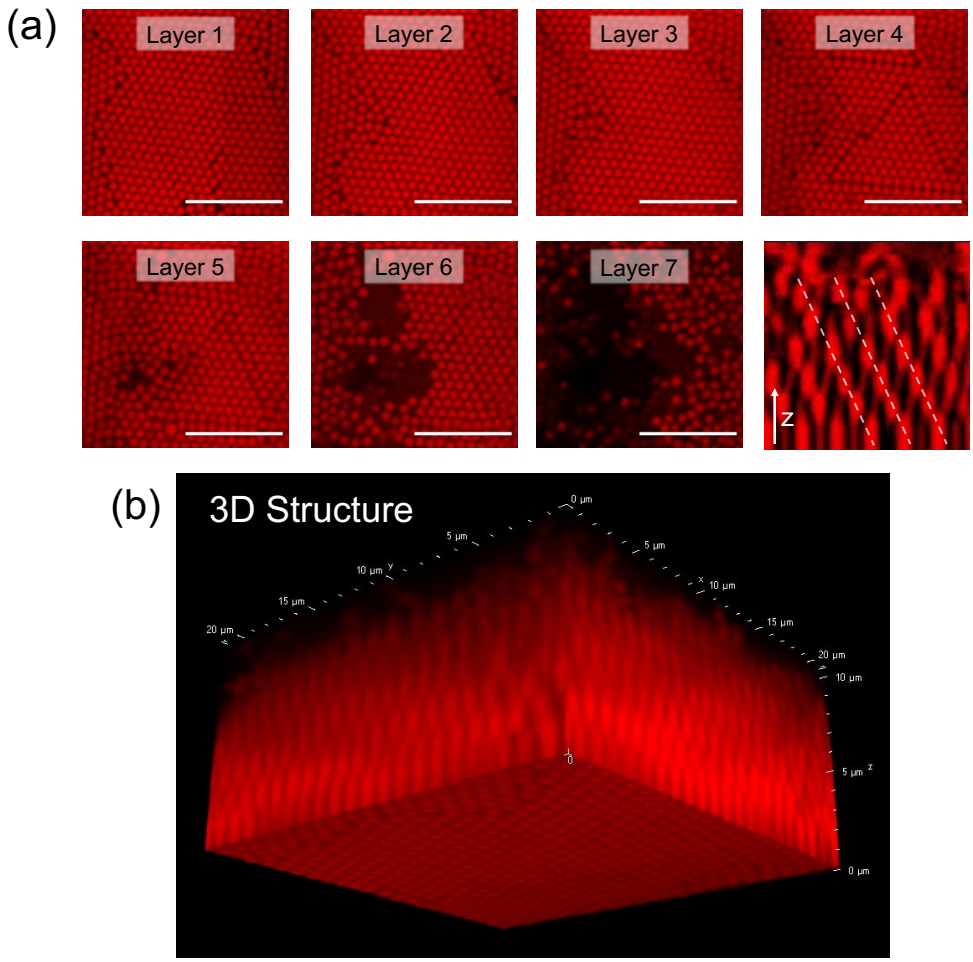


Figure 2.8: 3D Structure of DC Electric Field Assembled Colloidal Crystal. (a) Z-stack confocal image of the colloidal crystal structure from the bottom layer (Layer 1) to the top (Layer 7) for a 7-layer colloidal crystal. Scale bar = 10 µm. The cross-sectional image shows (110) plane of the FCC crystal structure. Arrow length = 2 µm. (b) 3D view of the structure.

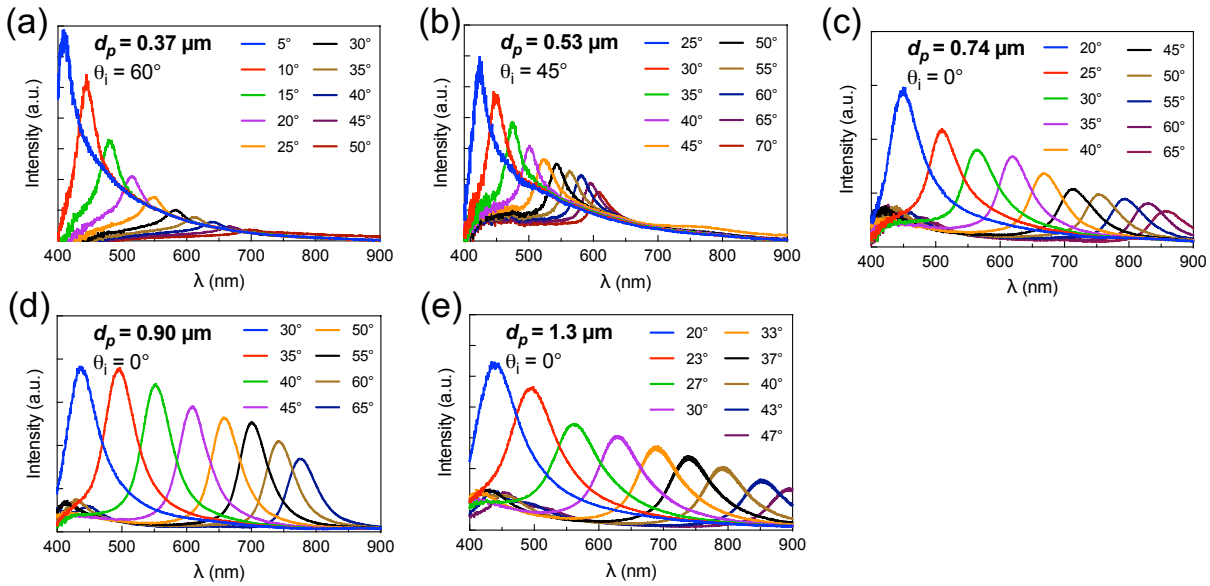


Figure 2.9: Raw spectra of angle dependent structural color, measured for colloidal crystals with particle size d_p of 0.37, 0.53, 0.74, 0.90, and 1.3 μm, respectively. Light incident angle θ_i is fixed for each set of measurement, while the diffraction angle θ_d varies as in the legend. These spectra are converted to diffraction efficiency for main text plots as per the Methods.

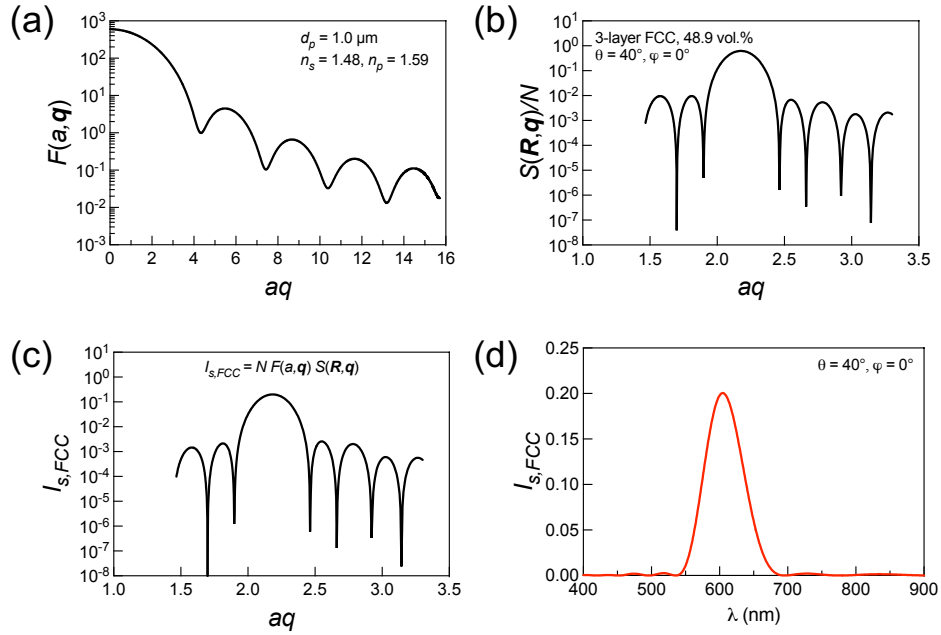


Figure 2.10: Performance of light scattering modeling. These figures report calculations that are components of the optical spectrum calculations reported in the main text. (a) Mie scattering form factor for 1.0 μm polystyrene spheres in DMSO. (b) Structure factor for a 3-layer FCC crystal with 183 particles (1.0 μm diameter), at scattering angle θ = 40° and azimuthal angle ϕ = 0°. The interparticle distance is 1.13 μm and the volume fraction is 0.489. (c) Calculated scattering intensity from the product of the form factor and structure factor in (a) and (b), using Equation 2.1 and 2.3 of the main text. (d) Structural color spectrum plotted as scattering intensity vs. wavelength (converted from q by its definition), for the wavelength range 400-900 nm, indicating a red color predicted at θ = 40° and ϕ = 0°.

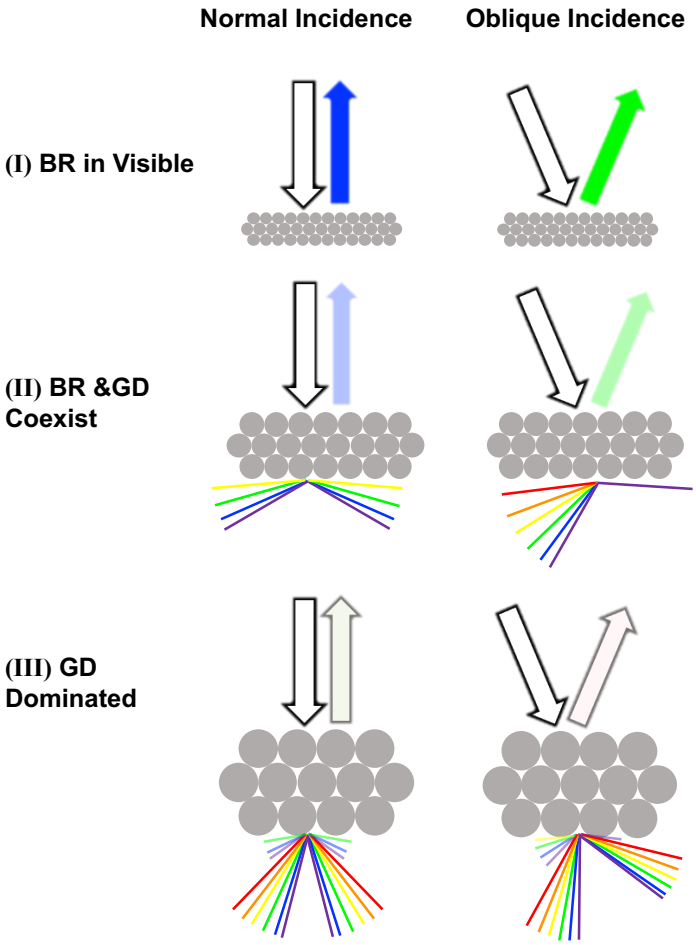


Figure 2.11: Structural color regimes for normal and oblique light incidence. In colloidal crystals, Bragg reflection (BR) and grating diffraction (GD) structural color are both angularly dependent, but with different behaviors. BR appears at specular angles, with monochromatic coloration that varies with the incident angle, while GD shifts the prismatic color band to different angles when the incident light angle is varied.

Chapter 3 Defect Structures in Colloidal Crystals and Their Effect on Grating Diffraction Structural Color

3.1 Abstract

Colloidal crystals of micron-sized colloids create prismatic structural colors through the grating diffraction of visible light. Here, we develop design rules to engineer such structural color by specifically accounting for the effect of crystal defects. The local quality and grain size of the colloidal structure is varied by performing self-assembly in the presence of a direct current (DC) electric field. The deposition, self-assembly, and crystallization of these colloids results in polycrystals of variable size, as controlled by the dissolved ion concentration (from 0.01-10 mM) and the applied electric current (from 1.6 - 310 μA/cm^2). Under these operating conditions, the global six-fold crystal bond order parameter (ψ_6) of the self-assembled crystals varies from 0.45±0.05 to 0.95±0.01 and the crystal grain number density varies between about 5 to 100 per 0.01 mm^2. We find that the grating diffraction structural color intensity of these self-assembled materials is strongly correlated with the crystal quality and grain number, with the diffraction efficiency varying by a factor of ~2.5 over the range of ψ_6 probed. Molecular dynamics (MD) simulation of the electrophoretic deposition reproduces the kinetics of the self-assembly, as well as the final structures. It also extends the number and range of deposition conditions probed, thereby creating a library that can be used to study the relationship between defect properties and grating diffraction structural color. Applying the finite-difference time-domain (FDTD) method to solve for light-material interactions in the MD-simulated structures yields calculated spectra that agree with experimental observations. The analysis also identifies a design trade-off between

diffraction intensity and azimuthal uniformity as order parameter and grain density are varied, thereby demonstrating that the grating diffraction structural color of self-assembled crystals of micron-sized colloidal spheres may be controlled by means of their local crystal quality and polycrystallinity.

This chapter was adapted from a publication[122]: T. Liu, C-M. Young, T. Moore, S. C. Glotzer, M. J. Solomon, Defect Structures in Colloidal Crystals and Their Effect on Grating Diffraction Structural Color, *ACS Appl. Mater. Interfaces* 2025, DOI: https://doi.org/10.1021/acsami.4c18558. Tianyu Liu and Michael J. Solomon conceived this research and designed the experiment. Tianyu Liu conducted the experiments with assistance from Chih-Mei Young. Chih-Mei Young and Tianyu Liu developed and conducted the image analysis of the microscope images. Chih-Mei Young conducted the MD simulation with assistance from Timothy C. Moore. The computational work utilized computational resources and services supported by Advanced Research Computing at University of Michigan.

3.2 Introduction

Structural color is an optical phenomenon that results from the constructive interference of light by micron to submicron periodic structures. This coloration is brilliant, iridescent, and reconfigurable in species such as chameleons[72,73], cephalopods[123], and squids[93]. Reconfigurability—that is, the morphing of the optical response due to structural changes in embedded periodic proteinaceous structures—allows the organism to manipulate the hue, intensity, and appearance of its skin.

Biomimetic structural color is novel and versatile and, if artificially recapitulated, could be used in pigments[23], decorative patterns, and color filters[124]. Colloidal particles are micron or submicron sized building blocks that can be self-assembled into dense and ordered structures.

Because their size is comparable with the wavelength of visible light, periodic arrays of colloidal spheres can diffract light, thereby causing color interference. Artificial structural color generated by colloidal self-assembly can serve several purposes. For example, the structural color of colloidal crystals can be applied in textiles[125], optical displays[126], anticounterfeiting codes[84], thermal management materials[127], sensors[128,129] and soft robotics[130,131]. Photonic crystals can provide functionality in microfluidic chip systems[132] or serve as on-chip label-free colorimetric sensors for specific analytes[133]. Finally, coloration due to light diffraction can be used to characterize the orientations of colloidal domains[27] and the size distribution[134] of microparticles.

The potential energy interactions between colloids — including those due to van der Waals forces, steric repulsions, and the screened Coulombic repulsion of charges on the particle surfaces — control their self-assembly into ordered structures[135]. Such colloidal crystals can be fabricated by methods that include solvent evaporation[16,17], spin coating[136,137], and the application of alternating current (AC)[42,138] or direct current (DC) electric fields[29,30,99,139]. Among these methods, the application of DC electric fields — which induces electrophoretic deposition of colloids — is a quick and versatile tool to assemble high quality colloidal 2D[140] and 3D[30] crystals. Applying a DC electric field across a conductive solution generates colloidal particle motion through several mechanisms. First, Faradaic reactions at the substrate surface produce ionic flows. These ionic flows create electric fields that generate particle electrophoresis. Second, particularly in water, these surface reactions can further generate electro-hydrodynamic flows of colloidal particles that promote self-organization on the surface[141]. The DC-field driven deposition, assembly and crystallization kinetics of colloids are well studied from the point of view of both equilibrium self-assembly and transport kinetics[19,32]. The specific operating conditions in colloidal electrophoretic deposition can produce a range of colloidal phases, such

as 2D clusters[142], ordered colloidal arrays[140,143,144], and liquid crystals of anisotropic particles[19,145]. Because of the reversibility of the applied electric fields that generate electrophoretic deposition, these self-assembled colloidal structures are reconfigurable.

By taking advantage of this reconfigurability, colloidal crystals assembled by DC electric fields have been used to produce reversible structural color[18,146]. The structural color appearance varies significantly with particle size in the range of ~0.1-1 μm because of different coloration mechanisms that range from Bragg reflection to grating diffraction[31,147,148]. Grating diffraction structural color produces a full spectrum of visible coloration propagated at different angles. This rainbow-like phenomenon has been identified in thin (1-5 layer) colloidal crystals with building block size ranging from to 0.3 μm to 1.3 μm. Colloids of this size can be directly visualized in real-time by confocal scanning laser microscopy (CLSM). Such direct visualization opens new possibilities for directly connecting colloidal crystal properties, including defect structures, to the structural color optical response[31,104].

We hypothesize that structural color produced by the grating diffraction mechanism is controlled by the quality of the colloidal crystal. There is prior evidence supporting a similar hypothesis for structural color produced by Bragg reflection of multilayer crystals. For example, by introducing differently sized particles in low quantities during solvent evaporation, *Liu et al.* showed that the colloidal crystal structure became disordered, and that the intensity of the Bragg reflectance was correspondingly reduced[149]. Moreover, even in a system of uniformly sized colloidal particles, variability in crystal quality due to the presence of defects such as grain boundaries can affect the structural color of multilayer crystals. Using simulation, *Liu et al.* studied the effect of this variability. Different types of defects, including dispersed/clustered vacancies, stacking fault tetrahedra, planar faults, and microcracks—all commonly present in

evaporatively assembled colloidal crystals—were found to affect the structural color spectral response[16]. In particular, the effect of defects on structural color reflectivity scaled with the total defect volume.

Notwithstanding these results and given that this earlier work relied on the simulation of defects, there is a lack of direct experimental characterization of defect abundance and type in self-assembled colloidal crystals and correlation of such measurements with the structural color response. We address this research gap here, by exploiting the fact that defect structures in colloidal crystals with grating diffraction structural color are directly observable by confocal laser scanning microscopy (CLSM). To accomplish this aim, we produce a state diagram of microstructures by self-assembling colloidal crystals through electrophoretic deposition under conditions of varying Debye screening length and DC electric field strength. Because the size of the colloidal particles is approximately 1 μm, the structure of these colloidal crystals can be characterized with single-particle resolution by CLSM. These crystal structures vary in hexatic order parameter and grain size, especially as the DC electric field strength is changed. We find that quantitative measures of local order and polycrystallinity are strongly correlated with the structural color optical spectrum. The deposition, self-assembly, and final structures were reproduced by molecular dynamics simulation; the optical response of these structures was calculated by finite-difference time-domain (FDTD) simulation to further investigate the correlation between crystal quality and structural color response.

3.3 Methods

3.3.1 Colloidal self-assembly by DC electric fields

The device to apply DC electric fields to an initially homogeneous colloidal suspension was built as described in *Liu et al*[31]. To perform electrophoretic deposition, indium tin oxide

(ITO) coverslips (70-100 Ω, SPI Inc.) functioning as device electrodes were sequentially ultrasonicated in water (10 min), acetone (10 min), isopropyl alcohol (10 min), and poly(sodium 4-styrenesulfonate) (PSS) in 0.5 M KCl (15 min)[99]. The purpose of the last step was to coat the ITO surface with the negatively charged 4-styrenesulfonate group.

Sulfate-stabilized fluorescent polystyrene spheres (0.95 ± 0.02 μm, Thermo Fisher Scientific, F8851, Lot 2525740) were suspended in dimethyl sulfoxide (DMSO) with an initial concentration of 0.9 vol.%. This initial volume fraction yields the deposition of three colloidal layers (each monolayer coverage requires 0.3 vol.%). Tetrabutylammonium chloride (TBAC), at concentrations varying from 0.01-10 mM, was introduced to control the Debye length and pair potential of the colloids. The conductivity of DMSO with various TBAC concentration were measured by conductivity meter (HORIBA Scientific, EC 11), as shown in **Figure 3.9**a. Approximately 9 μL of particle suspension was added into a cylindrical solution chamber of diameter 9 mm and gap height 0.12 mm. We then applied a constant electric current across the gap height of the solution using a potentiostat (Metrohm PGSTAT128N), yielding a current density i that was varied from 1.6 to 310 μA/mm^2.

The velocity u_o and Peclet number of the colloidal particles undergoing electrophoretic deposition were determined by the method described in *Ferrar et al.*[32] and *Kim et al.*[33]. The velocity u_o is determined by counting the number of particles deposited as a function of time, as reported in **Figure 3.9**b. These measurements were performed when the initial monolayer was no more than 20% filled. This filling duration varied between 10 s and 10 min, depending on the applied current density. We here describe the deposition conditions by reporting the Peclet number, $Pe = u_o d/D_o$, where u_o is the free-particle deposition velocity, d is the particle diameter, and D_o is the free-particle diffusivity. The free particle Brownian diffusivity D_o is 0.23

$\mu m^2/s$, determined by the Stokes-Einstein equation at 1 atm, 25 °C. **Figure 3.9**c lists the deposition velocities and calculated Peclet numbers at the conditions of this study.

3.3.2 Optical spectroscopy of structural color

Optical spectroscopy was performed to characterize the structural color response of the self-assembled colloidal crystals. To control the relative particle interaction and avoid chemical decomposition of the structural color, in addition to conditions described in the above section, these specimens were prepared under the same condition of c = 0.1 mM and i = 79 $\mu A/cm^2$. We controlled the fraction of particles adsorbed by varying the surface treatment of the ITO slides.

The customized device used for optical measurement is as described in *Liu et al*. Briefly, a collimated incident light source is projected onto a sample stage; a signal collector is connected to a spectrophotometer (HDX-VIS-NIR, Ocean Optics, Inc.). In this study, the detection angle was fixed at a polar angle $\theta = 30°$ relative to the angle of the source transmission (that is, $\theta = 0°$ is oriented along an axis perpendicular to the ITO electrodes). Real-time signal detection was enabled to capture the spectral variation during the assembly process. The spectrum of the final assembled structure was collected when it attained steady state.

3.3.3 Confocal laser scanning microscopy

Confocal laser scanning microscopy (Nikon A1R, 100X oil immersion objective, NA=1.40) was used to monitor the structure and kinetics of self-assembly. The shutter-flash mode was used to prevent photobleaching and photo-induced assembly[33]. Confocal images of size 512 x 512 pixels and 62 nm/pixel resolution were captured at a height of 0.5 μm above the substrate, coincident with the centroidal height of the deposited colloids. In most instances, nine adjacent images were acquired and stitched into a single 1440 x 1440 pixel (89 x 89 μm^2) image. This high resolution, wide field view of the structure facilitated the imaging and analysis of

multiple crystal grains within the specimen. We used the image analysis tool trackpy[150] to identify the centroidal location of each particle deposited on the surface of the ITO electrode. The fidelity of particle identification was 99.6% and the resolution of the identified centroids was ± 0.01 μm, as determined by variability in the centroidal locations of particles fixed to the substrate.

3.3.4 Molecular dynamics simulation

Simulations of colloidal self-assembly by electrophoretic deposition were carried out with Langevin dynamics in HOOMD-Blue (v4.4.1)[53]. Each simulation includes 8,000 particles. To model experimental conditions with various TBAC concentrations and applied electric fields, an electrostatic double layer repulsion pair potential and drag force induced by the DC electric field were adopted, as the schematic shown in **Figure 3.10**a. By tuning the parameters of the two contributions, a phase diagram corresponding with experimental results was obtained. The self-assembly kinetics, driven by electro-hydrodynamic interactions, were separately modeled using the same electrostatic double layer repulsion pair potential and an additional attractive pair potential. These two pair potentials are Z-position-dependent.

The pair potential that accounts for electrostatic double layer repulsion between colloids, V_{DL}:

$$V_{\mathrm{DL}}(r) = \frac{\mathrm{a}}{2} Z e^{-\kappa(r-(2\mathrm{a}))} \qquad 3.1$$

where a is the radius of the particles in the pair, r is the interparticle center-to-center distance. The material constant Z is proportional to the surface electric potential ζ as defined by the equation, $Z = 8.3 \times 10^{-8} tanh^2(\zeta/9.73)$ J m^{-1}at room temperature for DMSO solution[12], and ζ was measured to be -50 mV[19]. κ^{-1} is the Debye screening length, dependent on the ionic strength of the solution. κ^{-1} = 25 nm in 0.1mM TBAC/DMSO solution, as taken from *Shah et*

al[18]. V_{DL} calculated via Equation 3.1 was plotted in **Figure 3.10**b. For the other TBAC concentrations, varying from 0.01 mM to 10 mM, we approximated κ^{-1} by scaling the reference value by a factor of $1/\sqrt{c}$, where c is the TBAC concentration as per the definition of the Debye length[12]. These calculated κ values can be found in **Table 3.1**. To calculate the magnitude of the field-induced electric force on the particles, we used a model in which the electrostatic force on the particles from the DC electric field (F_E) is counterbalanced by the drag force (F_D) during the deposition process. Here, we take $F_D = 6\pi a\mu u$, where the deposition velocity (u) measured from the experiment (c.f. **Figure 3.9**b), and the particle radius a and solution viscosity μ were both set in accordance with the experiment.

To model the influence of electro-hydrodynamically induced lateral attraction between the deposited particles on the kinetics of the self-assembly process at high current density, particles in the bottom layer of the simulation box interact through a Lennard Jones (LJ) pair potential, $V_{\mathrm{LJ}}(r)$ (**Figure 3.10**). The magnitude of the attractive well (ϵ) of the LJ potential is taken as proportional to the electric field force, $\epsilon = AF_E$, where F_E is in femtonewtons (fN), as suggested by literature[142]. By matching the experimentally measured kinetics with simulation, we approximated the constant A to be 0.029 k_BT/fN. Parameters used in this simulation are shown in

Table 3.2. The interaction potential of the particles in the bulk solution above the surface was modeled solely through $V_{\mathrm{DL}}(r)$. The interaction between the particles at the bottom layer of the simulation box and the particles in the bulk was taken to be $V_{\mathrm{DL}}(r)$. The interaction between two particles—both in the bottom layer—was modeled by $V_{\mathrm{LJ}}(r)$. The schematics and potential energy diagram are shown in **Figure 3.10**a. Parameters used in the MD simulation are summarized in **Table 3.1**. In all simulations, the boundary condition of the four lateral sides of the simulation box is periodic. Upon deposition, the particles were stopped by a rigid boundary at the bottom of the simulation box. The interaction between the particles and the wall was modelled by the well-known Weeks-Chandler-Andersen (WCA) pair potential (ε = 1 k_BT)[42].

3.3.5 Hexatic Order Parameter

The local hexatic order parameter, $\psi_{6,j}$, of each particle identified in experiment or simulation was computed using the *freud* library[151]. For each located particle, $\psi_{6,j} = \frac{1}{N_j}\sum_{k=1}^{N_j} e^{i6\theta_{jk}}$ was computed for the N_j nearest neighbors, as identified within a distance specified by the first peak the of the radial distribution function $g(r)$. Here, θ_{jk} was the angle between the vector connecting sphere *j* and its neighbor *k* relative to an arbitrary reference direction[152]. $\psi_{6,j}$ is a complex number whose magnitude describes the local hexatic order and whose phase describes the hexatic orientation of the local environment around particle j. A particle for which the magnitude of $\psi_{6,j}$ is higher than 0.85 is taken as crystalline. This criterion, which was selected empirically by inspection of the order parameter distributions, was used to classify particles as crystal or defect. For each experimental or simulation condition, the overall crystal quality was determined as the average magnitude of $\psi_{6,j}$ for all N particles in the image or simulation.

3.3.6 Crystal grain analysis

Experimental and simulated structures displayed multiple crystal grains. These grains were identified by using the Density-Based Spatial Clustering of Applications with Noise (DBSCAN) clustering analysis method[151]. DBSCAN is a method that applies an algorithm that classifies samples into clusters by means of density, distance, and neighborhood parameters. DBSCAN identifies objects as sets of densely packed centroids; these objects are labeled as clusters. Here, the hexatic orientation and the position of each particle were taken as input features of this algorithm to label and number the clusters; therefore, each cluster is associated with a crystal grain. The minimum number of particles in one grain (MinPts) was set to five. The method's other adjustable parameter ξ defines the criteria by which centroids are clustered. We

calculated the average distance between each point, a three-dimensional coordinate that incorporates both positions and hexatic orientation of a particle, and its k neighbors (where k = MinPts). By plotting these average k-distances as a function of number of points, we identify the point of maximum curvature on the resulting elbow plot and set the corresponding average k-distances as $\xi = 0.2$ [153]. By applying this algorithm, the particles located closely in position and hexatic orientation are labelled as within the same clustered crystal grain. The grain number density (n_g) is calculated as the number of clusters counted (N_g) from one image divided by the area of the image or simulation snapshot. In the experiments, grains that share a boundary with an image edge are counted as half-grains to compensate for edge effects.

3.3.7 Finite difference time domain (FDTD) simulation of optical spectra

We simulated structural color optical spectra by means of the FDTD method[16,154,155], as implemented in Ansys Lumerical 2022 R2.4. The FDTD method solves the set of Maxwell equations within a defined volume through a discretization approach. FDTD structure obtained from experiment or MD simulation was used as input for the simulation. In the simulation, a plane wave light source of wavelength varying between 400 nm – 900 nm was perpendicularly propagated toward the crystal x-y plane. The light intensity was determined from the far-field electromagnetic field magnitude that propagated to different angles. The diffraction intensity was computed at one specific polar angle, θ = 30° and at various azimuthal angles, ϕ = 0-360°. The diffraction spectrum at θ = 30° was calculated by averaging the intensity over all azimuthal angles, as described in *Liu et al*[31]. The azimuthal uniformity of the color diffraction intensity is $U_\phi = \left(1 - \frac{\sigma_{I(\phi)}}{\bar{I}(\phi)}\right) \times 100\%$, calculated based on the coefficient of variation method[156], where

$\bar{I}(\phi)$ and $\sigma_{I(\phi)}$ are the mean and standard deviation of the diffracted light intensity across all azimuthal angles (ϕ = 0-360°) at the polar angle of measurement (θ = 30°).

3.4 Results

3.4.1 Setup of real-time structural and optical measurement

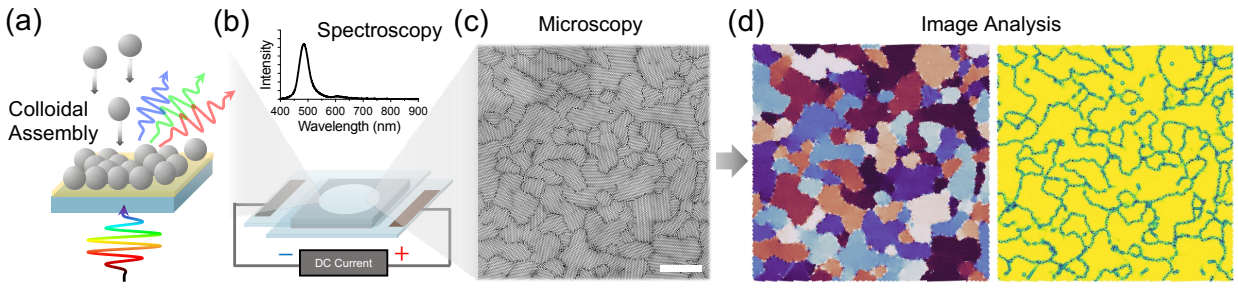


Figure 3.1: Crystal property characterization by spectroscopy and microscopy. (a) Schematic of the electrophoretic deposition in the DC electric field device. (b) Measurement of prismatic structural color by spectroscopy. (c) Wide field, high resolution CLSM image of the colloidal crystal acquired by image stitching. (d) Analysis of the CLSM image identifies crystal grain orientation, grain boundaries, and the local hexatic order parameter. Here, the color coding in the left panel identifies individual crystal grains. In the right panel, regions in yellow have high hexatic order parameter characteristic of high crystal ordering; other regions have low hexatic order parameter, and follow grain boundaries. Scale bar: 20 μm.

Figure 3.1 shows results upon applying an electric field of constant current density (i = 31 μA/cm^2) to an initially homogeneous solution of colloidal particles with c = 0.1 mM (**Figure 3.1**a). The resulting electrophoresis drives the negatively charged particles to deposit onto the anode. During deposition, the optical spectrum of the structural color was measured (**Figure 3.1**b) and the microstructure of the self-assembled particle arrays was imaged by CLSM (**Figure 3.1**c). A strong peak in the spectra is centered at 490 nm; the corresponding structure is a colloidal crystal with a distribution of grain boundaries. Image analysis characterizes the local hexatic order parameter, the polycrystalline structure, and the grain boundaries as shown in **Figure 3.1**d.

3.4.2 Electrophoretic deposition kinetics at various operating conditions

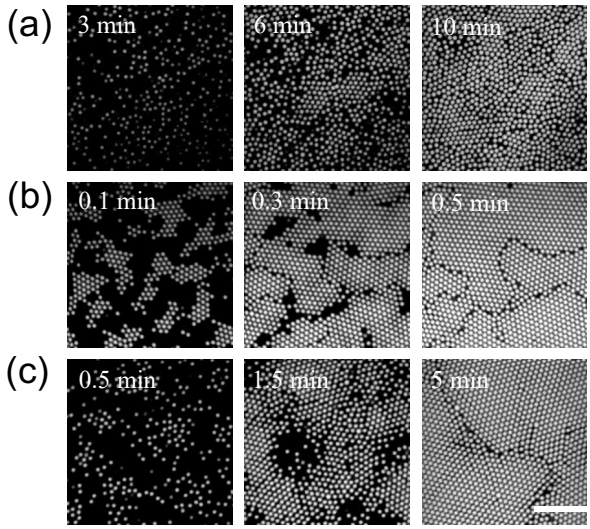


Figure 3.2: CLSM images display the electrophoretic deposition, self-assembly and crystallization kinetics at various experimental conditions. Images were captured at the surface of ITO electrode. (a) c = 10 mM and i = 31 μA/cm^2, (b) c = 0.1 mM and i = 31 μA/cm^2, and (c) c = 0.1 mM and i = 3.1 μA/cm^2. Scale bar: 10 μm.

Figure 3.2 reports the kinetics of the electrophoretic deposition as measured by experiment and simulation. Colloids deposited in a few seconds to a few minutes, depending on the ion concentration and current density. For c = 10 mM and i = 31 μA/cm^2 (Fig 2a), particles sedimented and formed the first condensed layer within about 10 minutes. As characterized by cluster analysis in **Figure 3.11**, the first crystalline clusters appeared ~6 min after deposition was initiated. The number of clusters increased with time and reached about 10 clusters per captured image at steady state (after ~10 min). The structure displays low crystallinity at this operating condition.

The kinetics of the self-assembly are sensitive to the electrodeposition conditions. For example, the deposition and self-assembly behavior before the formation of the close-packed layer is different than in **Figure 3.2**a, the assembly for c = 0.1 mM and i = 31 μA/cm^2 solution showed a well-organized, close-packed hexagonal crystal structure (**Figure 3.2**). The time evolution of the number of crystallites shows (**Figure 3.11**b) that the particles initially self-organize into multiple small crystallites. Their number increases rapidly in the first ten seconds.

It then decreases and reaches a steady value at about one-half of the peak value. The crystal structure appears to evolve by two mechanisms. First, newly deposited particles accrete to the crystallite boundaries. Growing crystallites also interact, align, and combine with neighbors to form larger crystallites. These mechanisms are active because both particles and clusters are free to diffuse on the substrate.

The experiment at c = 0.1 mM, i = 3.1 μA/cm^2 (**Figure 3.2**c) yields somewhat different self-assembly kinetics. Under this decreased applied current density, the electrophoresis deposition velocity is less; particles are still in the fluid state at t = 0.5 min. Crystallization occurred later, when a higher packing on the substrate is reached. The outcome is a crystal with less grains and a larger average crystallite size. The cluster analysis reported in **Figure 3.11**c shows that the crystal formation follows a pattern like that reported in **Figure 3.11**b; however, there are fewer. The difference in crystallite properties is evidently linked to differences in deposition conditions. At this condition, the particle deposition rate is lower than the other conditions, but the surface diffusion rate is the same. We will return to the reason these deposition conditions create variability in crystallite size in the paper's discussion.

3.4.3 Structural color and spectral during crystallization

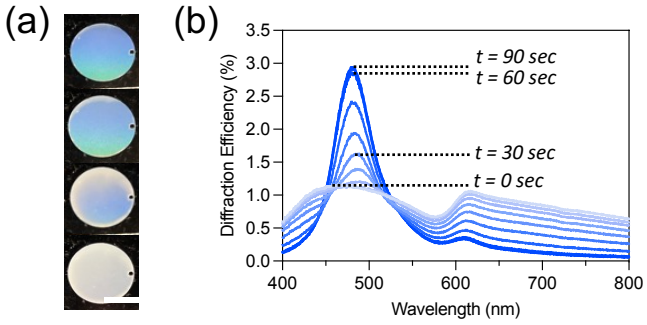


Figure 3.3: Time evolution of grating diffraction structural color. (a) Image time-series of the evolution of structural color in the self-assembled crystals at time 0, 30, 60, and 90s; the diffraction angle of observation is 30° from the axis of transmission of the source. (b) Time-evolution of the measured optical spectrum at 0, 30, 60 and 90s from the bottom to the top. The measurement conditions are c = 0.1 mM and i = 31 μA/cm^2.

The growing crystal arrays observed in **Figure 3.2** generate prismatic structural color, as shown in the images of **Figure 3.3**a. Here the conditions of electrophoretic deposition are c = 0.1 mM and i = 31 μA/cm^2 and the images are of the self-assembly chamber. Visible light incident perpendicular to the sample plane yields the iridescent structural color. The optical spectrum reported in **Figure 3.3**b confirms blue coloration, here observed at θ = 30° relative to the transmitted beam. Specifically, a peak in the optical spectrum appears at approximately 480 nm when the applied voltage is first applied. The peak continues to grow with time and reaches a steady state intensity, here measured as a diffraction efficiency of ~3.0% after 60 sec of deposition. Due to the constructive and destructive interference of light with the periodic structure, the intensity at other wavelengths simultaneously decreases.

3.4.4 Structural and optical reversibility

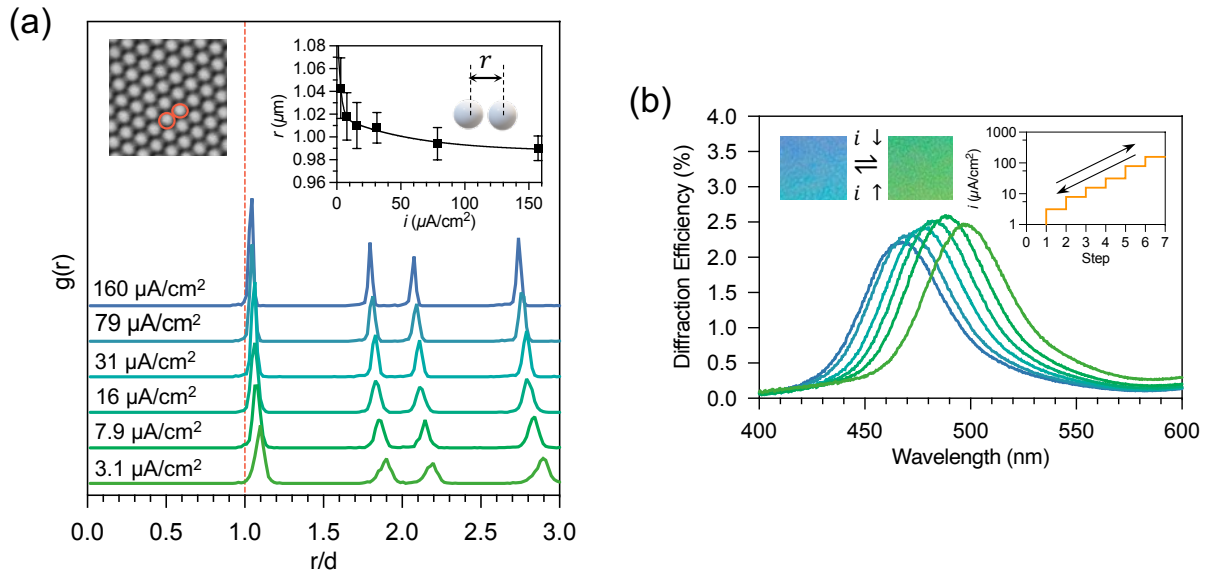


Figure 3.4: Tunability of the interparticle spacing and grating diffraction structural color. (a) Radial distribution functions, g(r), of colloidal crystals self-assembled at c = 0.1 mM and current density varying from i = 3.1 to 160 μA/cm^2. Data are vertically offset for clarity. Inset figure shows the measured interparticle distance, as defined by the schematic, at the different current densities. (b) Corresponding structural color spectra for the same conditions, also for conditions varying (a) from 3.1 to 160 μA/cm^2. The spectral maximum shifts from green to blue as i increases. The left and right insets are camera-captured images of structural color at the highest and lowest i, respectively. The insets figure shows how i is applied stepwise to probe each condition.

The lattice spacing of the hexagonal crystal can be controlled by the strength of the electric field, as exhibited in **Figure 3.4**. In this experiment, a colloidal crystal was initially assembled at i = 3.1 μA/cm^2. The current density was then increased stepwise through a sequence of magnitudes until i = 160 μA/cm^2. A steady-state signal was reached at each step. The microstructure was imaged at each condition, and the radial distribution function g(r) computed from image analysis. As plotted in **Figure 3.4**a, when the current density increases, the first peak of g(r) becomes sharper and shifts to a lower r/d, closer to the orange dash line labelled at r/d = 1.0. These data show that the interparticle distance, which controls the lattice spacing, decreases as i becomes stronger; it changes from approximately 1.05 μm to 0.99 μm over the range of current densities studied, as reported in **Figure 3.4**a inset. Accompanying peak sharpening, observable in the g(r) measurements, indicates that particles are increasingly registered with the hexagonal lattice, consistent with the structure approaching the close-packed condition.

Figure 3.4b shows the changes in the optical spectrum as i is increased stepwise as in **Figure 3.4**a. (from 3.1 μA/cm^2 to 160 μA/cm^2). The spectral peak progressively shifts from 500 nm (green) to 468 nm (blue). This change is qualitatively consistent with the shift in interparticle distance reported in **Figure 3.4**a and shows that the hue of the structural color is controlled by the current density, as also shown by the camera images (**Figure 3.4**b) of the solution chamber. This shift is consistent with the prismatic effect of grating diffraction[31], which is described by the equation,

$$m\lambda = D \sin\theta \qquad 3.2$$

where m is the order of diffraction (here, m = 1), λ is the diffracted light wavelength, and D is the grating periodicity, which is equal to $\frac{\sqrt{3}}{2}r$ for a hexagonal lattice. Here r is the interparticle

spacing, as available from **Figure 3.4**a. The spectral shift of **Figure 3.4**b is well predicted by Equation 3.2. For example, the calculated peak wavelengths are 495 ± 32 nm at i = 3.1 μA/cm^2, and 471± 21 nm at i = 160 μA/cm^2; these compare well with the measurements of 500 nm and 468 nm, respectively. In addition, the intensity of the observed structural color response (~3%) is comparable to the earlier report of *Liu et al*.[31]

Equation 3.2 consequently connects the spectral shift due to current density to an accompanying change in interparticle spacing of the crystal lattice. We believe that the lattice spacing itself decreases with current density for two reasons. First, increased current density increases the convective force of deposition[32]. The added force drives an increase in the packing at the substrate, decreasing the interlayer spacing. Second, increased current density increases the effective attraction between particles in the surface layer. This effective attraction arises due to electrohydrodynamic effects that grow with the electric field strength[30]. These current density effects on deposition are fully reversible over many cycles, as demonstrated in **Figure 3.12**. As the current density is ramped between high and low values, the structure cycles back to the same crystal state. Cyclic voltammetry shows that the Faradaic reactions driving the deposition are also robust to multiple cycles of reconfiguration.

3.4.5 State diagram of DC electric field assembled spheres

Figure 3.5 reports the state diagram of microstructures as the operating parameters of salt concentration and current density were varied between c = 0.01-10 mM and i = 1.6-310 μA/cm^2, respectively. CLSM images were acquired at steady-state. The time to reach steady-state varied between 2-10 min, depending on the deposition conditions.

Low current density – shown as the blue region in the figure – generates neither sufficient deposition force nor lateral attraction to deposit and self-assemble the particles into crystalline

structures. Considering the specific case of condition (i) shown in **Figure 3.5**b, the particles do not form a complete monolayer. The particles move freely, and the layer remains disordered. In this region, the surface coverage remains below the condition for hexagonal order.

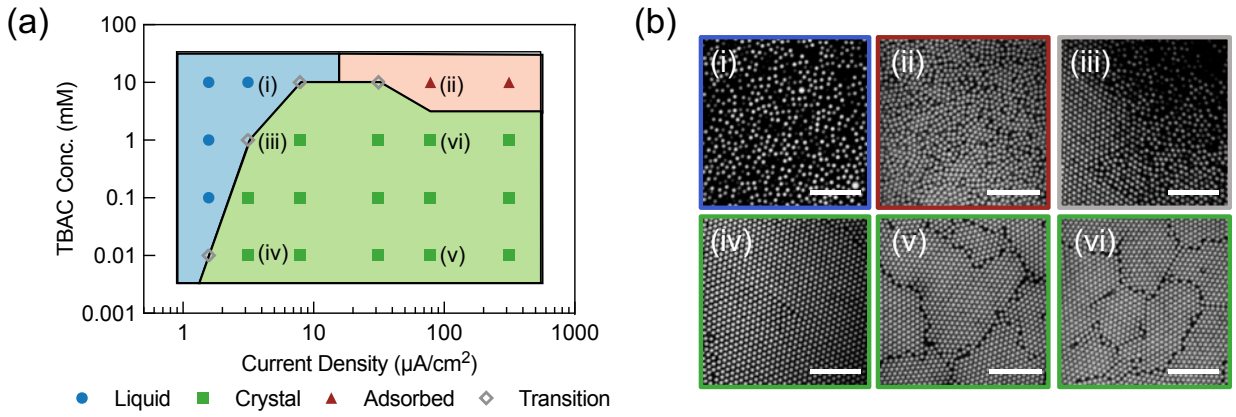


Figure 3.5: State diagram of DC electric field assembled colloids. (a) Electrophoretic state diagram for operating conditions varying from c = 0.01 to 10 mM and i = 1.6 to 310 μA/cm^2. Regimes labeled with blue, green, and red are dense liquid, polycrystal, and adsorbed state, respectively. (b) CLSM images of the microstructures resulting from various operating conditions. Corresponding experimental conditions are labeled in panel (a). Scale bar is 10 μm.

Upon increasing i or decreasing c, the deposition yields coexisting regions of disorder and hexagonal order. As shown, for example, at condition (iii) shown in **Figure 3.5**b, an interface between ordered and disordered regions was found. At these conditions, the electric field is not strong enough to create fully crystallized regions. Upon further increase in i or decrease in c, compact structures as shown in conditions (iv) and (vi) were produced. In this region (labeled as green in **Figure 3.5**a), polycrystals fully cover the substrate; the number density of crystal grains varies in this region. By changing the salt concentration and current density as per the conditions of points (iv), (v), and (vi), the number of crystal grains in the imaged area varies from one to about six.

For c > 2 mM and i > 20 μA/cm^2 an additional region of the state diagram was detected. This region, which we label the adsorbed state, is shown as red in **Figure 3.5**a. Condition (ii) shows that particles in this region are closely packed, but also with abundant defects and

disorder. Particles with crystalline order are in the minority, and crystallites are at best of very small size. Unlike the crystal and disordered liquid regions of the state diagram, the surface particles in this region of the state diagram are irreversibly bound to the substrate, indicating a strong attraction between colloidal particles and the conductive ITO film (c.f. **Figure 3.13** for evidence of binding).

The location of the boundary between the liquid and crystal phases is linked to the effects of salt and current density on the electrophoretic deposition. Previous studies have shown that if the electric field is strong, then the force it applies to the particles causes an increase in their concentration at the substrate. The particle concentration grows until the osmotic pressure it generates balances the force generated by the electrophoretic deposition. The relative strength of the electrophoretic deposition and the countervailing osmotic pressure is determined by the Peclet number. Empirically, crystallization has been observed when Pe = 1 or greater[19,32]. **Figure 3.9**c shows that in this system Pe increases with increasing current density and decreasing salt concentration, and that the liquid-crystal boundary in **Figure 3.5**a approximately tracks the boundary of Pe ~ 1 in **Figure 3.9**c.

3.4.6 Crystal quality and grain property characterization of structures in state diagram

The crystal structures imaged at the different operating conditions were further characterized by measuring $\psi_{6,j}$ of each particle and identifying crystalline clusters based on cluster analysis, as described in the methods. Each CLSM image has a size of 89 x 89 μm^2 and includes between 7500 to 9000 identified particles.

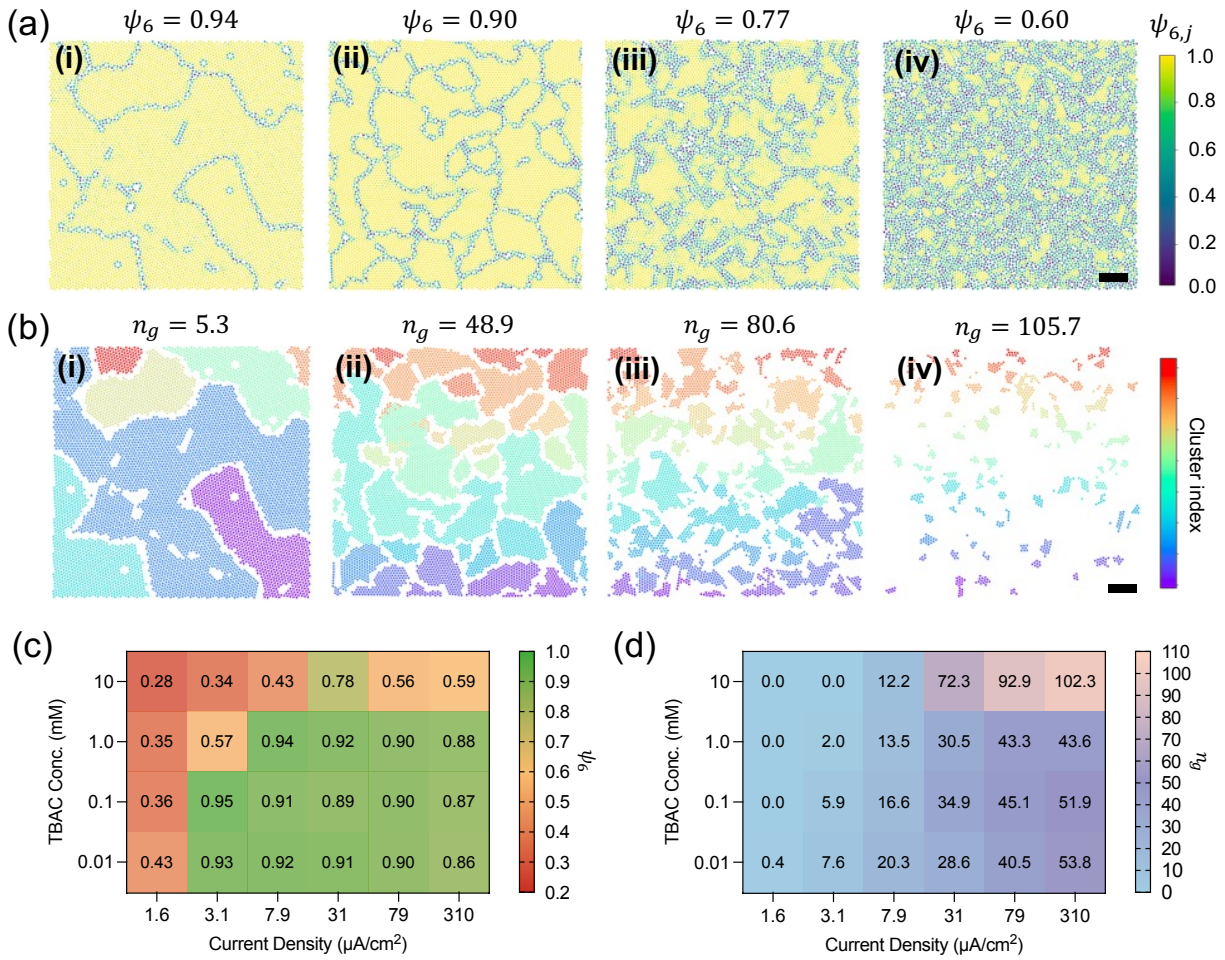


Figure 3.6: Crystal quality and grain boundary analysis of self-assembled structures. (i) c = 0.1 mM, i = 3.1 μA/cm^2, (ii) c = 0.1 mM, i = 79 μA/cm^2, (iii) c = 10 mM, i = 7.9 μA/cm^2, and (iv) c = 10 mM, i = 310 μA/cm^2. (a) Images show particle positions derived from image analysis and are color-coded by individual $\psi_{6,j}$ values. The globally averaged hexatic order parameter ψ_6 is also shown above each image. Scale bar: 10 μm. (b) Images show crystal grains identified by image analysis; they are color-coded by their Y coordinates. The number density of crystal grains (n_g) per 0.01 mm^2 is provided. Scale bar: 10 μm. (c) ψ_6 and (d) n_g measured at the studied operating conditions with ranges of c = 0.01 to 10 mM and i = 1.6 to 310 μA/cm^2. Plots in pannel (a)-(b) were created by Chih-Mei Young.

In **Figure 3.6**a and b, case (i) shows overall high crystal quality with $\psi_6 = 0.95$, where the notation ψ_6 denotes the average across all particles in the image. In this case, there are only a small number of grains and low appearance of defects. Generally, higher current density reduces ψ_6, because, as shown in **Figure 3.6**a-b (ii), more grain boundaries and crystal grains are found. At these conditions, most non-crystalline particles (dark colored) are located at grain boundaries; a minority are present in dislocations and vacancies inside of a crystal grain. These defect types

are further discussed in **Figure 3.14**. **Figure 3.6**a-b (iii) and (iv) are captured at c = 10 mM and higher i. Here the grain boundaries include more disordered particles, which further reduce ψ_6. The reduction of crystal quality coincides with a greater number of smaller size crystal grains. **Figure 3.6**c shows ψ_6 at the operating conditions studied. By comparing with **Figure 3.5**a, we see that lower ψ_6 values are associated with the liquid and adsorbed states, while crystals have a higher value, typically in the range $\psi_6 \sim 0.86 - 0.95$ (this is the region labeled in green on the table). The operating condition of c = 0.1 mM, i = 3.1 μA/cm^2 yields the highest quality crystal, as measured by ψ_6, with ψ_6 = 0.95.

The number density of crystal grains, n_g, is reported in **Figure 3.6**d. In the crystal region, n_g increases with increasing i, but has less dependence on c, suggesting that current density has a more significant effect on the polycrystalline structure than this range of salt concentrations. However, a sharp effect of salt concentration was found when c was increased above 1 mM. At this salt concentration colloids begin to adsorb to the surface, yielding low ψ_6, abundant grain boundaries, disordered regions, and small crystal grain size.

3.4.7 MD simulation of the self-assembly process

Simulation of the electrophoretic deposition shows the effect of salt concentration and current density on the local crystal quality and number density of crystal grains. **Figure 3.7**a illustrates the deposition of particles in the simulation box. **Figure 3.7**b and c report the microstructure of the surface layer. The simulations were conducted under conditions of deposition velocity and salt equivalent to those in **Figure 3.2**. The simulation conditions can be found in **Table 3.1** and

Table 3.2. At the conditions of **Figure 3.7**b, the particles form crystallites shortly after contact with the substrate. This observation is consistent with the driving force for deposition generated by the electric field and the lateral attractions due to the induced electrohydrodynamic flow. We observed slow translational and rotational movement of crystallites after their creation,

which resulted in the formation of small, fragmented crystal grains, consistent with the experimental observations reported in **Figure 3.2**b.

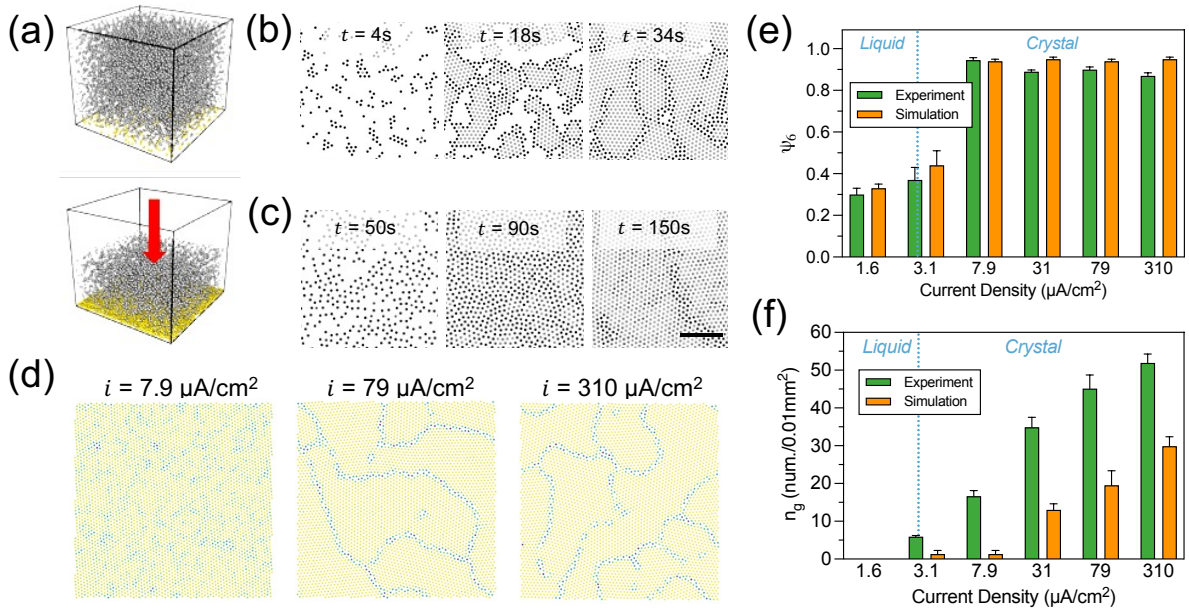


Figure 3.7: MD simulation results of the deposition and assembly process. (a) Schematic of the deposition simulation box; red labels particles that have reached the bottom substrate. (b)-(c) Snapshots of structures from MD simulations at conditions that correspond to the conditions of Figure 3.2 case (b) and (c), respectively. (d) Substrate layer of the self-assembled structures at c = 0.1 mM and various i in μA/cm^2, as simulated by MD. (e) Comparison between experiment and simulation for i = 1.6 to 310 μA/cm^2 for globally averaged hexatic order paramter, ψ_6. (f) Comparison between experiment and simulation for i = 1.6 to 310 μA/cm^2 for number density of crystal grains, n_g. Liquid and crystal regions are identified and labeled. Plots in pannel (a)-(d) were created by Chih-Mei Young.

At the conditions of **Figure 3.7**c, the deposited particles are initially disordered and do not form multiple crystalline domains. Yet, the particles ultimately self-assemble into a crystal with a larger grain size and fewer grain boundaries. In both cases, the morphological development of the crystal grains in simulation closely resembles the experimental observations.

Figure 3.7d shows the hexatic order parameter, $\psi_{6,j}$ of particles in the substrate layer at c = 0.1 mM and various i, again as simulated by molecular dynamics. As the current density is increased, the number of crystal grains increases, there are more defects, and the crystal grain size is smaller. This trend of ψ_6 and n_g with i is reported in **Figure 3.7**e and **Figure 3.7**f, respectively. The corresponding experimental results are also reported.

At current density equal to 1.6 and 3.1 μA/cm^2 a disordered phase is produced. The average ψ_6 at these conditions varies between 0.3 and 0.6. When i = 7.9 μA/cm^2, the average ψ_6 increases to 0.94. Greater current density thus produces structures of higher ψ_6. As current density increases, the number density of crystals also increases (**Figure 3.7**e). At the highest current density under simulated, n_g = 30 per 0.01 mm^2.

Figure 3.7e and **Figure 3.7**f show fair agreement between experiment and simulation. In **Figure 3.7**e, ψ_6 is slightly higher for the simulations than the experiment; however, for crystals, the difference is not statistically significant in any case (p = 0.26). In **Figure 3.7**f, while the number density of grains increases monotonically in both the experiment and simulation, the simulations do yield a lower grain density than the experiments. The difference is statistically significant in all cases (p = 0.99). An expanded set of MD simulated structures are reported in **Figure 3.15**, including much higher (up to ~2000 μA/cm^2) current density and at various salt concentration.

The overall consistency between experiment and simulation builds a comprehensive understanding of DC electric field deposition and the self-assembly process. Qualitatively, both methods confirm that increasing current density results in lower ψ_6 and higher n_g. Quantitatively, there is good agreement for the crystal quality (**Figure 3.7**e); however, the simulated grain density (**Figure 3.7**f) is significantly less than observed in the experiments. There are several possible reasons for the observed difference between the grain number density of simulation and experiment, as reported in **Figure 3.7**f. First, the simulations do not include an interaction between the particles and substrate beyond the standard repulsion modeled by the WCA potential. The presence of an attractive component of the substrate-particle interaction could subtlety affect the surface diffusion of the colloids, thereby affecting the grain boundary

size. Second, the effective attraction that models the electroosmotic flow (c.f. **Figure 3.10**) is an approximation[142]. Its details could also affect the complex particle dynamics that determine the grain boundary number density and size. Despite these discrepancies, the simulation results demonstrate that the electro-hydrodynamic interaction plays an important role in colloidal self-assembly kinetics and affects the outcoming crystal quality.

3.4.8 Trade-off between structural color intensity and uniformity at various defect abundance

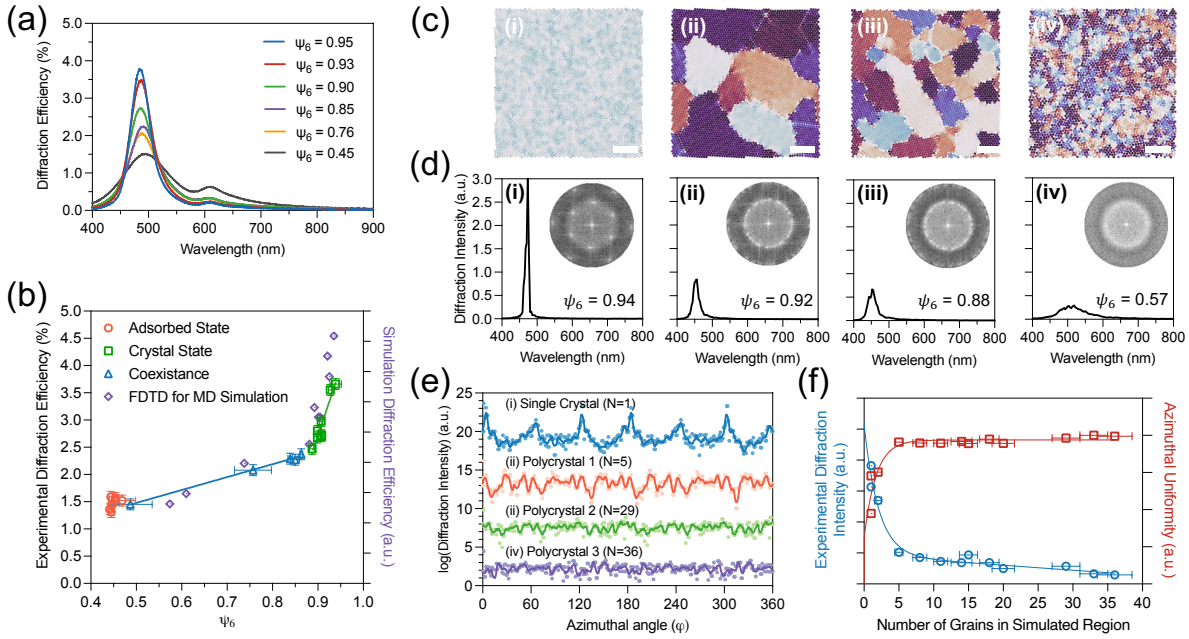


Figure 3.8: Correlation between defect abundance and structural color properties. (a) Measured structural color spectrum for different ψ_6 corresponding to different positions on the state diagram. (b) Structural color peak intensity in different electrophoretic states and ψ_6 values; including experimentally measured diffraction efficiency (left-axis) and FDTD simulated far-field diffraction efficiency (right-axis). The left-hand scale corresponds to the ○ , □, and △ symbols; the right-hand scale corresponds to the ◇ symbols. (c) Crystal-grain structure (substrate layer) of the MD simulated crystal. The simulated structures vary in crystal quality and cluster number; the left-hand panel reports a single grain of high crystal quality. Scale bar: 10 μm. (d) Structural color spectrum calculated by the FDTD method (for polar angle $\theta = 30°$) for the MD simulated structures of panel (c). The inset figure in each panel shows the diffraction pattern by far-field projection calculated by FDTD, also labeled by the ψ_6 values. (e) Simulated structural color spectrum by calculating the diffraction intensity at $\theta = 30°$ for different azimuthal angles for the four cases in panel (c) and (d). (f) The average structural color intensity and azimuthal uniformity as a function of the number of grains in the simulated region. Structure in panel (c) is created by Chih-Mei Young.

The set of crystals produced at the different conditions of the **Figure 3.5** state diagram may be ranked by their crystal quality. **Figure 3.8**a reports the structural color diffraction of

these materials, indexed by each specimen's ψ_6. The spectra each exhibit a peak; this value shifts slightly (from 495 to 485 nm) as ψ_6 varies from 0.45 to 0.95. In addition, the diffraction efficiency varies considerably with ψ_6. Although a disordered packing (ψ_6 = 0.45) still exhibits a color peak, the peak diffraction efficiency increases by a factor of 2.4 as ψ_6 increases from 0.45 to 0.95. The diffraction from the disordered specimen is consistent with other reports that compact packings with disordered structure display structural color[157]. At the same time, polycrystals with high quality or ψ_6 have a sharper and higher diffraction peak. A similar set of spectral curves can be obtained for the simulated structures by inputing the coordinate files generated by the simulations into an FDTD calculation of the far-field scattering.

Figure 3.8b plots the peak spectral intensity for all conditions, experiment and simulation. At low values of the hexatic order parameter, the diffraction efficiency increases slowly (indicated by the green line) with ψ_6. This slow increase continues until ψ_6 reaches ~ 0.87. The structural color intensifies rapidly with further increase in ψ_6. The rate of change in diffraction intensity in this region is about 10 times the rate of change in the low hexatic order parameter region. The turning point between the two regimes in the rate of change is at ψ_6 ~ 0.87. The maximum diffraction efficiency measured in the experiments is approximately 4.0%. Lower ψ_6 values are correlated with more grain boundaries. This means crystals with fewer grain boundaries can significantly improve the color intensity. FDTD calculations of the simulated structures corroborate the experiments and more completely describe the trend of **Figure 3.8**b. In addition, the slight polydispersity of the particles used in the experiments has negligible effect on these results. Specifically, incorporating the manufacturer polydispersity into the FDTD simulation does not change the spectral shape; the peak diffraction intensity changes by no more than 10%.

Figure 3.8c and **Figure 3.8**d report the microstructure and optical spectra of four of these simulated cases. Interestingly, comparing cases (i) and (ii), the structural color diffraction of a single grain crystal is about four times greater than a polycrystal with a similar value of ψ_6. This result indicates that the number density of grains (n_g) in the crystal is a second variable impacting grating diffraction structural color. Thus, the diffraction intensity is a function of not only the local crystal quality (as characterized, e.g., by ψ_6), but also how defects are organized in the material (as characterized e.g., by the grain density n_g).

In addition, the diffraction patterns of the simulated structures show variability in the azimuthal plane, as apparent in the insets of **Figure 3.8**d. The single crystal (case (i)) displays a clear 6-fold pattern in the azimuthal plane. The more polycrystalline structure of case (ii) shows a more uniform azimuthal scattering pattern; however, multiple bright points, corresponding to the scattering of individual grains, are still apparent. Case (iii) and (iv) in **Figure 3.8**d further illustrate the trend; these structures have higher n_g and even more uniform azimuthal uniformity. The intensity distribution as a function of azimuthal angle is shown quantitatively for the four cases in **Figure 3.8**e. Thus, interestingly, azimuthal uniformity of the structural color response of these materials – which is important for applications – requires some level of polycrystallinity.

This trade-off between color intensity and azimuthal uniformity is comprehensively illustrated in **Figure 3.8**f. **Figure 3.8**f reports the diffraction intensity as a measure of color intensity and coefficient of variance as a measure of azimuthal uniformity. As the number of crystal grains in the simulated area increases from one to five, there is a drastic increase in uniformity, but with the consequence of a weaker diffraction intensity. The diffraction intensity continues to decline as the number of grains increases beyond five; however, the color

uniformity undergoes no further significant change. Note that the azimuthal intensity distribution depends on the absolute number of grains in a field of observation.

Figure 3.8 therefore links the diffraction optical properties of colloidal crystals with their microstructural properties. We found a correlation between the hexatic order parameter and grain number density with the structural color properties of spectral intensity and azimuthal uniformity. Although creating a more perfect crystal increases the spectral intensity of the structural color, the requirement of fewer crystal grains for a perfect crystal reduces the color uniformity. Characterizing this tradeoff, as apparent in **Figure 3.8**f, is particularly useful for engineering applications, because they require attention to both color intensity and uniformity.

3.5 Discussion

This work demonstrates the effect of applied current density and solution salt concentration on the self-assembly, crystal quality, and diffraction grating structural color of colloidal crystals. We established the effect of defects, as quantified by the hexatic order parameter and grain number density, on the spectral intensity and color uniformity of the structural color produced by the controlled self-assembly of colloids. In this discussion, we address the marginal effect of additional defects on the color quality of the colloidal crystal structural color. We compared this marginal effect, here identified for the case of grating diffraction structural color, with prior work that addressed similar effects in multiple layered colloidal crystals. Finally, we reviewed prospects for applications of these findings to produce structural color materials.

In addition to the identification of the operating conditions that control crystal quality and grain size of colloidal crystals, this study identified that there is a tradeoff between the color intensity and color uniformity of these materials. This tradeoff is captured in **Figure 3.8**f; it

shows, through FDTD calculations for MD simulated structures, that crystals with low grain density exhibit non-uniform grating diffraction. In the limit of a single crystal, the azimuthal diffraction intensity shows six-fold symmetry. Approximately 5-10 grains are needed to ensure that the orientation of the crystallites is sufficiently random to yield uniform azimuthal color intensity. This also indicates that larger grain size can improve the color intensity but reduce the uniformity, as shown by **Figure 3.17**. Therefore, counterintuitively, applications requiring color uniformity would be better achieved with a polycrystalline, rather than single-crystal structure. Yet, there is a design tradeoff, because **Figure 3.8**f also shows that the introduction of polycrystallinity reduces the color intensity. In the present case, a 4%-2.5% decrease in color intensity accompanies the level of polycrystallinity that achieves color uniformity.

A chief finding of this study is the characterization of the marginal effect of additional defects on the grating diffraction optical response of colloidal crystals. The defects of the self-assembled crystals are primarily grain boundaries (c.f. **Figure 3.14**). This study demonstrated the profound effect of defect abundance on structural color intensity (**Figure 3.8**b), as shown by the sensitivity of the diffraction efficiency to the hexatic order parameter, ψ_6. The point is equally apparent when these data are plotted as a function of the fraction of defect particles, as illustrated in **Figure 3.16**. The key point is that the first defects introduced into a perfect crystal have a much stronger marginal effect on the color intensity than additional defects added on top of them. That is, introduction of 1% defect particles into a high-quality crystal ($\psi_6 > 0.87$) marginally reduces the diffraction intensity by 0.1%; however, introducing the same percentage of defect particles into an already defect colloidal crystal (here taken as $\psi_6 \leq 0.87$, less than the turning point in **Figure 3.8**b) reduces the diffraction intensity by only 0.01%.

This transition from a crystal whose color intensity is highly sensitive to defects to one that is more insensitive occurs at a defect abundance of about 25% (**Figure 3.16**b). Moreover, in **Figure 3.16**c, we show the special distribution of defect at different defect abundance. We hypothesize that this difference in sensitivity to defects is related to the collective nature of the light-material interaction that leads to structural color. Specifically, the introduction of one defect into an otherwise perfect crystal strongly reduces the diffraction intensity because the light-matter resonance that generates the diffraction grating is compromised by the effect. This resonant effect is non-local, extending well beyond the volume of the defect itself. This regime of strong effect continues while the defect concentration is dilute; in this regime each additional defect contributes a strong effect as it non-locally perturbs the light-matter resonance. However, as the defect abundance increases into the non-dilute regime, the non-local perturbation generated by the defects begin to spatially overlap. The incremental effect of each additional defect is consequently less. This hypothesis could be tested in future work by introducing defects at specific points in the crystals. At low concentrations, correlated distributions of defects would have different effects on the color intensity than uniformly distributed defects.

Interestingly, this finding is consistent with earlier work that characterized the effect of defects on the Bragg reflectance of multilayer colloidal crystals[16]. The Bragg reflectance of those crystals, produced by evaporative self-assembly, was highly degraded if the defect volume was less than about 10%; if the defect volumes were greater than 10%, the effect on the Bragg reflectance was less considerable.

The factors here identified influencing the formation, structure, and optical response of colloidal crystals can support the future development of new materials with tailored optical properties. For example, identifying the role of spatial correlations of defects in the intensity of

the grating diffraction optical response offers the possibility of using this feature as a design parameter in materials development. Such defect engineering could be usefully integrated with the reconfigurability of the electrophoretic self-assembly method (c.f. **Figure 3.12**) to vary the self-organization of defects in time. In addition, the work indicates that the azimuthal uniformity of the grating diffraction response is directly linked to the size and orientation of crystal grains. This structure-property relationship could also be exploited for materials design. This approach expands the potential for future studies on the optical response of colloidal crystals, including understand effects of defects introduced through irregular particle sizes or broader particle size distributions. Taken together, these findings extend the scope for microstructural engineering of grating diffraction structural color, the pursuit of which could be fruitfully applied to the advanced manufacturing of materials and devices such as sustainable coatings and electrophoretic displays.

3.6 Conclusions

In summary, by varying the salt concentration and applied current density during electrophoretic deposition, we engineered crystal quality and grain number density in thin colloidal crystals so as to control the intensity and azimuthal uniformity of the grating diffraction structural color response. Molecular dynamics and FDTD simulations revealed the direct connection between the hexatic order parameter of the crystal and the spectral intensity of the structural color; it furthermore showed that the degree of polycrystallinity affects both the spectral intensity and color uniformity of the colloidal crystal materials. The study shows that electrophoretic deposition is an attractive means to create colloidal crystal arrays with tunable and reconfigurable structural color for applications exploiting the prismatic color generated by grating diffraction. The polycrystalline structure can be fabricated and controlled by means of

assembly operations, thereby enabling versatile performance of the azimuthal intensity of the structural color response.

3.7 Supplementary Information

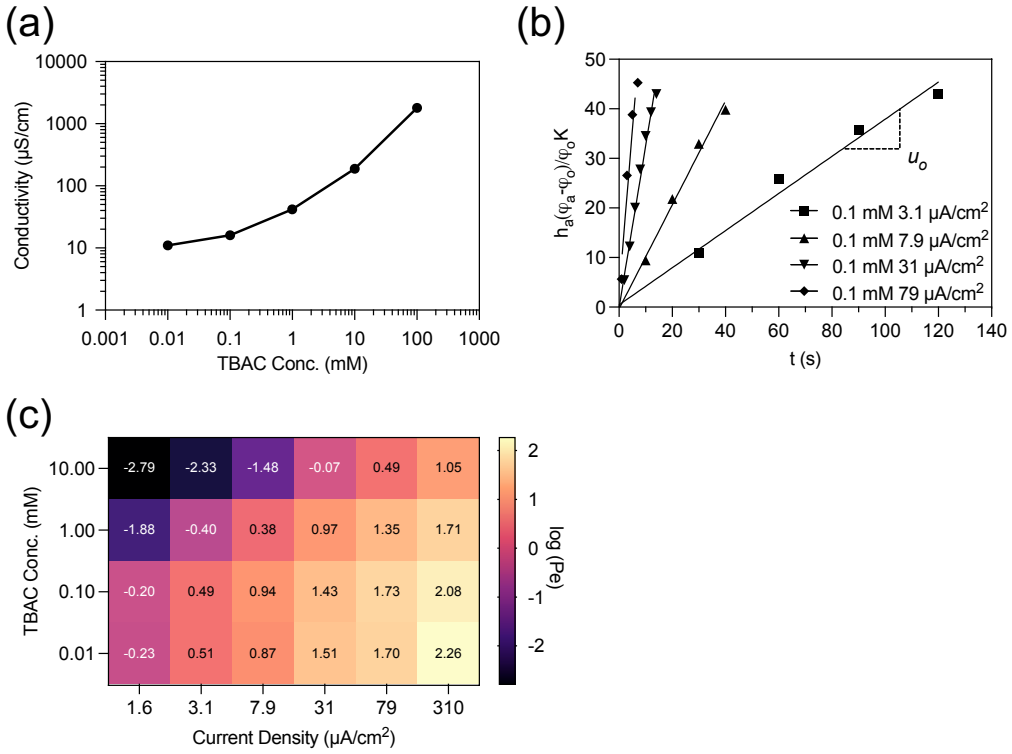


Figure 3.9: Measured deposition rate at various conditions. (a) Measured conductivity of DMSO with different added TBAC concentrations. (b) Measurement and modeling of electrophoretic deposition kinetics. (a) Characterization of the deposition velocity for different operating conditions is made by recognizing that mass conservation requires that the slope of a plot of $\frac{h_a}{K(\phi_o)}\left(\frac{\phi_a}{\phi_o}-1\right)$ vs. t yields u_o, the colloidal deposition velocity. Here h_a is the height of the first (substrate) layer, ϕ_a is the volume fraction of that layer at time t, ϕ_o is the initial particle volume fraction in solution, and the constant $K=(1-\phi_o)^{6.55}$ addresses the volume fraction dependent retardation due to sedimentation. (c) The measured Peclet number (log scale) at different operating conditions, as function of salt concentration and applied current density.

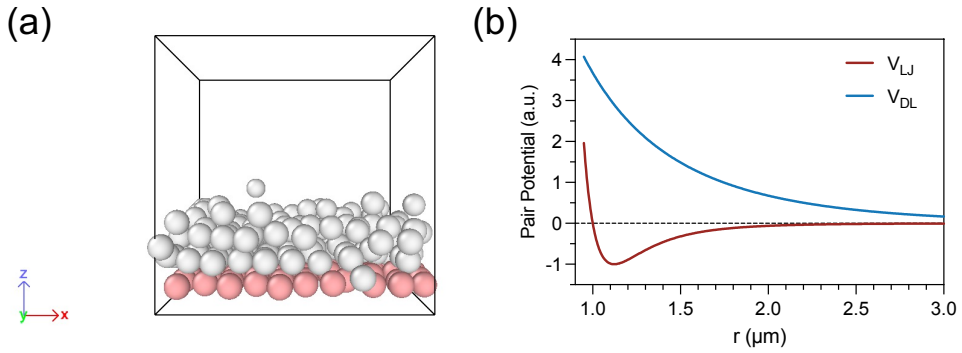


Figure 3.10: Pair potentials in MD simulation. (a) Model for MD simulation of the self-assembly. Bulk (non-surface) particles (white spheres) interact repulsively through V_{DL}, as per the Equation 3.1 illustrated in the main text; particles at the substrate (pink spheres) interact through a Lennard Jones potential, V_{LJ}, which models the effective lateral attraction due to electrohydrodynamic flow. (b) Sample plots of the pair potential for the two types of interactions, at c = 0.1 mM and i = 79 μA/cm^2.

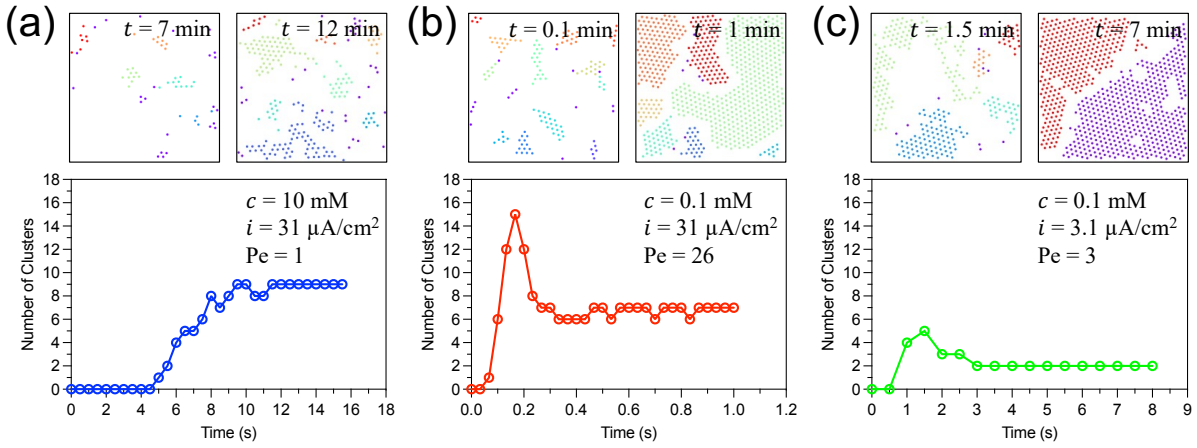


Figure 3.11: Properties of crystal grains. Characterized from the confocal microscopy images of the substrate layer, as captured during the electrophoretic deposition and produced by cluster analysis (cf. Methods). Top rows identify crystalline particles as per the value of $\psi_{6,j}$ at different deposition times t; the bottom row plots how the number of crystal grains in the image changes with time. These structural kinetics are reported for operating conditions: (a) c = 10 mM, i = 31 μA/cm^2 c = 0.1 mM, (b) i = 31 μA/cm^2, and (c) c = 0.1 mM, i = 3.1 μA/cm^2.

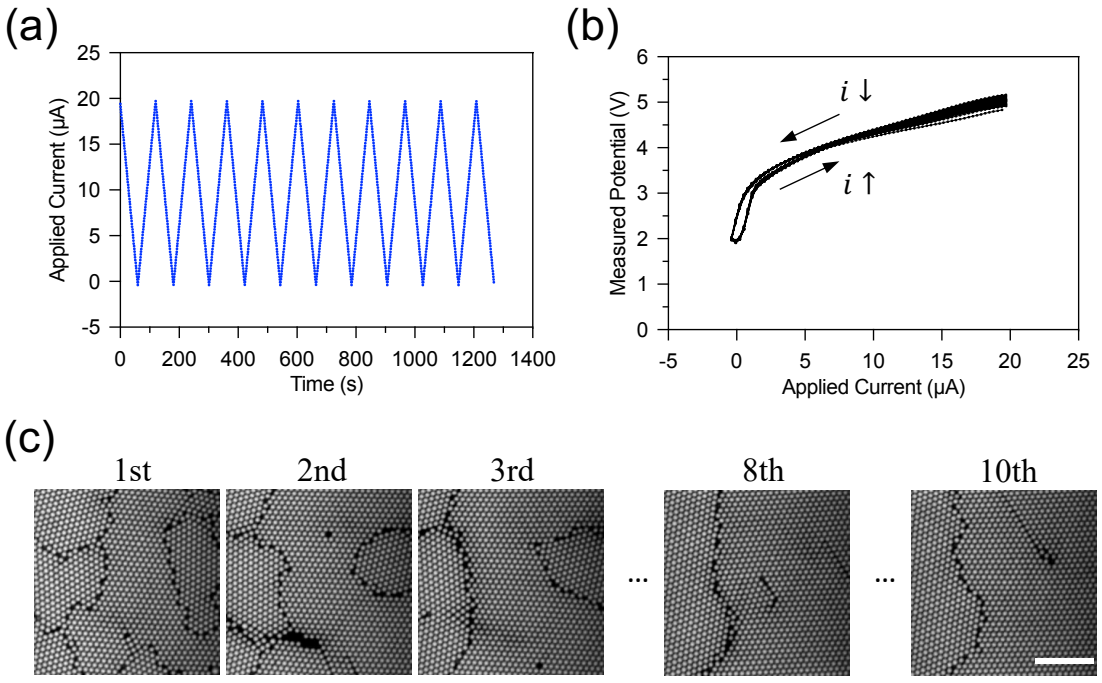


Figure 3.12: Test of reconfigurability of the self-assembled crystals. (a) Cyclically applied current to the device during 10 cycles. (b) The measured potential across the solution cell is also stable during the 10 cycles (data for 10 cycles are overlaid). (c) Confocal microscopy images of the polycrystalline structure captured at the same position after each cycle, also showing reversibility in the structural and crystal grain properties. Scale bar: 10 μm.

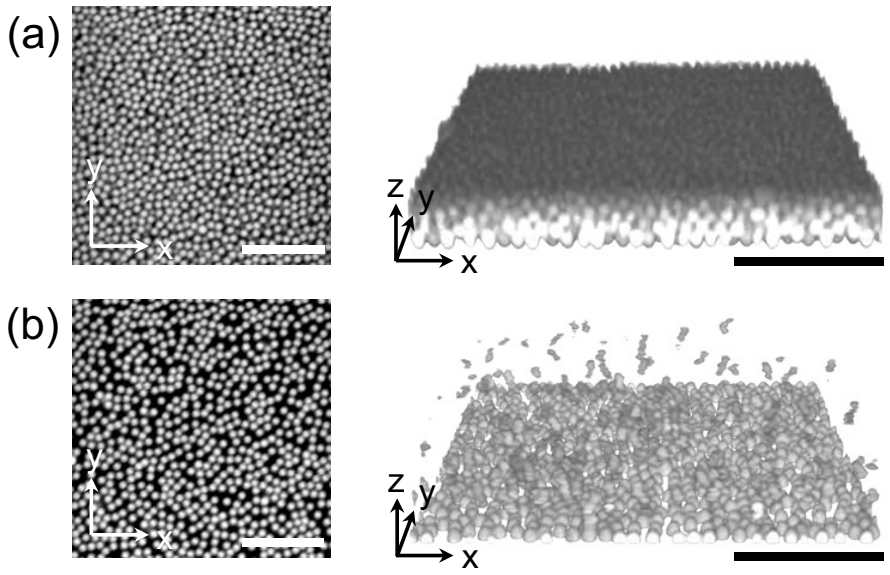


Figure 3.13: 2D and 3D confocal images of particles deposited in the adsorbed region of the state diagrams. (a) When the electric field is on, colloidal particles deposit and form a disordered layer. (b) When the electric field is off for more than 10 min, the bottom layer that is in contact with the ITO surface remains adsorbed. Scale bar: 10 μm.

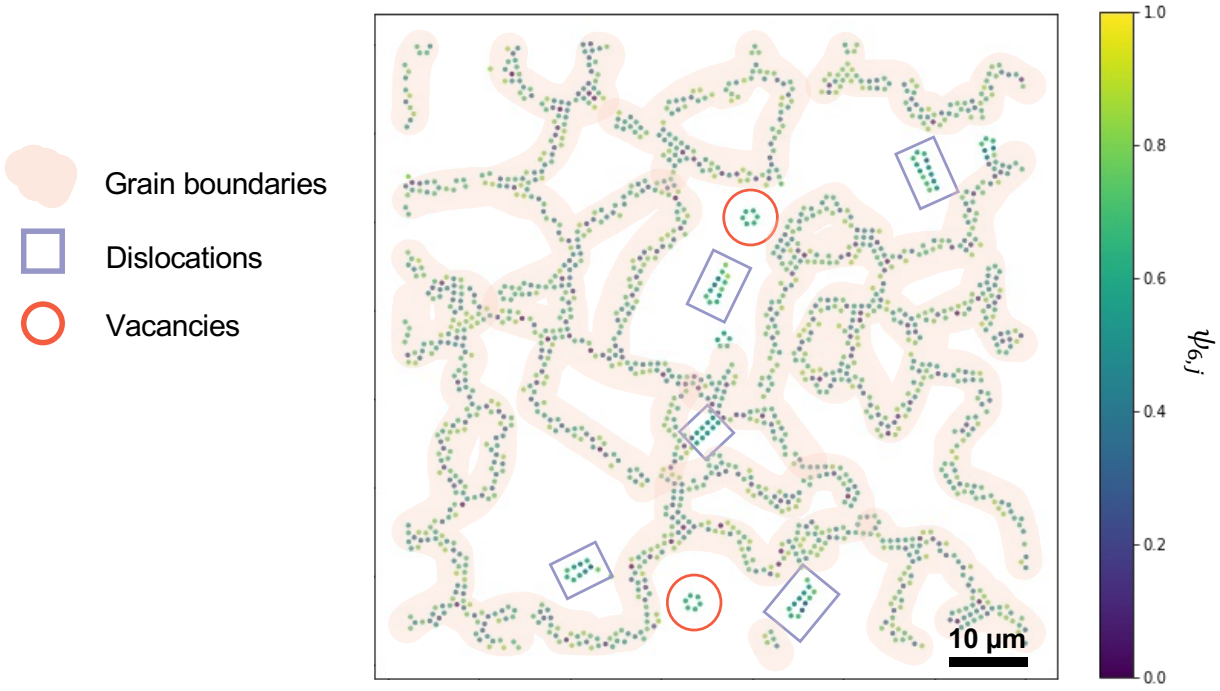


Figure 3.14: Defects categorized by type. Sample image showing different types of defects found in the self-assembled crystals. Image presents only particles with $\psi_{6,j} \leq 0.85$, which is the criterion for a defect particle used in this paper. Grain boundary particles represent >90% defects in this image.

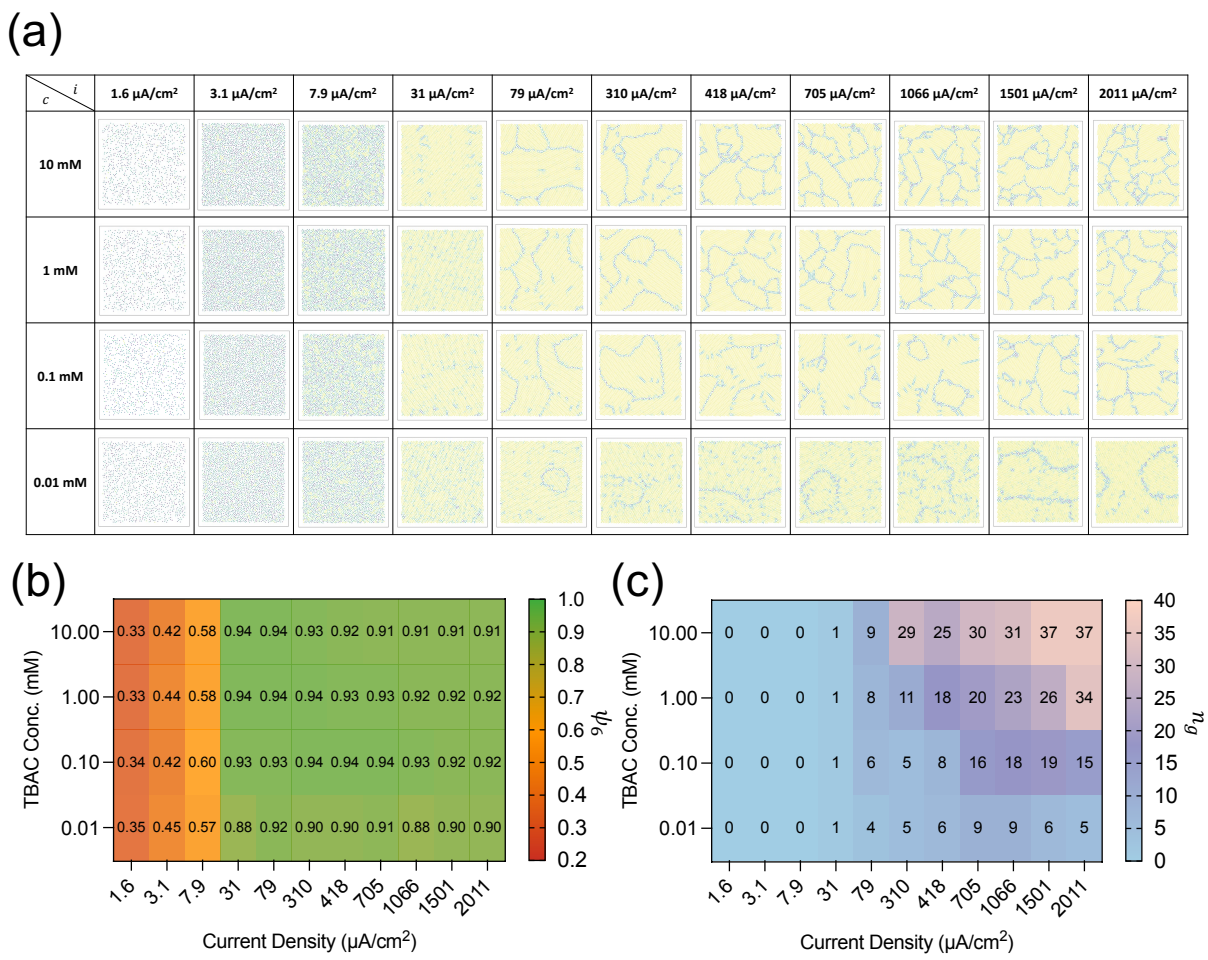


Figure 3.15: Simulated state diagram. (a) State diagram produced by molecular dynamics simulation shows the effect of salt concentration and current density on the self-assembled structure. The units of salt concentration are mM and of the current density are μA/cm^2, and the simulation parameters are given in Table S1 and S2. (b) The calculated average order parameter ψ_6 and (c) crystal grain density n_g identified per 0.01 mm^2 area. Plots in pannel (a) were created by Chih-Mei Young.

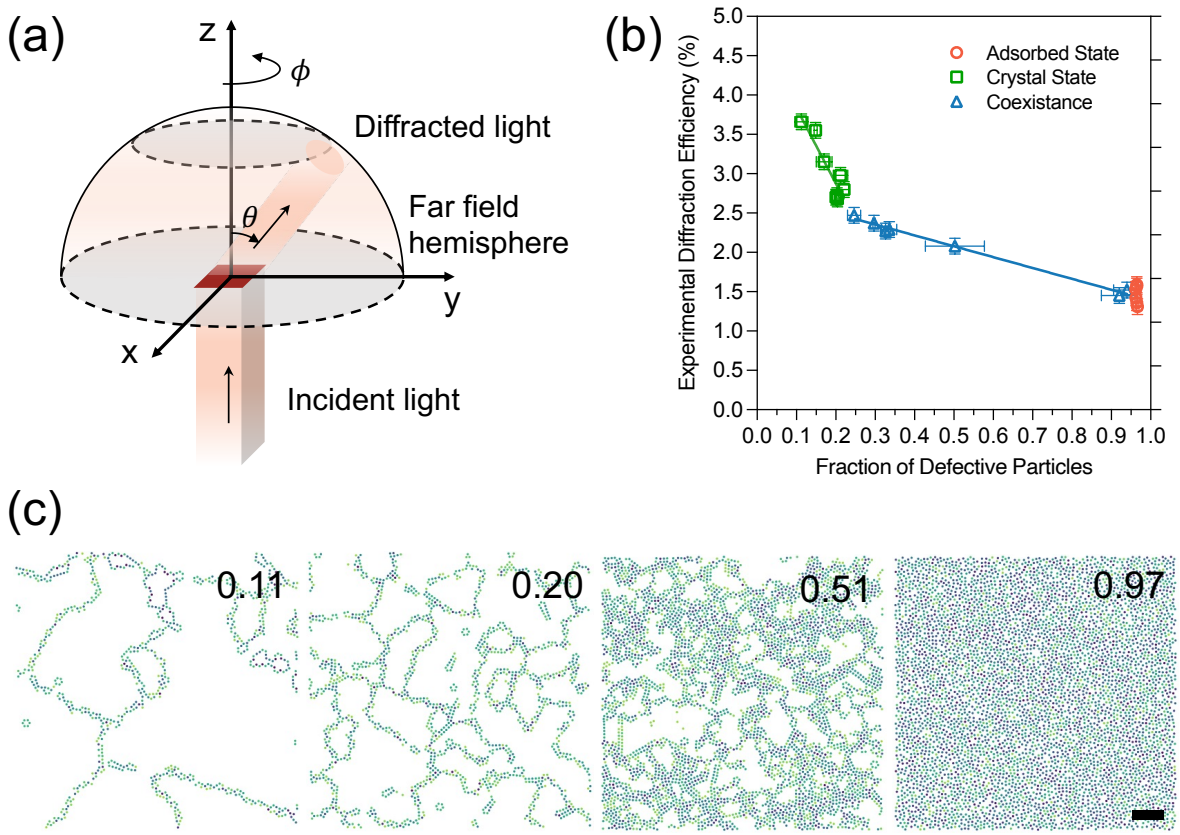


Figure 3.16 Correlation between diffraction efficiency and defect density. (a) 3D schematics of FDTD far field projection symmetry. The MD simulated structure, labeled as the dark red square, is located at the center of the hemisphere that defines the scattering geometry. Incident light was propagated along the z-axis, perpendicular to the sample plane of the red square (xy plane). The diffraction intensity in the far field is a function of the polar and azimuthal angles, θ and ϕ, respectively. (b) The experimentally measured diffraction efficiency decreases as the fraction of defective particles increases ($\psi_{6,j} < 0.85$). (c) Confocal microscopy images showing the spatial distribution of defect ($\psi_{6,j} < 0.85$) particles. The fraction of defect particles for each case is indicated at the upper right corner of the image. Scale bar: 10 μm.

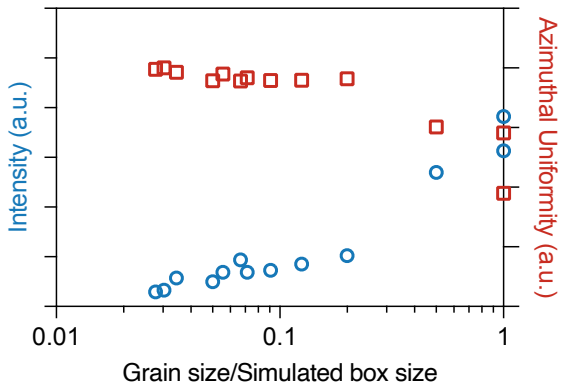


Figure 3.17 Diffraction color properties at different grain size. Larger grain size increases the color intensity but reduces the azimuthal uniformity.

Table 3.1: MD Simulation parameter κ. Estimated for different salt concentrations.

TBAC/DMSO (mM)	κ (1/μm)
0.01	12.6
0.1	40.0
1	126.5
10	400.0

Table 3.2: MD simulated electric field strength and lateral attraction potential. For different current density measured in the experiment.

Current Density i (μA/cm^2)	Electric Field Force F_E (fN)	Lateral Attraction Potential ϵ (k_BT)
1.6	1.4	0.04
3.1	6.6	0.19
7.9	18.8	0.54
31	58.6	1.70
79	117.3	3.40
310	262.5	7.61
418	310.5	9.00
705	414.0	12.00
1066	517.5	15.00
1501	621.0	18.00
2011	724.5	21.00

Chapter 4 Colloidal Crystal Grain Boundary Annealing by Rotating Electric Fields with Six-Fold Symmetry

4.1 Abstract

Periodic external stimuli anneal colloidal crystals by driving particles in the crystal to collectively reorganize, overcome free energy barriers, and adopt lower free energy states with reduced defect levels. In this study, we use a rotating AC electric field of variable amplitude, frequency, and cycle time to progressively convert polycrystals into a single colloidal crystal by annealing of grain boundaries. The electric field was applied to pairs of counter-electrodes in a coplanar device with six-fold symmetry. The field was sequentially rotated among the counter-electrode pairs with a period τ that varied between 3s and 45s. In the first phase of assembly, dipolar interactions and dielectrophoresis compacted polystyrene microparticles of diameter 3.7 μm into a defect-rich polycrystal with hexagonal shape. In the second phase, the cyclic rotation of the AC-field generated dielectrophoretic flow that convected particles in the crystal along closed, triangular paths. Field-induced displacement of the particles induced defect rearrangement; defects, including grain boundaries, were progressively propagated to the edge of the crystal and then expelled. We observed the annealing process by confocal microscopy; analysis of the images yielded the time-dependent hexatic order parameter, phase angle, and Voronoi diagrams of all the particles. The dielectrophoretic force that yielded the particle deformation was controlled by means of the frequency (ω) and amplitude (A) of the rotating AC electric field. The operational range for complete annealing of the crystal was $A > 4$V and ω <5

kHz. In addition, a cycling period of $\tau \sim 15$s achieved the maximum crystal quality as characterized by the ψ_6 order parameter. Annealing by means of a rotating field with six-fold symmetry therefore significantly improves the rate of defect removal from colloidal crystals, ultimately generating a defect-free crystal over a duration ranging from 20 to 200 min. Computations of the local deformation field due to the dielectrophoretic force were analyzed to yield an effective, position dependent active energy of particles in the crystal. This active energy correlated well with the time-dependent changes in defect dynamics and crystal quality, thereby establishing a potential explanation of the mechanism of annealing as an activated process.

This chapter was adapted from manuscript in preparation for publication by Tianyu Liu, Syahidah Mohd Khairi, and Michael J. Solomon. Tianyu Liu conducted the experiment with assistance from Syahidah Mohd Khairi. Tianyu Liu designed and fabricated the six-fold coplanar device. Syahidah Mohd Khairi built the software and hardware for auto-control circuit of AC signal. Tianyu Liu developed code for analysis of the confocal images. The microelectrode devices used in this work were fabricated at Lurie Nanofabrication Facility (LNF) at the University of Michigan.

4.2 Introduction

Colloidal particles dispersed in a liquid phase may self-assemble into crystals; however, these ordered microstructures, especially those produced rapidly, typically contain defects. Such self-assembly is often accomplished with the assistance of external stimuli, including centrifugation as well as optical[33], magnetic[21], and electric fields[18,20,31,43]. These approaches are especially prone to produce defect-laden crystals. However, materials possessing low levels of defects are associated with enhanced functional properties. Functional properties of crystalline materials affected by crystal quality include mechanical strength[158], electrical conductivity[159],

and optical properties[17]. For example, with respect to the last property, the diffraction intensity of a colloidal crystal grating was shown to be sensitive to crystal quality; higher diffraction efficiency was correlated with better long-range crystalline order[31].

The types of defects present in colloidal crystals include grain boundaries, dislocations, disclinations, and vacancies[42,160,161]. The diffusion of defects in colloidal crystals is slow[9,162]. External stimuli can not only induce self-assembly of colloids but also initiate local structural rearrangements that impact crystal quality. Thus, the crystal is annealed by the external stimuli, which introduces energy activates particles to rearrange locally. For example, by introducing Janus particles into a polycrystalline array, defect annealing was accomplished through local rearrangements generated by the active motion of the Janus particles[9,162]. In addition, a pulsed laser power can transform colloidal crystal films into interconnected nanostructures[163]. Injected energy can also initiate annealing over macroscopic areas. For example, by optimizing the properties of an acoustic wave, *Menath et al.* showed that the grain size in interfacially assembled 2D colloidal crystal monolayers were increased by about two orders of magnitudes. MD simulation identified two mechanisms for the colloidal crystal annealing. One was the transport of particles between adjacent grains; the second was collective grain rotation, which was described as grain rotation around its center to resolve misorientation relative to neighboring grains[27].

For colloids of diameter ~ 1 μm at room temperature in water, the Brownian diffusivity is low (D = 0.22 $\mu m^2/s$.) Rearrangements that can generate annealing are therefore slow; the characteristic time for these colloids to diffuse their own diameter is ~ 2.3s. Although the defects generated during self- and directed assembly may not be stable at equilibrium, the slow dynamics of colloids in this size may mean that infeasibly long times are required to eliminate

them from the system. A potential approach to address this problem is to input external energy into the system. This external energy can increase particle dynamics, thereby speeding the resolution of defects. Among the range of external fields available, AC electric fields are an appealing choice because these field both couple to a broader range of materials and can be easily tuned in strength and orientation.

Applied AC electric fields can also induce dipolar interactions between colloidal particles; such interactions can affect phase behavior and microstructure. Example structures include chains and 2D crystals with 1D symmetry[34,35]. Moreover, *Kao et al.* showed that the cyclic application of AC electric fields can anneal defects from colloidal crystals, thereby enhancing crystal quality[42]. In this study, the AC electric field was applied between parallel counter-electrodes in a fixed configuration. The work identified an optimum period of the cyclic field, approximately one-half the melting time of the crystal. *Zhang et al.* studied the application of multi-directional fields with two pairs of polarized electrodes in a square configuration. These fields created a time-dependent free energy landscape[164]. This approach, when combined with machine learning and feedback control, removed grain boundaries initially present in the crystal[45,164]. Such time and orientation dependent fields represent a new class of annealing strategies to resolve defects in colloidal crystals. However, the role of field characteristics—including its variation in space and time—on annealing kinetics and performance have yet to be investigated. In addition, the hierarchy of mechanisms that accomplish annealing have yet to be proposed and studied.

In this study, we designed a device for colloidal self-assembly with co-planar counter-electrodes located with six-fold orientational symmetry. A cyclic AC electric field was applied, which generated annealing of self-assembled colloidal crystals. When the orientation of the AC

electric field was circularly rotated strong local, cyclic motion of the colloids was observed. This deformation induced progressive local rearrangements of particles in the crystal. The rearrangements progressively acted to expel defects and grain boundaries from the crystal. This annealing could be optimized by varying the frequency and voltage of the electric field as well as the cycle time of its rotation in orientation. We characterized the cyclic deformation of the particles in the crystal as well as the time evolution of their hexatic order parameter (ψ_6), the crystal grain number density, and the Voronoi tessellation of the crystal. We provide a hypothetical mechanistic explanation of the annealing.

4.3 Methods

4.3.1 Fabrication of coplanar microelectrode device

The geometry of the 6-fold micro electrode device, or the photomask used in photolithography, was designed using a 2D computer-aided design software called Klayout. The electrode tips were rounded with radius of curvature of 100 μm; this dimension avoided breakdown and discharge at the electrode-solution interface[165]. The distance between the paired counter electrodes was 300 μm. The coplanar microelectrode device was fabricated at Laurie Nanofabrication Facility at University of Michigan. A glass coverslip (50x35mm) was coated with 7.5 nm of Chromium and 15 nm of gold using physical vapor deposition (Angstrom Engineering Evovac Evaporator). The pattern was transferred using photolithography. Before experiments, the glass was cleaned by sonication in acetone (15 min), isopropyl alcohol (IPA) (15 min) and 1M of potassium hydroxide solution in IPA (30 min). Then the glass was sonicated in poly(sodium 4-styrenesulfonate) (PSS) in 0.5 M KCl (15 min) to prevent particle sticking[99].

4.3.2 Preparation of the colloidal suspension

The colloidal crystals were self-assembled from monodisperse polystyrene latex microspheres (Thermo Fisher Scientific, F8858, lot 2500452). These colloidal particles were 3.70 ± 0.04 μm in diameter; they emitted red fluorescent (emission peak wavelength of 605 nm). The colloidal solution was prepared by resuspending the particles in 0.1 mM NaCl solution with a concentration of 0.031 vol% measured by hemocytometer, equivalent to monolayer coverage. In a typical experiment, about 13 μL of colloidal suspension was added to the center of device. The chamber dimensions were controlled by a spacer (1 mm in height, 5 mm in diameter). The solution was allowed to rest for at least 30 min prior to experiments; the colloids sedimented to the bottom of the chamber within this period.

4.3.3 Application of the rotating electric field

The six-fold coplanar device has three pairs of electrodes; each pair of electrodes faced each other. A square wave AC electric field was applied across each pair by an AC waveform generator (RIGOL, DG1022). The field amplitude and frequency varied between 3 - 7 V_{rms} and 1-30 kHz, respectively. A cycle of the rotating AC electric field consisted of three phases. In each phase, one pair of electrodes was powered by the AC field, while the other two pairs were disconnected. The configuration was rotated clockwise to perform the next phase of the cycle. The period of the three-stroke cycle varied from $\tau = 3$ to 45 s. The connection and disconnection of the electrode pairs with the waveform generator was controlled using a relay module (Songle, SRD-05VDC-SL-C, 8-channel) and an Arduino Leonardo microcontroller. The relay module switched the connection on and off between each electrode and the waveform generator as per instructions programmed into the microcontroller.

4.3.4 Characterization of the self-assembled colloids

The microstructure of the self-assembled colloids was visualized by confocal laser scanning microscopy (Nikon A1R with 100x, excitation wavelength 561 nm, NA 1.45 oil immersed objective). A series of 512x512 pixel images (0.25 μm/pixel resolution) were captured (at 1 fps) during self-assembly and annealing. Particle location and tracking were performed using TrackMate in Fiji[166], tracking error 9 nm. The centroidal coordinates of all particles in each frame were exported and analyzed using customized Python program. The local hexatic order parameter ($\psi_{6,j}$) was computed as per: $\psi_{6,j} = \frac{1}{N_j}\sum_{k=1}^{N_j} e^{i6\theta_{jk}}$, where θ_{jk} is the angle between the vector connecting sphere *j* and its neighbor *k* relative to an arbitrary reference frame. Here, the modulus of $\psi_{6,j}$ represents the local crystallinity around particle *j*, and the phase angle indicates the orientation of the hexatic bonds around that particle relative to the reference frame. The quality of a crystal, represented by ψ_6, was the average of the individual $\psi_{6,j}$ for all particles in each image frame. In addition, the Voronoi cell of each particle was determined by applying an algorithm available from the freud library, an open-source Python package[151].

Particle dynamics were determined separately by analyzing a series of 512 x 512 images (0.25 μm/pixel) acquired at an increased frame rate (10 fps). Particle tracking using TrackMate linked the particles with unique identifiers, therefore allowing visualization of particle trajectories[166]. In addition, the velocity of each particle was determined from the ratio of the frame-to-frame displacement to the time lapse. The velocity at each frame (frames acquired at an interval of 0.1s) was calculated by reference its current location to the location of the particle ten frames after (1s interval). This procedure was adopted to minimize the effect of Brownian motion and image analysis error on the measured velocity, but still sample the velocity at high resolution. The direction of the velocity was determined relative to the reference frame.

4.3.5 Calculation of field strength and driven forces

The electric field in the central region of the six-fold coplanar device was simulated using 2D COMSOL Multiphysics. The geometry (1000x1000 µm) is constructed from a CAD file of the photolithography mask. Material properties, including the dielectric constants of the solution and the conductivity of the metal layer, were taken from the literature[167,168]. The conductivity of 0.1mM NaCl in water was 18.2 mS/cm, measured by a conductivity meter (EC11, Horiba Scientific). A boundary condition of 5V was set at two of the counter electrodes, while no potential drop is set at other liquid-electrode interfaces. The mesh size varies between 10-40 µm, as determined by the local geometry. The simulation calculated the position dependent electric field profile $\boldsymbol{E}(x, y)$. We then numerically determined $\boldsymbol{\nabla E}^2(x, y)$ in both e_x and e_y direction, as used in the calculation of the dielectrophoretic force.

4.4 Results

4.4.1 Experimental setup with automated AC electric field

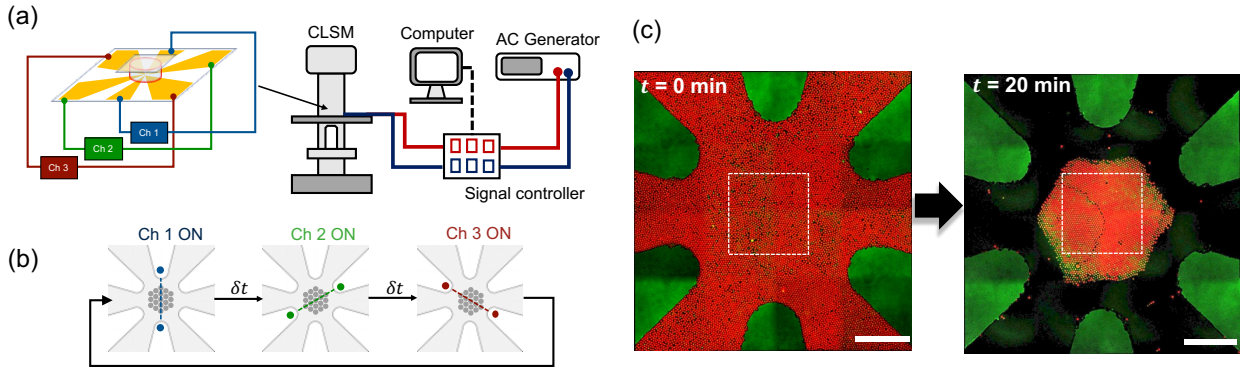


Figure 4.1: Rotating electric field device setup. (a) Schematic of device with six-fold electrode symmetry for application of rotating electric fields. A preprogrammed signal controller connected to an AC power generator produces an electric field that is cyclically rotated by sequentially energizing three pairs of counter-electrodes, shown as Channel 1, 2 and 3. Confocal microscopy (CLSM) was used to visualize the microstructure of the self-assembled crystal. (b) The applied electric field was cycled clockwise with a constant period τ. (c) Stitched CLSM images of the device before and after the application of the AC electric field. The dash line box marks the region of the self-assembled crystal that was imaged at high resolution. The green and red channels image the electrodes and colloids, respectively. Scale bar: 100 µm. The signal controller shown in panel (a) was built by Syahidah Mohd Khairi.

Colloidal self-assembly and annealing were performed in a device that applied an orientationally variable AC electric field across counter electrodes positioned with six-fold rotational symmetry. As shown in **Figure 4.1**a, a programmed and controlled square wave AC electric field of constant amplitude (A) and frequency (ω) was applied across pairs of oppositionally positioned electrodes as per the sequence illustrated in **Figure 4.1**b. After initial deposition under gravity, the colloidal particles (red) packed into a disordered structure with some local crystalline ordering. The distribution of particles on the bottom surface of the device was uniform. When the rotating electric field was initiated, colloidal particles displaced under the action of the electric field towards the center of the device. They quickly self-assembled into a crystal, as shown by the central red region of the image in **Figure 4.1**c. This crystal, here self-assembled under the conditions $A = 5V_{rms}$, $\omega = 5$ kHz and $\tau = 15$s, displays a hexagonal shape after 20 minutes of field cycling. The green channel in this image shows the microelectrodes.

4.4.2 Characterization of the microstructure during annealing process

Figure 4.2a reports CLSM images of the central region of the self-assembled crystal at different times in the process. The position and local bond orientation of each particle was identified by image analysis (c.f. Methods); **Figure 4.2**b shows this identification, with each particle labeled by its phase angle. Initially, the colloidal microstructure was disordered. The imposition of the rotating electric field concentrated the particles in the central region of the device; a liquid to crystal phase transition occurred during this period. After 3 min of self-assembly, the microstructure was polycrystalline; small crystallites were each oriented at different phase angles. As time progressed ($t > 10$ min), the cyclic electric field removed grain boundaries and reduced the number grains. After application of the rotating field for 30 min, only two crystal grains remain. The remaining grain boundary separating them progressively

migrated away from the center of the crystal between 30-180 min. This grain boundary was expelled from the crystal by t = 220 min; the initial polycrystal was thus fully converted to a single crystal.

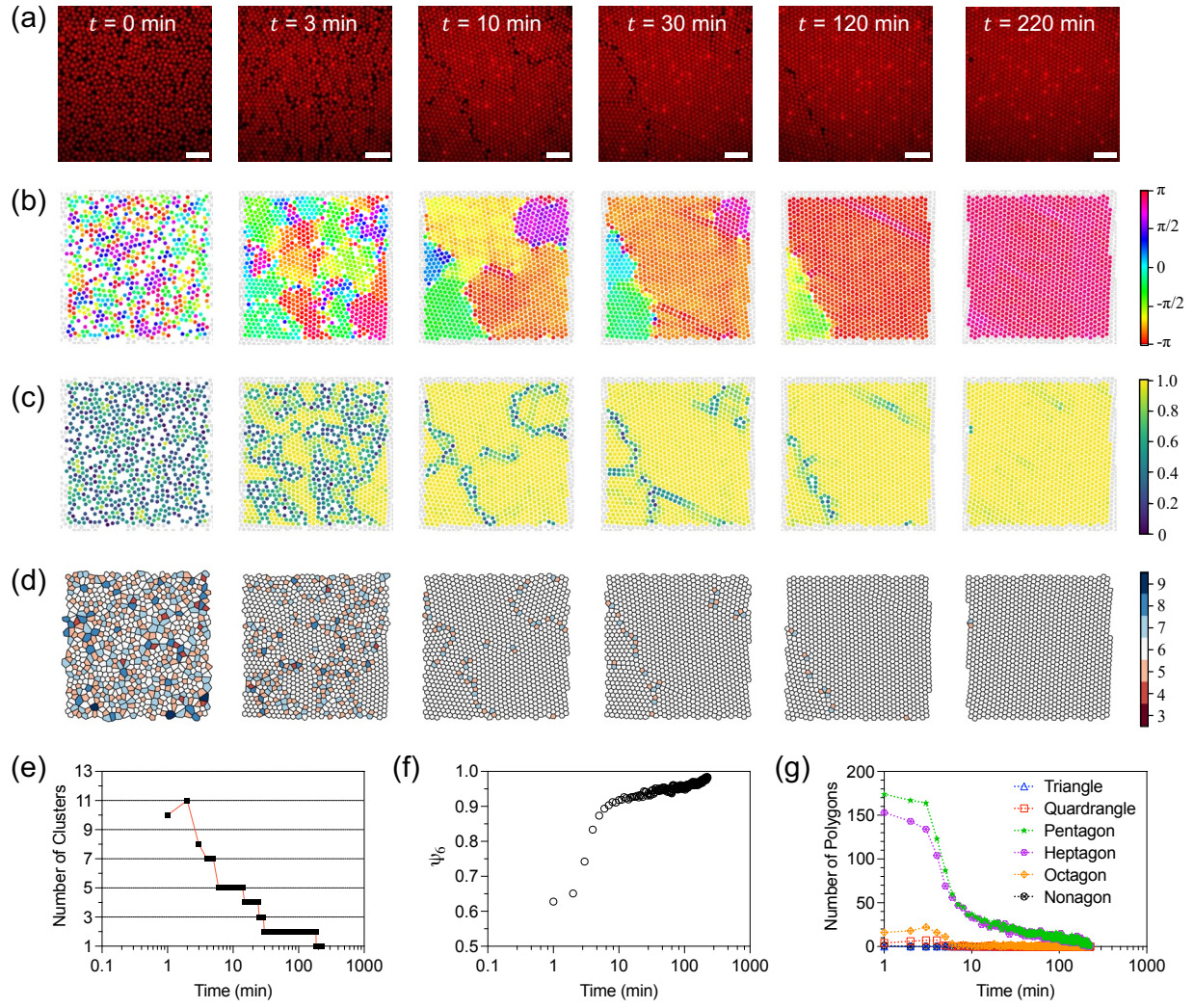


Figure 4.2: Analysis of particle positions in the colloidal crystals as a function time during self-assembly and annealing. The experiment was performed at an applied voltage, frequency, and period of A = 5V$_{rms}$, ω = 5 kHz and τ = 15s, respectively. CLSM images of the colloidal crystal structure are shown in panel (a). Particle locations in each frame are coded by phase angle (b) and modulus (c) of $\psi_{6,j}$ and Voronoi tessellation (d). Panel (e), (f), (g) show the time evolution of the number of clusters, average hexatic order parameter, and number of different Voronoi polygons, respectively. In (g), polygons were categorized by the number of sides, here reported for N = 3, 4, 5, 7, 8 and 9.

Figure 4.2b and c display how the phase angle and magnitude of $\psi_{6,j}$ evolved for each particle during this period. The particle-level assignment of $\psi_{6,j}$ clarified the number of crystal

grains (**Figure 4.2**b) and confirmed the grain boundary dynamics (**Figure 4.2**c). The time-dependent Voronoi diagram of the crystal characterized features of the non-crystalline order at the grain boundaries (**Figure 4.2**d). Defects were indexed as polygons with edge number different from six and labeled by color on the figure.

The time-dependence of grain number, crystal quality, and Voronoi polygons are plotted in **Figure 4.2**e, f, and g, respectively. The number of grains (**Figure 4.2**e) progressively declines, until only a single grain remains for t > 180 min. **Figure 4.2**f plots the time dependence of the average magnitude of the hexatic order parameter in the imaged region. This value increases sharply during the initial period of particle concentration and phase transition. After about 10 min, the ψ_6 continues to increase, albeit at a lower rate. Steady state, here defined as the time by which ψ_6 is constant to within 1% during a 10-minute period, occurs at 180 min, in accord with the evolution of the grain number. ψ_6 = 0.96 at that time. The progress of annealing is also apparent from the time dependence of the Voronoi polygon abundance, as shown in **Figure 4.2**f. At early times (t < 10 min) the number of polygons that are not hexagons decreases rapidly; within this period nearly all polygons with 3, 4, 8, or 9 edges disappear. Pentagons and heptagons persist, however. These two Voronoi shapes are present in about equal number. Their numbers also decrease until ~ 200 min. At that time their abundance decreases to less than 5, consistent with a crystal of nearly ideal coordination number.

4.4.3 Particle traveling velocity and triangle trajectory

The changes in microstructure, defects, and crystal quality reported in **Figure 4.2** occur while the particles in the crystal undergo cyclic displacement. **Figure 4.3**a plots the average position of all particles in a cycle for the condition $A = 5V_{rms}$, ω = 5 kHz and τ = 15s; the average magnitude of each particle's velocity (c.f. Methods) during the cycle is indicated by the

color. The velocity varies spatially. Particles at the center move slowly—their average velocity less than 0.2 μm/s—while the particles close to the boundary display a higher velocity—0.8 μm/s or greater. The origin of the spatially varying velocity is related to the spatially variation of the electric field, which yields a position dependent dielectrophoretic force, as discussed subsequently.

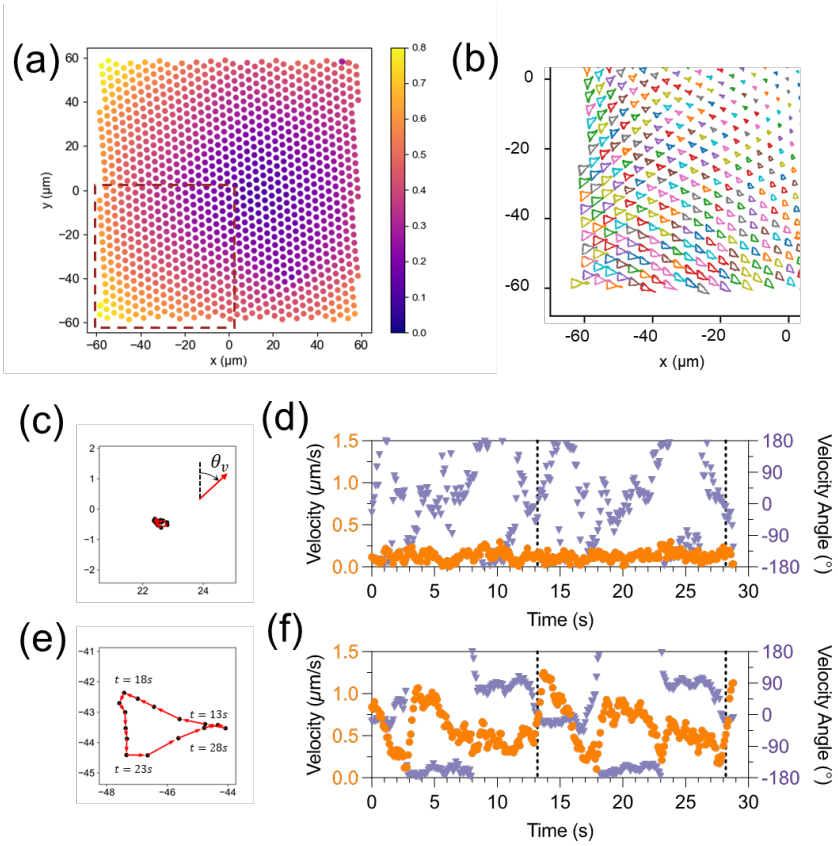


Figure 4.3: Particle trajectories induced by the rotating AC electric field. (a) The average velocity of all particles in the central region of the self-assembled colloidal crystals at t = 200 min. Data are for two cycles of field rotation at the experimental conditions of $A = 5V_{rms}$, $\omega = 5$ kHz and $\tau = 15$s. The particles are shown at their average positions; they are colored by their average velocity. Boxed area corresponds to the area in panel (b). (b) The trajectories of particles during one cycle (at t = 200 min) are plotted. (c)-(f) The displacement and velocity of representative particles are shown. (c) and (d) are for a particle close to the center and (e) and (f) are for particles far from the center. In (c) and (e), the black points show the particle centroids, and the red arrows show the magnitude and direction of the velocity at each time step (Δt = 1 s). (d) and (f) The velocity magnitudes and directions labeled with orange and purple markers, for the particle shown in (c) and (e), respectively. Dash line labels show the beginning and end of a cycle.

Figure 4.3b shows that the particles execute triangular, closed loop trajectories. This triangular trajectory is consistent with the sequence of the AC electric field cycle. The distance

the particle travels during each step of the AC field sequence varies with the radial position of the particle in the crystal. For example, a particle located close to the center exhibits less movement, as illustrated by the trajectory of a sample particle shown in **Figure 4.3**c. The velocity magnitude and direction of the particle is shown for two consecutive cycles. **Figure 4.3**d confirms that the particle velocity is less than 0.2 μm/s at this position in the crystal. Its direction of motion is also highly variable; the triangular motion apparent in **Figure 4.3**b is not observable in this sample trajectory.

However, a particle located far away from the center—here at x = -43 μm, y = -46 μm—exhibits a trajectory of better-defined direction and higher velocity (c.f. **Figure 4.3**e). Here, the field first rotates into a new position at t = 13s. (This corresponds to the case where the field oriented along an axis connecting the electrodes at 120° and -60°, with angles specified clockwise.) At t = 18s, the AC field is switched to channel 1 (aligned along an axis from 0° to 180°). At t = 23s, the AC field is switched to channel 2 (aligned along an axis from 60° to -120°.) During each stroke of the cycle (c.f. **Figure 4.3**f), the particle initially accelerates from a residual velocity of ~ 0.2 μm/s to a velocity ~1 μm/s. The velocity subsequently declines to a value of approximately 0.5 μm/s by the end of the stroke. Also as shown in the figure, the direction of the particle is well-defined, rapidly changing at the beginning of each stroke by 60° and maintaining a consistent direction during the stroke of the cycle.

4.4.4 Structural evolution under various AC frequencies

The annealing behavior of the AC electric field depends on the amplitude and frequency of the field. **Figure 4.4**a shows the time-dependent microstructure of the crystal at ω = 1k, 3k, and 10k Hz for fixed $A = 5V_{rms}$ and τ = 15s. At 1 kHz, particles assembled into a single crystal quickly, in about 15 min; however, the shape of the crystal's boundary was initially irregular. At

this condition the particles were disordered; the center appeared more organized than the edges. At 3 kHz, a polycrystal was initially obtained; it converted into a single crystal after 45 min of cyclic field application. Complete annealing of the crystal at 10 kHz was however not observed; grain boundaries persisted for the full duration of the experiment (90 min). Here, we define complete annealing as the transformation of the initial polycrystal into a single crystal.

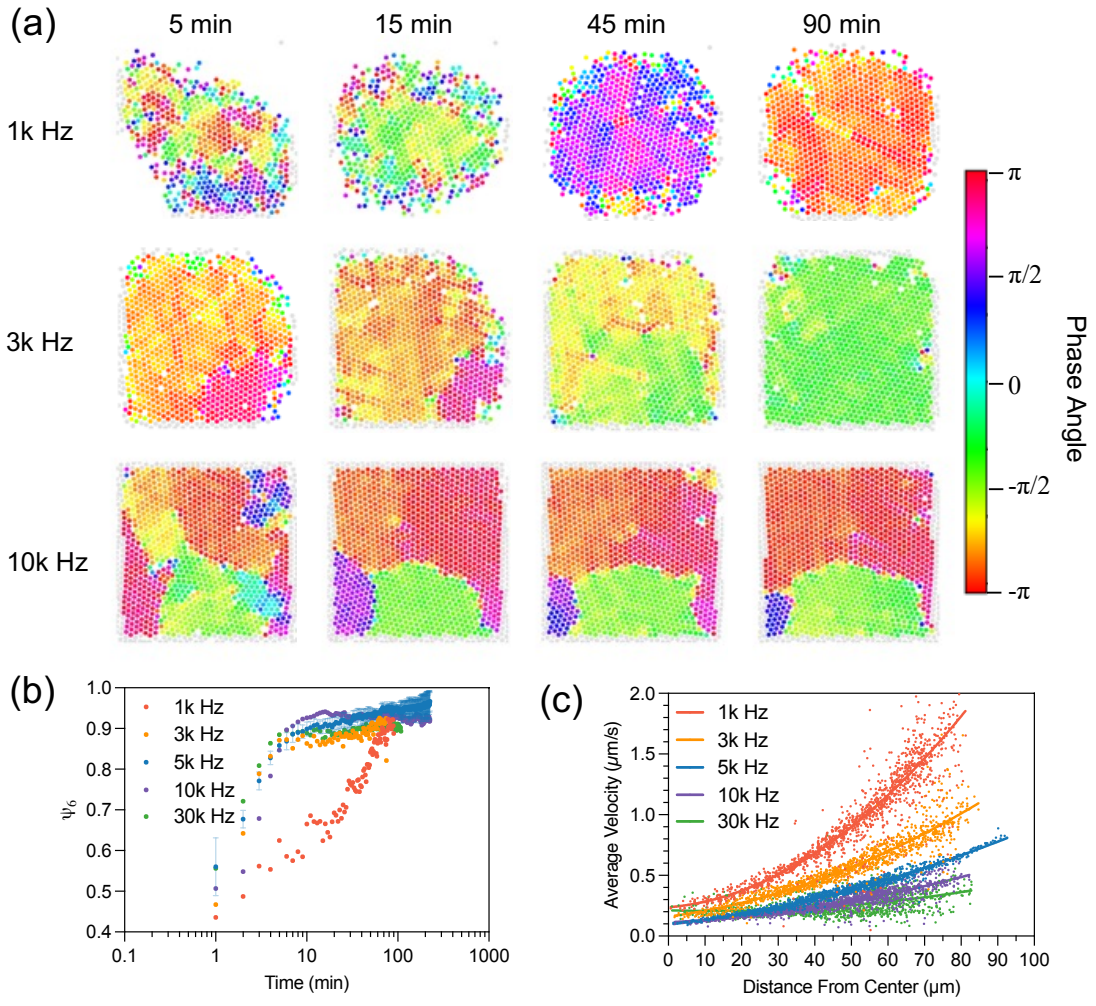


Figure 4.4: Control of driving forces and the effect on annealing performance. (a) Time evolution of colloidal crystal structure at $A = 5V_{rms}$, $\tau = 15s$, and ω between 1-10 kHz. Particle centroids are colored by the phase angle of their hexatic order parameter, ψ_6. (b) Magnitude of the hexatic order parameter vs time for the different AC field frequencies. (c) The average velocity of particles as a function of distance from the center of the self-assembled colloidal crystal.

Figure 4.4b shows the ψ_6 evolution for the different conditions. The time evolution of ψ_6 is very similar within the range ω = 3 - 30 kHz, with only the following difference between

the 3 kHz and 5 kHz cases relative to the 10 and 30 kHz cases: At 3 kHz and 5 kHz, ψ_6 continues to increase over the full duration of the experiment, indicating that annealing is not complete by the conclusion of the experiment. On the other hand, at 10 kHz and 30 kHz ψ_6 attains a constant value. For the ω = 1 kHz case, it takes longer time for the disordered colloids to assemble into a crystal with high ψ_6; the transformation at this condition is about an order of magnitude slower than the others.

Figure 4.4c shows the radial variation of the average particle velocity (calculated for each cycle) across the five frequency conditions. Consistent with **Figure 4.3**, the particle velocity increases with radial distance at every condition tested. In addition, the velocity curves shift lower as the frequency of the AC field increases; decreasing the frequency creates a stronger electric field that drives particle displacement. However, this increased particle displacement does necessarily translate to more rapid crystallization or annealing, because, as **Figure 4.4**b shows, ψ_6 increases more slowly in 1 kHz case, even though the particle velocity is at its greatest.

4.4.5 Annealing performance vs. operating conditions

Experiments were conducted to show the effect of operating conditions on the annealing performance. We studied the effects of AC amplitude, frequency, and cycling period separately; **Figure 4.5** plots ψ_6 and the final number of crystal grains for the conditions studied. The three-variable parameter space of τ, A, and ω was sampled in three ways. In each, one parameter was varied while the other two were held constant. The optimal average local orientational order, as measured by ψ_6, was identified at ω = 5kHz, A = 5V and τ = 5 s, respectively (c.f. **Figure 4.5**a, c, and e). Complete annealing—defined as evolution of the structure to a single crystal grain—

occurred over a broader range of conditions. This condition was satisfied at $\omega \leq 5$ kHz, $A \geq 5$V, and $\tau \geq 5$s, as demonstrated by **Figure 4.5**b, d and e, respectively.

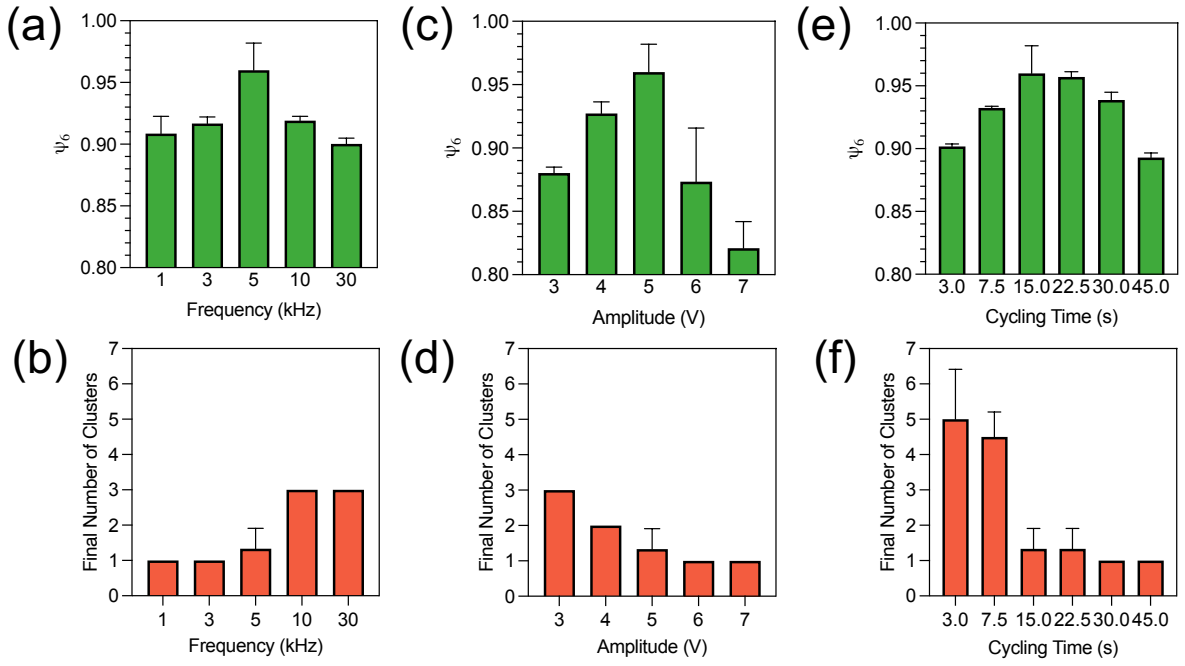


Figure 4.5: The effect of AC electric field operating condition on annealing performance. ψ_6 and crystal grain number are shown as frequency, amplitude and cycle time are varied. (a)-(b) A = 5 V_{rms}, ω = 1-10 kHz, and τ = 15s. (c)-(d) A = 3-7 V_{rms}, ω = 5 kHz, and τ = 15s. (e)-(f) A = 5 V_{rms}, ω = 5 kHz, and τ = 3-60s.

4.4.6 Dielectrophoretic force and active energy injection

The computed (vector) electric field in the six-fold device is shown in **Figure 4.6**a. Here the top and bottom electrodes are polarized with a voltage offset of 5V. The field shows strong magnitude around the electrodes; it is weaker at the center. The field is symmetric about both the x and y axes and the magnitude and direction of the field are a function of both x and y.

Because of the position dependent electric field, the dielectrophoretic (DEP) force and dipolar force vary across the device. The DEP force is determined by the equation,

$$\boldsymbol{F}_{DEP} = 2\pi a^3 \varepsilon_{\mathrm{m}} \mathrm{Re}|\mathrm{CM}(\omega)| \cdot \boldsymbol{\nabla}|\boldsymbol{E}|^2 \qquad 4.1$$

In this equation, ε_m is the dielectric constant of the medium, which is 6.95×10^{-10} F/m for water, and E is the electric field strength. Here, Re|CM(ω)| is a function of the frequency ω of the AC field (in radians), calculated as shown in **Table 4.1**.

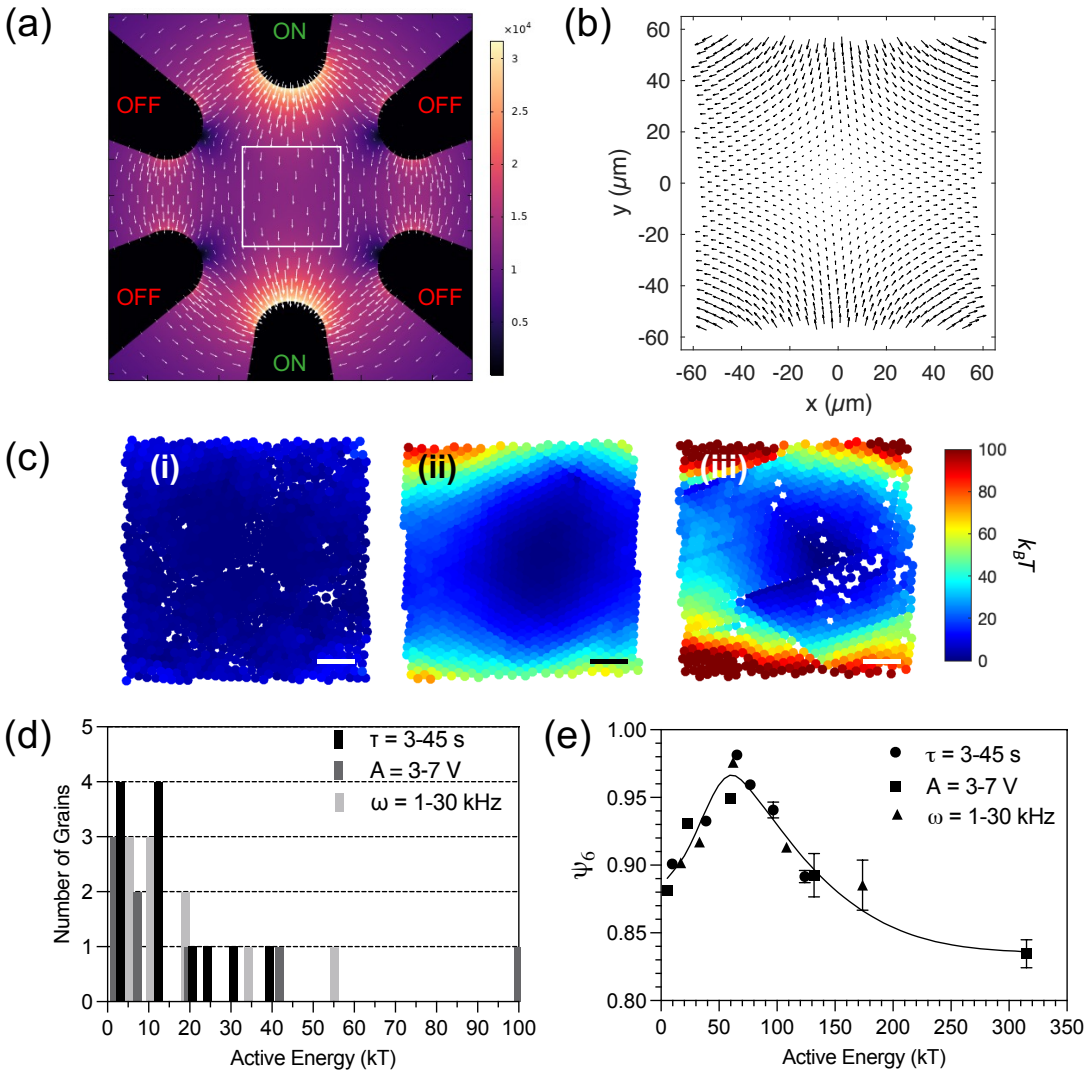


Figure 4.6: Annealing as an activated process. (a) computed electric field magnitude (color) and direction (white arrow) when the top-bottom electrodes were offset by 5V. (b) Calculated DEP force for the central region device, denoted by the box in (a). Vectors represent both direction and scaled magnitude of the force. (c) Active energy generated by the DEP work (c.f. text) of each particle when the electric field is applied for (i) 1s, (ii) 5s, and (iii) 15s, at ω = 5 kHz and A = 5V. (d) The correlation between active energy and number of crystalline grains after 3h of annealing experiment, for different cycling period (circle), amplitude (squares) and frequency (triangles). (e) The overall quality of the crystal, characterized by ψ_6 after 3h of operation, correlated with the average active energy input by the field conditions of varying period, amplitude, and frequency of the AC field cycle. The curve plotted is to guide the eye.

The vector field $\boldsymbol{F}_{DEP}(x, y)$ is plotted in **Figure 4.6**b, using **Figure 4.6**a as input. **Figure 4.6**b shows that the DEP force is small at the center of the device; it grows rapidly as the distance from the center increases.

Particles that undergo dielectrophoretic motion perform work. Specifically, this work $W_{a,i} = \boldsymbol{F}_{DEP,i} \cdot \boldsymbol{\Delta x_i}$, the dot product of $\boldsymbol{F}_{DEP}$ and the displacement vector $\boldsymbol{\Delta x}$. The former quantity is available from **Figure 4.6**b and the latter from the measurements reported in **Figure 4.3**. This work, which varies by particle as per its location, is plotted in **Figure 4.6**c. The cycle times of the experiments reported in the three panels are 3s, 15s, and 45s, respectively. Like the DEP force itself, $W_{a,i}$ is strong close to the top and bottom of the box and is weak at the center. In addition, the longer the cycling time, the longer the trajectory (or displacement), which also results in greater DEP work. For each operation (representing 1/3 of a cycle time), the average active energy per particle, termed W_a, for these three conditions is 3.1 k_BT, 20.8 k_BT and 39.3 k_BT, respectively. The active energy injected therefore increases with longer operation time.

We hypothesize that annealing is an activated process. A successful annealing requires to overcome a free energy barrier to convert polycrystal to a monocrystal. This can be described by the reaction coordinates as shown by **Figure 4.8**. We find that the DEP work (W_a) correlates with the crystal quality and conditions for complete annealing, as shown in **Figure 4.6**d and e. To perform this analysis, we calculated the active energy at various operating conditions, over the range of τ = 3-45 s, ω = 1-30 kHz and A = 3-7 V. The number of grains plotted in **Figure 4.6**d describes whether the annealing under a specific condition is successful (= 1 grain) or not (>1 grain). We find a rapid change of the value at about W_a = 65 k_BT. Injection of an average active energy per particle greater than this value yields a monocrystal (single grain), while lower active energy injection significantly reduces the chance of full defect removal through grain

boundary annealing. **Figure 4.6**d supports the hypothesis that annealing from a polycrystal to single crystals requires injection of sufficient active energy through the cyclically applied AC electric field.

Figure 4.6e also evaluates the hypothesis is that is what is critical about the operating conditions of amplitude, frequency, and cycle time is the amount of active energy injected into the system on a per particle basis. This figure shows that the measure of quality ψ_6 of the crystal produced under all the operating conditions correlated with the average active energy per particle injected by the cyclic electric field. The data from all the experimental conditions studied collapse well onto a master curve. The overall quality of the finally assembled colloidal crystal displays at maximum at about W_a = 65 k_BT, in agreement with the transition observed in **Figure 4.6**d. The existence of an optimum active energy injected by the cyclic electric field suggest that annealing performance is controlled by multiple factors, a point that we address in the discussion section.

4.4.7 Transition of state for a single particle

Figure 4.6e thus indicates that the global annealing performance correlates with the average active energy per particle injected by the electric field. In this system, annealing progresses by the migration of grain boundaries toward the outside of the crystal, until they are ultimately expelled. The global annealing performance is thus linked to the local grain boundary motion. Inspection of the crystal dynamics indicates that grain boundaries migrate from regions of low active energy to high active energy, as shown in **Figure 4.7**a. **Figure 4.7**a is an overlay image of particles in a colloidal crystal and the DEP energy landscape; a grain boundary is located in regions with varying DEP energy. However, the grain boundary generally moves from a low energy region to higher energy region. The grain boundary motion involves intermittent

dynamics of individual particles. The boundary motion represents a progression of particle states in which each are initially in one crystallite, then transition to be part of the boundary, and finally return back into a crystalline state as part of the neighboring crystallite. This trajectory shown by the relative location of a single particle and grain boundary in **Figure 4.7**b. We observed the grain boundary as it passed through the red particle from 25-110 min.

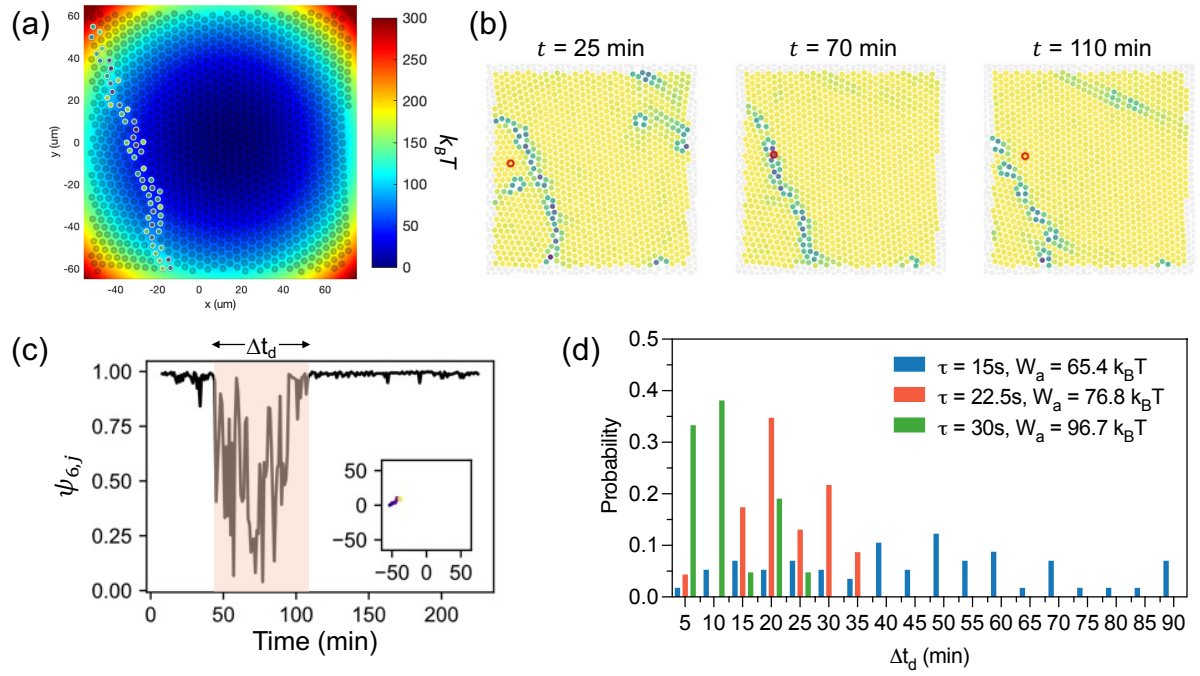


Figure 4.7: Transition state of a local particle. (a) Active energy landscape for one cycle of operation, calculated under conditions of A = 5V_{rms}, ω = 5 kHz and τ = 15s. The points label the location of the particles at 50 min after the cyclic field was initiated. Defect particles in the grain boundary are identified (with the condition $\psi_{6,j} < 0.9$) and indicated in the image with a white border. (b) Track of a single particle (marked by red circle) before, during, and after it moved from one crystal grain to the neighboring grain, at a time of 25 min, 70 min and 110 min, respectively. (c) The $\psi_{6,j}$ of the tracked particle in panel (b) changes over time. The orange shaded area indicates the time in defect state (as per the condition $\psi_{6,j} < 0.9$). The inset of the figure labels the location of the tracked particle over the entire assembly and annealing process. (d) The probability distribution of the time needed for a defect state ($\psi_{6,j} < 0.9$) to transition from one crystal grain to the other, here plotted for three different cycle times/active energies.

We analyzed the intermittent dynamics of this particle by tracking its change in $\psi_{6,j}$ v with time, as presented in **Figure 4.7**c. We observed a rapid change in $\psi_{6,j}$ around 45 min and then again at 107 min. A broad peak with a low $\psi_{6,j}$ value between these two times is indicative

of a defect state. It forms during a time interval when the tracked particle is part of the grain boundary (shaded area in **Figure 4.7**c). We define the time interval a given particle spends in defect state as $\Delta t_{d,j}$ and call it the defect state time. We found this value for all sampled particles by calculating the duration for which $\Delta t_{d,j} < 0.9$, conditioned on that state being held for 5 or more minutes. Additional examples of this $\Delta t_{d,j}$ identification can be found in **Figure 4.9**.

We sampled particles interacting with grain boundaries under several conditions to determine the probability distribution of Δt_d, as reported in **Figure 4.7**d. The trend indicates that higher active energy, such as at the condition of τ = 30s, results in a sharper distribution of Δt_d and a relatively short average Δt_d. On the other hand, lower active energy yields a wider span of Δt_d, as exemplified by the τ = 15s condition. These results suggest that the origins of the global active energy effects on annealing, as observed in **Figure 4.6**e are correlated with the distribution of times that particles spend in the grain boundary defect state, as reported in **Figure 4.7**d. Future work can seek to discover the mechanistic origin of this correlation. Of particular interest would be to test what functional form that defect state time distribution adopts. From the data, candidate functional forms might be a Gaussian or Poisson distribution. Additional sampling under a broader set of active energy injection conditions would facilitate such testing.

4.5 Discussion

In this study, we determined the optimal annealing conditions for a colloidal crystal subjected to a rotating electric field and sought explanations of the findings by investigating the annealing as an activated process. In the following discussion paragraphs, we address the contribution of both DEP and dipolar forces and their effect on annealing performance. In addition, we illustrate how the active energy injection determines the structural evolution of the colloidal crystal during annealing. Finally, we compare the performance of the six-fold design

and its operation with previous studies with different designs and operating conditions, thereby demonstrating the advantage of the annealing method used in this work.

The forces generated by the externally applied AC electric field are induced dipole-induced dipole attractions between closely positioned particles, and the dielectrophoretic force due to the non-uniformity of the electric field. When the electric field is initially applied, the primary force on the particles is dielectrophoretic. Gradients in the electric field drive particles toward the center of the geometry. They there transform from a disordered phase into a crystalline phase. As the particle concentration increases the separation between particles also decreases. The contribution of the dipolar attraction to the total energy therefore increases. Both forces—dipolar and dielectrophoretic—consequently stabilize the self-assembled crystal. However, this pathway for rapid self-assembly also creates non-equilibrium structure with many defects, including grain boundaries. We found that annealing occurs if the cyclic electric field continues to be applied under a particular range of conditions. In this phase of the experiment, the overall shape of the crystal is maintained; however, particles in the crystal undergo periodic cyclic deformation. Because the magnitude and direction of the particle's cyclic motion tracks the strength and direction of the applied field (c.f. **Figure 4.3** and **Figure 4.4**), we conclude that these particle displacements are primarily driven by the dielectrophoretic force generated by the spatially varying electric field.

Based on the physics of activated processes, we hypothesize that there is a free energy barrier in the system that retards the conversion of the polycrystal, with its higher free energy and lower entropy, into a defect free crystal with a lower free energy and higher entropy. The transition from the higher to lower free energy state can be accelerated by the injection of active energy into the system through the cyclic DEP forces. These DEP forces promote the transient

creation of high energy configurations in the system. This exploration of the free energy landscape can intermittently result in configurations that traverse the free energy barrier, thereby accelerating the conversion from the polycrystal to the single crystal state. **Figure 4.6** and **Figure 4.7** present evidence at global and local scales, respectively, for the existence of such activated dynamics. Globally, the polycrystal to single crystal transition proceeds by a process in which grain boundaries are expelled from the crystal. Locally, the grain boundary motion is generated by particles transforming from one crystal state to another by traversing the grain boundary defect state through intermittent dynamics.

According to Equation 4.1, decreasing the frequency or increasing the amplitude of the AC field tends to increase the DEP and dipolar forces. At high frequency conditions, as shown in **Figure 4.4**a (iii), the gentle movement is due to weak DEP forces at ω = 30 kHz. The colloidal crystal in this case reached a steady state structure through field-driven particle displacements that still include polygrains. On the other hand, injection of very large amounts of active energy is also not desired. This situation can generate transient dislocations, observed as a temporarily split and misalignment of a crystal grain. For example, in the case of ω = 1kHz as shown in **Figure 4.4**a (i), particles at the edge remains disordered. This reduces the ψ_6. Thus, there appears to be an optimum active energy that can balances the need for sufficient active energy injection to anneal grain boundaries but still at low enough levels in which transient dislocations are avoided. That is, greater active energy increases the chance of successful annealing because it enhances the local dynamics of particles in the crystal. We observed progressive removal of grain boundaries given sufficient active energy injection. However, Excessive active energy reduces the quality of crystal, as apparent in **Figure 4.6**e. By analysis of this kind, we found when the active energy injection (as quantified by the DEP work) was $W_a < 65\ k_B T$, then most

defects were located in unresolved grain boundaries. On the other hand, the defects appear when $W_a > 65\ k_BT$ are mostly dislocations and some locally disordered packing. This can be seen in **Figure 4.10**, where we show examples of high and low active energy regimes.

The multiple-electrode device generates a temporally and spatially varying dielectrophoretic (DEP) energy landscape, enabling the crystal to deform globally. Similarly, Zhang *et al.* utilized two pairs of operating electrodes and two pairs of grounded electrodes to create an anisotropic energy landscape, incorporating a feedback control loop to regulate field parameters[164]. In contrast, the six-fold device used in this work introduces an additional directional operation, allowing for local movement along a triangular trajectory. The cyclic field, operating at a constant time interval, also eliminates the need for external control. Finally, the optimized conditions enable defect removal without melting the crystal, making this method particularly applicable to systems with low phase change tolerance.

4.6 Conclusions

This work demonstrates the feasibility of using a six-fold electric field to anneal the defects incorporated into a colloidal crystal during self-assembly. We characterized and analyzed the annealing process—which consisted of a rotating AC electric field—by measuring the time-dependent positions of particles in the crystal with confocal microscopy. We compared the performance of annealing over a range of operating conditions, including the AC field amplitude, frequency, and cycling period. The annealing performance was specifically assessed by measuring the final number of crystalline clusters and the global average value of the hexatic order parameter ψ_6. We hypothesized that the annealing displays features of an activated process. The activation energy here is taken as the energy injected into the system by the cyclically applied electric field. This injection yields particle displacements due to the effect of

the dielectrophoretic force, which was computed for the electrode geometry used for self-assembly and annealing. A critical active energy of about 65 k_BT averaged for each cycle was discovered to be the minimum energy injection needed to yield full annealing, here defined as self-assembly of a single grain crystal. We also found that ψ_6 of this final colloidal crystal was also optimized at 65 k_BT; this suggests that there is an optimum value of the active energy that should be input into the system for best annealing. We explored the effect of the injected active energy on the local dynamics of particles in the vicinity of a grain boundary and found evidence of an intermittent dynamics consistent with the existence of an activated process. This work therefore identifies an annealing strategy, finds its optimum operation, and proposes a mechanism for its performance in ways that are broadly relevant to the fundamental understanding of defect dynamics in colloidal crystals, and the practical processing of these materials for their use as functional materials.

4.7 Supplementary Information

Table 4.1: Parameters used for force calculations at different field frequencies. $\mathrm{Re}|\mathrm{CM}(\omega)|$ was determined by *Mittal et al.* by assuming that its value is log-linear between 1 kHz to 30 kHz following the equation $\mathrm{Re}|\mathrm{CM}(\omega)| = -0.39 \log \omega + 2$.

Frequency (kHz)	ϵ_r of solution	$\mathrm{Re}\lvert\mathrm{CM}(\omega)\rvert$
1	78.4	0.83
3	78.4	0.64
5	78.4	0.56
10	78.4	0.44
30	78.4	0.25

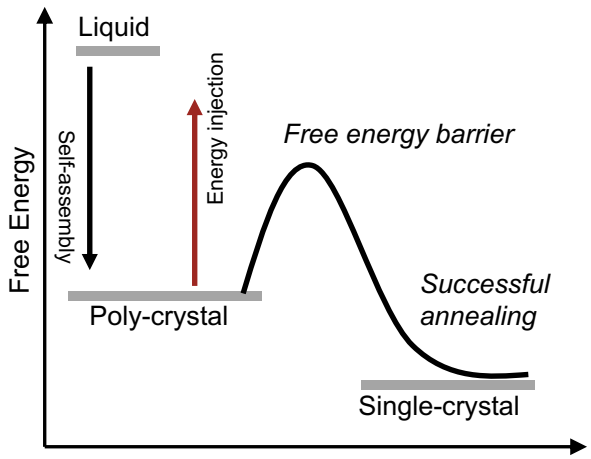


Figure 4.8: Reaction coordinates of self-assembly and annealing process. This diagram illustrates the hypothesized annealing mechanism by activated process.

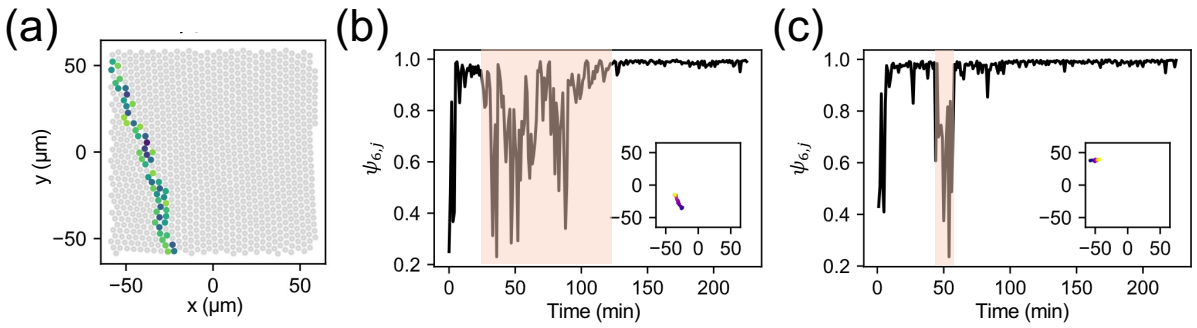


Figure 4.9: Characterization of time of a single particle in defect state. (a) Defects in colloidal crystals at the condition of A = 5V_{rms}, ω = 5 kHz and τ = 15s, at 50 min after the field was turned on. Particles are colored based on the local ψ_6 values to identify the grain boundary. (b)-(c) Additional example particles located at the grain boundary as shown in panel (a). The local ψ_6 for two particles is plotted as a function of time. Shaded areas correspond to the time needed for the particle to traverse the defect state (Δt_d). The inset figure plots the location of the particle through the entire process.

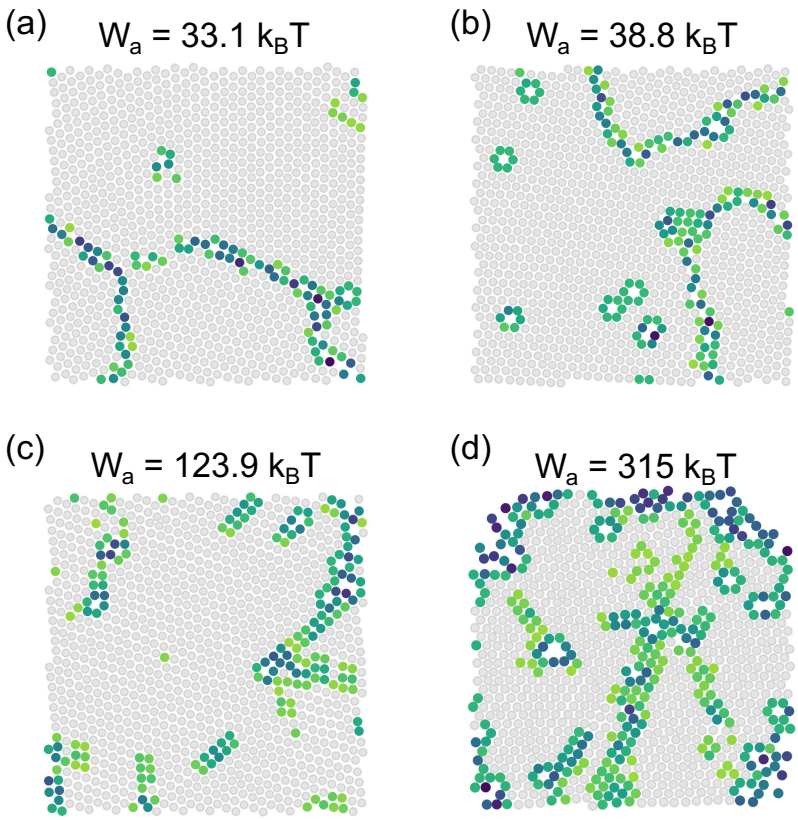


Figure 4.10: Defect structures at conditions of various active energy input. (a)-(b) At these low active energy levels, defects are primarily present as unresolved grain boundaries. (c)-(d) At these high active energy levels, defects are primarily observed as transient dislocations. Defect particles colored as per their non-crystalline $\psi_{6,j}$.

Chapter 5 Conclusions

5.1 Summary of research

In this dissertation, we investigated the relationship between tunable microstructure in colloidal crystals and their structural color properties. We demonstrated the feasibility of engineering the microstructure by varying the pair interactions and electric field conditions. We found that structural color properties could be precisely tailored by adjusting the particle size, crystal dimensions, and defect abundancy. Furthermore, we developed an open-loop process that enabled the annealing of defects in a colloidal crystal, and thereby to improving its crystal quality.

Chapter 2 presented our findings about the generation of prismatic structural color from thin layers of colloidal crystal made of microparticle colloids (size ~1 μm), a size range that is less commonly associated with structural color, as most of the structural colors are produced by building blocks with length scale of 0.1-0.3 μm. We hypothesized and explained this phenomenon as the consequence of a grating diffraction effect. Specifically, we characterized the grating diffraction structural color by optical spectroscopy and color analysis. Then, by studying the effect of particle size and number of crystalline layers on the color performance, including the angular variation of the spectrum, hue, and saturation, we found that the functional dependencies of these quantities were described the grating diffraction theory. In addition to the experimental work, we developed a model based on Mie scattering theory, which integrated the form factor of a single colloidal sphere and the static structure factor of an FCC crystal structure.

The model fully predicted the structural color spectral response for micron and submicron colloids. We extended this calculation to different particle diameters and crystal layer thicknesses, resulting in an operating diagram that bridged two optical regimes: grating diffraction and Bragg's reflection. We observed excellent agreement between the measured structural color peaks, diffraction theory, and the scattering model. This work demonstrates that structural color is closely linked to both the particle dimensions and the self-assembled structure, making it useful for applications in sensors and coatings. It also showed the relationship between microparticle crystal structural and the structural color optical spectrum, a relationship that was exploited in the second part of the project.

Self-assembled colloids usually contain defects that may also affect functional properties such as structural color. In Chapter 3, we probed an approach to manipulate the self-assembly kinetics and defect formation mechanism and investigated the impact of these defects on structural color. We discovered two important factors that affect the mechanism of electrophoretic deposition and assembly, (1) the solution salt concentration and (2) the applied electric current density. These parameters control the pair potential, deposition velocity, and electrohydrodynamic forces. As a result, the self-assembled colloidal polycrystals exhibit various defect structures and grain number density. We constructed a complete state diagram illustrating the transition from dense liquid to colloidal crystals of varying quality, and finally to a disordered adsorbed state. In addition, we found the overall quality of the colloidal crystal (as measured by the average hexatic order parameter of the system, ψ_6) can influence the grating diffraction structural color performance. Specifically, we found the color intensity increaseed with ψ_6 about 10 times faster after ψ_6 exceeded 0.87, representing a turning point. In addition, MD and FDTD simulation further demonstrated that the azimuthal uniformity of the coloration

depends on the number of grains and their varying alignment relative to each other. We observed a trade-off between color intensity and the azimuthal uniformity, suggesting that defect engineering can enhance the performance of colloidal crystals for real-world applications.

However, defects are generally undesired for most of applications. In Chapter 4, we explored the use of a rotating AC electric field to resolve defects in 2D colloidal crystals. We designed a 6-fold electrode device that allowed the dipolar force to be multidirectional and rotationally applied to the colloidal crystal. The first part of the chapter focuses on optimizing the annealing performance by varying the electric field conditions, including the amplitude, frequency and cycling period. The second part delves into the fundamental mechanism of local and global annealing observed under these conditions. Performing particle tracking and force calculations allowed us to estimate the active energy injected by the field during each cycle. We hypothesized that the annealing occurs as an activated process and performed testing to explore this mechanism, which posits that a sufficient level of activation energy is required to drive particles to the lower free energy state that resolves defects. The accumulative effect of these local rearrangement results in successful global annealing.

5.2 Outlook and future directions

5.2.1 Further improvement of grating diffraction efficiency

In Chapter 2 and 3, we obtained structural color by grating diffraction with a diffraction efficiency less than 5%. A more energy sustainable way to produce coloration would involve improving the diffraction efficiency. This work suggests two avenues that could be pursued through future research to improve the diffraction efficiency:

The first method would be to vary the shape of the grating, which could be accomplished by a change of particle geometry. This method would require special fabrication of the

microparticles and the design of controllable ways for their self-assembly[169]. Specifically, particles with designed shape and surface chemistry can be synthesized using photolithography[170] or thermoplastic deformation[20,171]. For example, it is possible to assemble tetrahedral colloids into a 2D surface to form a blazed grating. In addition, the grating orientation is also designable with various geometries of the building block.

The second approach would be through increasing the refractive index contrast between particle and solution. A higher refractive index would result in a stronger diffraction intensity based on our Mie scattering modeling and FDTD simulation. For example, replacing solid particle by hollow spheres[172] can improve the refractive index contrast from 1.08 (DMSO/PS) to 1.48 (DMSO/Air). FDTD could be simply implemented to predict the spectral response for various geometries and dielectric properties of the material. This would open many possibilities for applications of this grating diffraction structural color.

5.2.2 Reversibility and durability in reconfigurable electrophoretic deposition

Our use of the electrophoretic deposition method in the dissertation offers a reversible way of assembling colloidal crystals. However, real applications also require long-term durability. The electrochemical reaction accomplished in the DC field cell that induced electrophoresis is primarily due to surfactants and water in DMSO, which may be depleted over a long time of operation because of the electrochemistry. Future research could explore adding different electrochemical reactants or using alternative electrolytes to optimize performance and extend operational lifetime.

In Chapter 3, we analyzed the microstructure of self-assembled polycrystals after a single DC field operation. Because of this approach, the practical reversibility of the polycrystal structure is more hypothesized than known. Parameters whose reversibility could be assessed are

ψ_6 and the number of grains in the crystal. Future researchers could use reversible cycling, akin to cyclic voltammetry, to create time dependent colloidal structures and characterize their properties after each cycle. This test would be useful to understand structural color properties, especially the stability across multiple cycles of field operation.

5.2.3 Categorizing defects using machine learning-aided image analysis

Defects presented in 2D and 3D colloidal crystals can be categorized based on their geometry and local environment. In this dissertation, we primarily characterized the defects by calculating the real and imaginary parts of ψ_6, performing cluster analysis to identify grains and grain boundaries, and using Voronoi analysis. Further analysis of the microscopy images could help identify additional, fruitful information about the defect structures. We propose that future work could leverage machine learning to classify defects in colloidal crystals in more efficiently and in new ways, similar as described in previous studies[173,174]. For example, supervised learning models could be trained on microscopy images labeled with defect types such as grain boundaries, point defects, and dislocations. By incorporating additional features like particle locations and nearest neighbor data, the accuracy of the classification could be further improved. This would help to correlate defect types with their impact on optical properties, enabling more precise control over the material's performance.

5.2.4 Effect of field symmetry on the annealing of defects in spheroid colloidal crystals

We developed a 6-fold device with a 60-degree phase angle, the symmetry of which is consistent with the fundamental lattice symmetry of crystals self-assembled from isotropic spheres. More research could be conducted on the effect of field geometry on annealing performance. This may involve changes to the number of electrodes, the orientation of each electrode, and the operation sequence of the applied field. For example, asymmetric changes in

the field direction of the applied dipolar interaction would be of interest; such an approach might be helpful to anneal grain boundaries with particular misalignment angles. In addition, the number of directional operations and its operation sequence may affect the local motions and trajectories of particles in the crystal, resulting in differences in the overall annealing performance.

Adopting these ideas for research on annealing of colloidal crystal with non-spherical shape would also be particularly valuable. For example, in a way that differs from spheres, the contact angle for a close-packed array of colloidal ellipsoids depends on the particle aspect ratio[175]. Moreover, colloidal ellipsoids have higher rotational degrees of freedom. A stronger dipolar force could algin the long axis of the particles with the field direction[43,176]. Therefore, more opportunities to design the geometry of the device for optimal annealing of non-spherical particles might be available.

Appendices

Appendix A: Computer Code

This appendix section contains the core computer codes developed for this dissertation research, including scattering modeling, image analysis, data manipulation, and FDTD calculation.

A.1 Scattering modeling algorithm

The scattering modeling uses Mie scattering code adapted from Prof. Michael Solomon's CHE 696, 2003 notes, and the static structure factor for FCC crystal.

A.1.1 Mie scattering algorithm (MATLAB)

```
function [solution, Cscat, bracketcostheta] = Miescattering_modver1(m, a_p,
lambda, anglimit, n_angles)

% magnitude of the incident wave vector, k_i.
k_i = 2*pi/lambda;

% dimensionless parameters used in the calculation of a_n and b_n
alpha = k_i*a_p;
beta = m*alpha;

% n_c is the number of terms to be taken in the summation of terms containing
the scattering coefficients.
% This expression is recommended by Barber and Hill in Light Scattering my
Particles: Computational Methods, 1990.
% You can modify this expression to complete homework problem #3.
n_c = round(alpha + 4.05*alpha^0.3333 + 2);

% If n_c > 250 the code won't work.  Thus, set n_c to 250 and continue.  So,
if n_c = 250 is output on the screen,
% The computed scattered is not expected to be valid.
if n_c > 250
    n_c = 250
end;
% n_c
```

```
% n-angles is the number of angles the scattering will be computed at.  As
n_angles increases, the angular
% resolution will improve; however, the code will take longer to run.  This
parameter is user modifiable.

% The parameter maxtheta sets the angular range of computation.  The default
is maxtheta = 1; then the angular range
% is from 0 to 0.95*pi (a little less than 180¬°).  For example, to perform a
calculation where theta varies from
% 0 to a little less than 90¬°, choose maxthetafactor = 2.  This parameter
will be changed by the user to complete problem #2.

maxthetafactor = 180/anglimit;
%maxthetafactor = 1;

fudge = 0.999;

% In this section a number of arrays are loaded that set the range of values
which will be calculated.
for k = 1:n_angles;
    q(k) = 2*k_i*sin(fudge*pi/maxthetafactor*k/n_angles/2);
    theta(k) = fudge*pi*k/n_angles/maxthetafactor;
    thetadeg(k) = theta(k)*180/pi;
    costheta(k) = cos(fudge*pi/maxthetafactor*k/n_angles);
    sintheta(k) = sin(fudge*pi/maxthetafactor*k/n_angles);
    aq(k) = a_p*q(k);
end;


% In this section the functions pi_n and tau_n are computed by means of a
Matlab function that computes
% Legendre polynomials.  Derivatives of Legendre functions are computed by
recrusion relations from Kerker,
% The scattering of light, 1969.  It isn't necessary to modify this section
to complete the homework.
for i = 1:n_c;
    P = legendre(i,costheta);
    pi_n(i,:) = P(2,:);
    for k = 1:n_angles
        pi_n(i,k) = -pi_n(i,k)/sintheta(k);
        if i == 1
            pi_n_prime(i,k) = 0;
            tau_n(i,k) = costheta(k)*pi_n(i,k);
        elseif i == 2
            pi_n_prime(i,k) = 3;
            tau_n(i,k) = costheta(k)*pi_n(i,k)-(sintheta(k))^2*(2*i-1);
        else
            pi_n_prime(i,k) = (2*i-1)*pi_n(i-1,k) + pi_n_prime(i-2,k);
            tau_n(i,k) = costheta(k)*pi_n(i,k)-
(sintheta(k))^2*pi_n_prime(i,k);
        end;
    end;
end;

tau_n;
pi_n(1,:);
```

```
% In the following lines (approximately seventy) the scattering coefficients
a_n and b_n
% are computed.  They are a function of the dimensionless parameters alpha
and beta.  They are
% computed by calling Bessel function routines, and by means of recursion
relations from Kerker,
% The scattering of light, 1969.  There is no need to modify this section to
complete the homework.
y(1) = alpha;
y(2) = beta;
y;
y = y.';

for i = 1:n_c;
    x(i) = i + 0.5;
end;

psi(1,:) = besselj(x,y(1));
psi(2,:)= besselj(x,y(2));
psi(1,:) = (pi*y(1)/2)^0.5*psi(1,:);
psi(2,:) = (pi*y(2)/2)^0.5*psi(2,:);

chi(1,:) = bessely(x,y(1));
chi(2,:)=bessely(x,y(2));
chi(1,:) = -(pi*y(1)/2)^0.5*chi(1,:);
chi(2,:) = -(pi*y(2)/2)^0.5*chi(2,:);

zeta = psi + j*chi;

psilow(1,:) = besselj(0.5,y(1));
psilow(2,:)=besselj(0.5,y(2));
psilow(1,:) = (pi*y(1)/2)^0.5*psilow(1,:);
psilow(2,:) = (pi*y(2)/2)^0.5*psilow(2,:);

chilow(1,:) = bessely(0.5,y(1));
chilow(2,:)= bessely(0.5,y(2));
chilow(1,:) = -(pi*y(1)/2)^0.5*chilow(1,:);
chilow(2,:) = -(pi*y(2)/2)^0.5*chilow(2,:);

zetalow = psilow + j*chilow;

n_high = n_c + 1.5;

psihigh(1,:) = besselj(n_high,y(1));
psihigh(2,:)=besselj(n_high,y(2));
psihigh(1,:) = (pi*y(1)/2)^0.5*psihigh(1,:);
psihigh(2,:) = (pi*y(2)/2)^0.5*psihigh(2,:);

chihigh(1,:) = bessely(n_high,y(1));
chihigh(2,:) = bessely(n_high,y(2));
chihigh(1,:) = -(pi*y(1)/2)^0.5*chihigh(1,:);
chihigh(2,:) = -(pi*y(2)/2)^0.5*chihigh(2,:);

zetahigh = psihigh + j*chihigh;

for i = 1:n_c
```

```
    if i == 1
        psiprime(1,i) = 0.5*psilow(1,1) - 0.5*psi(1,i+1) + psi(1,i)/2/y(1);
        psiprime(2,i) = 0.5*psilow(2,1) - 0.5*psi(2,i+1) + psi(2,i)/2/y(2);
        zetaprime(1,i) = 0.5*zetalow(1,1) - 0.5*zeta(1,i+1) +
zeta(1,i)/2/y(1);
        zetaprime(2,i) = 0.5*zetalow(2,1) - 0.5*zeta(2,i+1) +
zeta(2,i)/2/y(2);
    elseif i == n_c
        psiprime(1,i) = 0.5*psi(1,i-1) - 0.5*psihigh(1,1) + psi(1,i)/2/y(1);
        psiprime(2,i) = 0.5*psi(2,i-1) - 0.5*psihigh(2,1) + psi(2,i)/2/y(2);
        zetaprime(1,i) = 0.5*zeta(1,i-1) - 0.5*zetahigh(1,1) +
zeta(1,i)/2/y(1);
        zetaprime(2,i) = 0.5*zeta(2,i-1) - 0.5*zetahigh(2,1) +
zeta(2,i)/2/y(2);
    else
        psiprime(1,i) = 0.5*psi(1,i-1) - 0.5*psi(1,i+1) + psi(1,i)/2/y(1);
        psiprime(2,i) = 0.5*psi(2,i-1) - 0.5*psi(2,i+1) + psi(2,i)/2/y(2);
        zetaprime(1,i) = 0.5*zeta(1,i-1) - 0.5*zeta(1,i+1) +
zeta(1,i)/2/y(1);
        zetaprime(2,i) = 0.5*zeta(2,i-1) - 0.5*zeta(2,i+1) +
zeta(2,i)/2/y(2);
    end;
end;

for i = 1:n_c
    a(i) =(psiprime(2,i)*psi(1,i) -
m*psi(2,i)*psiprime(1,i))/(psiprime(2,i)*zeta(1,i) -
m*psi(2,i)*zetaprime(1,i));
    b(i) =(m*psiprime(2,i)*psi(1,i) -
psi(2,i)*psiprime(1,i))/(m*psiprime(2,i)*zeta(1,i) -
psi(2,i)*zetaprime(1,i));
end;

% In this section S1(theta), S2(theta), i_1(theta) and i_2(theta) are
computed
% by summing the coefficients a_n and b_n from 1 to n_c.
for k = 1:n_angles
    S_1(k) = 0;
    S_2(k) = 0;
    for i = 1:n_c
        S_1(k) = S_1(k) + (2*i+1)/i/(i+1)*(a(i)*pi_n(i,k) + b(i)*tau_n(i,k));
        S_2(k) = S_2(k) + (2*i+1)/i/(i+1)*(a(i)*tau_n(i,k) + b(i)*pi_n(i,k));
    end;
    i_1(k) = S_1(k) * conj(S_1(k));
    i_2(k) = S_2(k) * conj(S_2(k));
end;

% In this section the scattering cross section is computed by means of the
expression
% in van de Hulst, pg 128.

Qscat = 0;
bracketcostheta = 0;
for i = 1:n_c
    Qscat = Qscat + (2*i+1)*(a(i)*conj(a(i))+b(i)*conj(b(i)));
end
```

```
for i = 1:n_c-1
bracketcostheta = bracketcostheta +
i*(i+2)/(i+1)*real(a(i)*conj(a(i+1))+b(i)*conj(b(i+1))) + ...
                                    (2*i+1)/i/(i+1)*real(a(i)*conj(b(i)));
end

Qscat = Qscat*2/alpha^2;
Cscat = Qscat*3.14158*a_p^2;
bracketcostheta = bracketcostheta*4/alpha^2/Qscat;

% In this section the Rayleigh Debye scattering for a sphere is computed for
the same input parameters
% used in the above Mie theory calculation.  This section was used in
development of the code for error checking.
% You can use these results to learn about the differences in Rayleigh Debye
and Mie scattering if you would like.
V = 4/3*pi*a_p^3;
for z = 1:n_angles
    Rayleighi_1(z) = k_i^6*V^2*((m-1)/2/pi)^2*(3/(aq(z))^3*(sin(aq(z))-
aq(z)*cos(aq(z))))^2;
    Rayleighi_2(z) = (costheta(z))^2*k_i^6*V^2*((m-
1)/2/pi)^2*(3/(aq(z))^3*(sin(aq(z))-aq(z)*cos(aq(z))))^2;
end;

% The remainder of the code contains various options for output.  All of the
output options besides figure(2)
% have currently been disabled by inserting a "%" before each command line.
If you would like to make use of
% a disabled output command, simply remove the "%".  Feel free to modify this
part of the code to generate output
% in any format you would like.
% Figures 1-4 plot some of the code output versus parameters like theta and
aq.

%figure(1)
%semilogy(aq,i_1,aq,i_2)

%figure(2)
%semilogy(thetadeg,i_1,thetadeg,i_2)

%figure(3)
%semilogy(aq,i_1,aq,i_2,aq,Rayleighi_1,aq,Rayleighi_2)

%figure(4)
%semilogy(thetadeg,i_1,thetadeg,i_2, thetadeg,
Rayleighi_1,thetadeg,Rayleighi_2)

% The matrix "solution" contains a summary of all output of the code suitable
for cutting
% and pasting into your favorite spreadsheet or plotting program.  It is
currently disabled by means of a "%" in line 217.

i_1 = i_1.';
i_2 = i_2.';

S_1 = S_1.';
```

```
S_2 = S_2.';

thetadeg = thetadeg.';
aq = aq.';
Rayleighi_1 = Rayleighi_1.';
Rayleighi_2 = Rayleighi_2.';

solution(:,1) = i_1;
solution(:,2) = i_2;
solution(:,3) = thetadeg;
solution(:,4) = aq;
solution(:,5) = Rayleighi_1;
solution(:,6) = Rayleighi_2;
solution(:,7) = S_1;
solution(:,8) = S_2;

% filenameout = sprintf('Miesolution');
% save(filenameout, 'solution', '-ascii');

end
```

A.1.2 Calculation of structure factor of crystal lattice using Euler's method (MATLAB)

```
function S = sf_fcc(uo,us,n_m,lambda,N,a_p,lattice)
ko_ = uo*2*pi*n_m/lambda;
ks_ = us*2*pi*n_m/lambda;
q_ = ks_-ko_;
expsum = 0;
for j = 1:N
    expsum = expsum+cos(dot(q_,lattice(j,:)));
end
sqrdsum = expsum^2;
S2 = 1/N*sqrdsum;
end
```

A.1.3 Calculation of structure factor of amorphous structure (MATLAB)

```
S = Sfactor_amorphous(phi,aq, a_p, n_angles)
% compute structure factor
S = ones(n_angles,1);
c = zeros(n_angles,1);

l1 = -1*(1+2*phi)^2/(1-phi)^4;
l2 = 6*phi*(1+0.5*phi)^2/(1-phi)^4;
l3 = 0.5*phi*l1;

d = 2*a_p;
rho = phi/4*3/3.14159/a_p^3;

qd = aq*2;

c(1:n_angles) = d^3*3.14159*4*((qd.^-2*-1*(l1+l2+l3)+qd.^-4*(2*l2+12*l3)-
qd.^-6*24*l3).*cos(qd(1:n_angles)) + ...
```

```
                                (qd.^-3*(l1+2*l2+4*l3)-qd.^-
5*24*l3).*sin(qd(1:n_angles)) - qd.^-4*2*l2 + qd.^-6*24*l3);

S(1:n_angles) = 1 + c(1:n_angles)*rho./(1-c(1:n_angles)*rho);
```

A.1.4 Build FCC crystal lattice with cylinder shape (MATLAB)

```
function onelatt = original_single_layer_lattice(d,num)
a1 = [d/2,sqrt(3)/2*d,0];
a2 = [d/2,-sqrt(3)/2*d,0];
halfn = (num-1)/2;
int_ = -halfn:1:halfn;
latt0 = [];
for i = 1:num
    for j = 1:num
        P = int_(i)*a1+int_(j)*a2;
        latt0 = [latt0;P];
    end
end
onelatt = latt0;
end

function latt = fcc_crystal_lattice(latt0,d,M,rot_phi)
d111 = (sqrt(2)/sqrt(3))*d;
latt = [];
if mod(M,2) == 0
    z = (-M/2+1):1:M/2;
else
    z = (-(M-1)/2):1:((M-1)/2);
end

for j = 1:M
    if mod(z(j),3) == 0
        lattj = latt0 + [0,0,z(j)*d111];
    elseif mod(z(j),3) == 2
        lattj = latt0 + [0,0,z(j)*d111] + [0,d/sqrt(3),0];
    else
        lattj = latt0 + [0,0,z(j)*d111] + [d/2,d/(2*sqrt(3)),0];
    end

%scatter3(lattj(:,1),lattj(:,2),lattj(:,3),1000,'MarkerFaceColor',rand(3,1));
    %hold on
    latt = [latt;lattj];
end
rot_deg = rot_phi*pi/180;
Rz = [cos(rot_deg),-sin(rot_deg),0;sin(rot_deg),cos(rot_deg),0;0,0,1];
latt = transpose(Rz*transpose(latt));
end

function circlatt = fcc_circle_lattice(latt0,d,num)
circlatt = [];
halfn = (num-1)/2;
rmax = d*halfn*sqrt(3)/2+1;
for i = 1:length(latt0)
    r = sqrt(latt0(i,1)^2+latt0(i,2)^2);
    if r <= rmax
```

```
        circlatt = [circlatt;latt0(i,:)];
    end
end
end
```

A.1.5 Calculation of form factor and scattering intensity (MATLAB)

```
function [F,aq] = ff(m, a_p, lambda, theta,r_detc)
solution = Miescattering_modver1(m, a_p, lambda, theta, 1);
S1 = solution(7);
S2 = solution(8);
aq = solution(4);
kvector = 2*pi*m/lambda;
F =
(1/(kvector^2*(r_detc^2)))*((1/2)*(real(S1)^2+imag(S1)^2+real(S2)^2+imag(S2)^
2));
end

%%%%%%%%%% INPUT MATERIAL PARAMETERS %%%%%%%%%%%%%%%%%%%%%%%%%%%%%%%%%%%%
d_p = [950]; % particle diameter (nm)
M = 1; % number of layers
num = 13; % must be odd number! number of particles one side each layer
lambda = 400:1:900; % nm
phi = pi/(3*sqrt(2)); % particle volume fraction for perfect FCC is
pi/(3*sqrt(2))
n_p = 1.59; % particle refractive index
n_solv = 1.48; % medium refractive index; air 1; water 1.33; DMSO 1.48
n_air = 1;
n_glass = 1.5;

mr = sqrt(phi(1)*n_p^2+(1-phi(1))*n_solv^2);
a_p = d_p/2;
m = n_p/n_solv;

%%%%%%%%%% INPUT LIGHT PARAMETERS %%%%%%%%%%%%%%%%%%%%%%%%%%%%%%%%%%%%%%%
% define unit vector k
% for 1,1,0 plane ko = [0,0,-1]
% for 1,1,1 plane (closed packed plane)
theta_in = 0; % degree
theta_out = 25:5:60;
rotation = 1:1:30; % degree
in = pi*theta_in/180; out = pi*theta_out/180; % conv. deg. to rad.

for i = 1:length(theta_in)
    if abs(theta_in(i))<=90
        uo(i,:) = [sin(in(i)),0,sqrt(l^2-(sin(in(i)))^2)]/l; % incident light
(unit vector)
    else
        uo(i,:) = [sin(in(i)),0,-sqrt(l^2-(sin(in(i)))^2)]/l; % incident
light (unit vector)
    end
end

for i = 1:length(theta_out)
    if abs(theta_out(i))<=90
        us(i,:) = [sin(out(i)),0,sqrt(l^2-(sin(out(i)))^2)]/l;
```

```
    else
        us(i,:) = [sin(out(i)),0,-sqrt(l^2-(sin(out(i)))^2)]/l;
    end
    s(i) = acos(dot(uo,us(i,:)));

end
theta_s = 180*s./pi;
lambda_solv = lambda/l;
%%%%%%%%%%%%%% LATTICE %%%%%%%%%%%%%%%%%%%%%%%%%%%%%%%%%%%%%%%%%%%%%%%%
d = (1/sqrt(2))*(16/3*pi*a_p^3/phi(1))^(1/3); % the shortest distance between
two particles: larger than particle diameter if phi <0.74

for z = 1:length(rotation)
    lattice = fcc_crystal_lattice(circlatt0,d,M,rotation(z));
    N_lattice = length(lattice(:,1)); %number of particles
    for y = 1:length(theta_s)
        angle3d(y,1:length(lambda)) = theta_out(y);
        for x = 1:length(lambda)
            [Form(y,x),aq(y,x)] = ff(m, a_p(1)/1000, lambda_solv(x)/1000,
theta_s(y),r_detc);
            Structure_c(y,x) =
sf_fcc2(uo,us(y,:),n_solv,lambda(x),N_lattice,a_p(1),lattice);
            Intensity(y,x) = N_p*Form(y,x)*Structure_c(y,x)*ang_inc;
        end
    end
    sum_I = sum_I + Intensity;
end
avg_I = sum_I/length(rotation);
```

A.2 Confocal image analysis

This section includes computer program written to analyze the confocal captured images to extract the structural information, such as particle locations, order parameters, radial distribution functions, crystalline clusters numbers, Voronoi analysis, etc. Illustrative output figures were provided to clarify and guide the flow of the code.

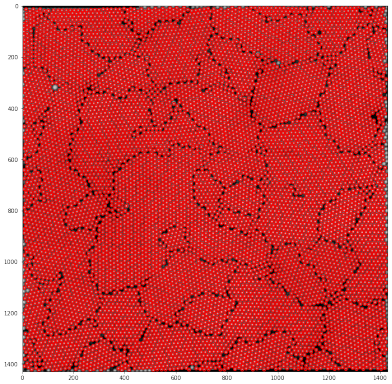
A.2.1 Particle tracking by Trackpy (Python 3)

```
im = Image.open("/Users/xx.jpg")
print (im.size)
micron_per_pixel = 118.24/1900
feature_diameter = 0.95 # um
radius = int(np.round(feature_diameter/2/micron_per_pixel))
if radius % 1 == 0:
    radius += 1
print('Using a radius of {:d} px'.format(radius))

mpl.rc('image', cmap='gray')
frames = np.array(im)
frames = rgb2gray(frames)

f = tp.locate(frames,11)
```

```
plt.figure(figsize=(12,12))  # make a new figure
tp.annotate(f, frames, plot_style={'markersize': 5})
[out]:
```



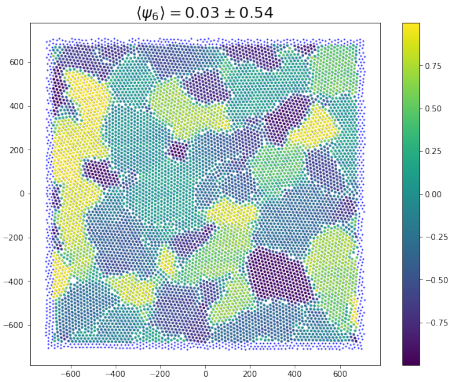
A.2.2 Crystal grain analysis (Python 3)

This part of code is produced by Chih-Mei Young and modified by Tianyu Liu.

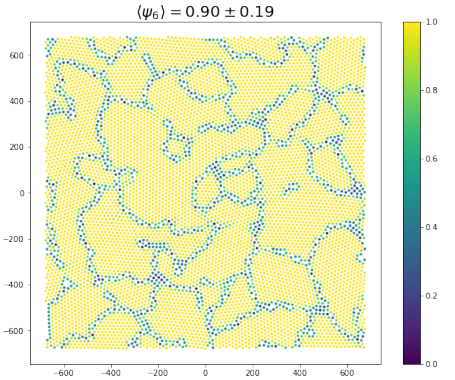
```
f_post_size = f[["x", "y","size"]]
f_np = np.array(f_post_size)
Lx = 1.1*(np.amax(f_np[:,0]) - np.amin(f_np[:,0]))
Ly = 1.1*(np.amax(f_np[:,1]) - np.amin(f_np[:,1]))
Lz = 0
B0 = np.array([im.size[0]/2,im.size[1]/2,0])#f_np.mean(axis=0)
positions = np.copy(f_np)
positions = positions - B0
positions[:,2] = 0
edge_buffer = 10*f_np[:,2].mean()

cond = ((positions[:,0]-np.amax(positions[:,0])+edge_buffer<0)*
        (positions[:,0]+np.amax(positions[:,0])-edge_buffer>0)*
        (positions[:,1]-np.amax(positions[:,1])+edge_buffer<0)*
        (positions[:,1]+np.amax(positions[:,1])-edge_buffer>0))
fbox = freud.box.Box(Lx=Lx,Ly=Ly,Lz=Lz, is2D=True)
psi_woE = freud.order.Hexatic(k=6)
psi_woE.compute((fbox,positions), neighbors={"num_neighbors": 6})
psi6_woE_ImagValues = np.imag(psi_woE.particle_order)
psi6_woE_AbsValues = np.abs(psi_woE.particle_order)
psi6_woE_Angles = np.angle(psi_woE.particle_order)

# imaginary value -> orientation
fig = plt.figure(figsize=(10,8))
plt.scatter(positions[:,0], positions[:,1], s=1, c='b')
plt.scatter(positions[cond,0], positions[cond,1], s=5,
c=psi6_woE_ImagValues[cond], cmap = 'viridis')
plt.title(r'$\langle\psi_6\rangle={p:.2f}\pm{pp:.2f}$'.format(p=psi6_woE_Imag
Values[cond].mean(),pp=psi6_woE_ImagValues[cond].std()), fontsize=20)
plt.colorbar()
[out]:
```




```
# absolute value -> close to hexatic packing
fig = plt.figure(figsize=(10,8))
#plt.scatter(positions[:,0], positions[:,1], s=1, c='b')
plt.scatter(positions[cond,0], positions[cond,1], s=5,
c=psi6_woE_AbsValues[cond], cmap = 'viridis',vmin=0,vmax=1)
plt.title(r'$\langle\psi_6\rangle={p:.2f}\pm{pp:.2f}$'.format(p=psi6_woE_AbsV
alues[cond].mean(),pp=psi6_woE_AbsValues[cond].std()), fontsize=20)
plt.colorbar()
[out]:
```

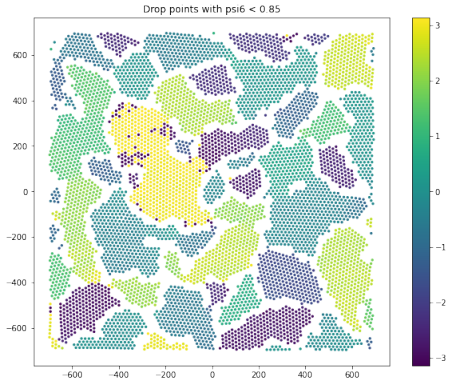



```
#combine imaginary value, absolute value and position
img = pd.DataFrame(psi6_woE_Angles, columns = ['Ang'])
abs = pd.DataFrame(psi6_woE_AbsValues, columns = ['R'])
f_post = f[["x", "y"]]
f_post_img = f_post.join(img)
f_post_img_abs = f_post_img.join(abs)

# drop abs value <= 0.85
f_post_drop = f_post_img_abs[f_post_img_abs['R'] >= 0.85]
f_drop_abs = f_post_drop[["R"]]
f_abs = np.array(f_drop_abs)
f_drop_img = f_post_drop[["Ang"]]
f_img = np.array(f_drop_img)
f_post_drop_xyI = f_post_drop.drop(columns=["R"])
f_post_drop_xy = f_post_drop_xyI.drop(columns=["Ang"])
drop_abs_x = f_post_drop[["x"]]-B0[0]
drop_abs_y = f_post_drop[["y"]]-B0[1]
drop_abs_xy = f_post_drop[["x","y"]]

fig = plt.figure(figsize=(10,8))
plt.scatter(drop_abs_x, drop_abs_y, s=5, c=f_img, cmap = 'viridis')
plt.title("Drop points with psi6 < 0.85")
```

```
plt.colorbar()
[out]:
```

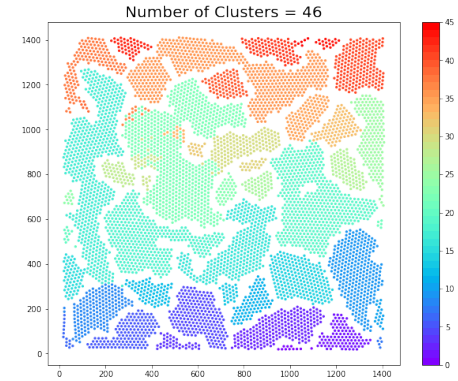



```
clus_ornt = StandardScaler().fit_transform(f_post_drop_xyI) #don't use scaler
#just use in img part
db = DBSCAN(eps=0.15, min_samples=5).fit(clus_ornt,[f_img])
labels = db.labels_
clus = pd.DataFrame(labels, columns = ['Clusters'])
f_post_img_clus = f_post_drop.join(clus)

df =
pd.DataFrame(data={'x':f_post_drop['x'].tolist(),'y':f_post_drop['y'].tolist(
),'Clusters':labels})
mask_neg1 = (df['Clusters']>-1)
df_neg1=df[mask_neg1]
clus_num = int(max(df_neg1['Clusters'])+1)
x_mask_neg1 = df_neg1['x']
y_mask_neg1 = df_neg1['y']
clusters_mask_neg1 = df_neg1['Clusters']

fig = plt.figure(figsize=(10,8))
cmap = matplotlib.cm.get_cmap('rainbow', clus_num)
plt.scatter(x_mask_neg1, y_mask_neg1, s=5, c=clusters_mask_neg1, cmap = cmap)
plt.title('Number of Clusters = {}'.format(clus_num),fontsize=20)
plt.colorbar()

[out]:
```



A.2.3 Radial distribution function using particle centroids csv file (Python 3)

```
def csv_to_RDF(csv_infile,
               rmax=50, nbins=250, last_frames=1,
```

```
                pixel_conversion=None, distance_unit=None,
                save_file=None, overwrite=False,
                plot=True, save_plot_name=None, overwrite_plot=False, dpi=300,
                *args, **kwargs):

    data = pd.read_csv(csv_infile)

    n_particles = len(data)
    frames = np.unique(data.frame)
    n_frames = len(frames)
    positions = []
    Lxs, Lys, Lzs = [], [], []

    for frame in frames[-last_frames:]:
        particle_pos = data[list('xyz')].loc[(data.frame==frame)]
        positions.append(particle_pos.values)
        xys = np.array([particle_pos.values]*n_particles)
        ref_pos = np.array([[particle_pos.values[p]]*n_particles for p in
range(n_particles)])
        xys -= ref_pos
        Lx = xys[:,:,0].max()-xys[:,:,0].min()
        Lxs.append(Lx)
        Ly = xys[:,:,1].max()-xys[:,:,1].min()
        Lys.append(Ly)
        Lz = xys[:,:,2].max()-xys[:,:,2].min()
        Lzs.append(Lz)
    positions = np.array(positions)

    RDF_calculator=freud.density.RDF(bins=nbins, r_max=rmax)

    for f, pos in enumerate(positions):
        fbox = freud.box.Box(Lx=Lxs[f], Ly=Lys[f], Lz=Lzs[f])
        RDF_calculator.compute(system=(fbox, pos))

    rlabel = 'r ({dist_u})'.format(dist_u=distance_unit if distance_unit is
not None else 'a.u.')
    if not pixel_conversion:
        pixel_conversion = 1

    output = pd.DataFrame({rlabel: RDF_calculator.n_r*pixel_conversion,
'g(r)': RDF_calculator.rdf})

    if save_file is not None:
        if not os.path.exists(save_file):
            pandas_to_file(output, save_file, *args, **kwargs)
            print("Saved file to {}".format(save_file))
        elif overwrite:
            pandas_to_file(output, save_file, *args, **kwargs)
            print("Overwrote existing file at {}".format(save_file))
        else:
            print("Did not overwrite existing file at {}".format(save_file))

    return output
```

A.2.4 ψ_6 and Voronoi analysis (Python 3)

```
data_TrackMate = pd.read_csv(folder+cond+'.csv',
```

```
                                header=1, # header row number
                                usecols=[9,10,11,12,13], # import column number
                               )
data_TrackMate.columns = ['Particle_ID','Frame','X','Y','Z']

num_frames = np.max(data_TrackMate['Frame'])

new_table = []

for frame in range(num_frames+1): # (0,num_frames-1)

    # filter to only one frame
    table_frame = data_TrackMate[data_TrackMate['Frame']==frame]

    particle_position = table_frame[['X','Y','Z']].copy()
    particle_position.loc[:,['X']] = particle_position.loc[:,['X']] -
halfSize # center is 0
    particle_position.loc[:,['Y']] = -(particle_position.loc[:,['Y']] -
halfSize) # center is 0
    particle_position = np.array(particle_position)
    particle_position = particle_position.reshape((1,
particle_position.shape[0], particle_position.shape[1]))

    for f, pos in enumerate(particle_position):
        freudbox = freud.box.Box(Lx=size, Ly=size, Lz=0)
        #RDF_calculator.compute(system=(freudbox,pos))
        hex_order.compute(system=(freudbox,pos))

    # save data
    table_frame.loc[:,'Hexatic_Order'] = np.abs(hex_order.particle_order)
    table_frame.loc[:,'Hexatic_Real'] = np.real(hex_order.particle_order)
    table_frame.loc[:,'Hexatic_Imag'] = np.imag(hex_order.particle_order)
    table_frame.loc[:,'Hexatic_Angle'] = np.angle(hex_order.particle_order)
    new_table.append(table_frame)

new_table = pd.concat(new_table)

unfiltered_table = new_table
loc_yxz1 = unfiltered_table[['X','Y']]
corr_xyz_unfiltered_table = unfiltered_table
corr_xyz_unfiltered_table['X'] = loc_yxz1['X']-halfSize
corr_xyz_unfiltered_table['Y'] = -(loc_yxz1['Y']-halfSize)

threshold = 20/512*size
filter_mask = (corr_xyz_unfiltered_table['X']>=(-halfSize+threshold)) &
(corr_xyz_unfiltered_table['X']<=(halfSize-threshold)) &
(corr_xyz_unfiltered_table['Y']>=(-halfSize+threshold)) &
(corr_xyz_unfiltered_table['Y']<=(halfSize-threshold))
filtered_table = corr_xyz_unfiltered_table.loc[filter_mask]
border_particles = corr_xyz_unfiltered_table.loc[~filter_mask]


# Voronoi for multiple frames
systems = []
poly_list = []
loc_all = []
for idx in range(num_frames+1):
```

```
    unfiltered_corr_frame =
corr_xyz_unfiltered_table[corr_xyz_unfiltered_table['Frame']==idx]

    loc_xyz = unfiltered_corr_frame[['X','Y','Z']]
    loc_np = np.array(loc_xyz)
    loc_all.append(loc_np)

    box = freud.box.Box(Lx=size, Ly=size, is2D=True)
    points = box.wrap(loc_np)
    bp = (box,points)
    systems.append(bp)

voro = freud.locality.Voronoi()

for box, points in systems:
    voro.compute((box, points))
  poly_list.append(voro.polytopes)

def calc_Voronoi_property_all_frames(num_frames,corr_xyz_unfiltered_table):
    num_edge=[]
    poly_area=[]
    for polytopes in poly_list:
        num_edge_list = list([len(poly) for poly in polytopes])
        num_edge = num_edge+num_edge_list
        poly_area_list = list([shapely_Polygon(poly).area/pix_per_um**2 for
poly in polytopes])
        poly_area = poly_area+poly_area_list

    corr_xyz_unfiltered_table['Polygon_Edge']=num_edge
    corr_xyz_unfiltered_table['Polygon_Area']=poly_area
    return corr_xyz_unfiltered_table

def plot_voronoi_polygon_area_all_frames(systems,corr_xyz_unfiltered_table):
    for i in range(len(systems)):
        fig = plt.figure()
        ax = fig.subplots()
        polytopes = poly_list[i]

        # add to filter boundary
        unfiltered_frame =
corr_xyz_unfiltered_table[corr_xyz_unfiltered_table['Frame']==i]
        filter_mask2 = (unfiltered_frame['X']>=(-halfSize+threshold)) &
(unfiltered_frame['X']<=(halfSize-threshold)) & (unfiltered_frame['Y']>=(-
halfSize+threshold)) & (unfiltered_frame['Y']<=(halfSize-threshold))
        polytopes_filtered=list(compress(polytopes, filter_mask2))
        #num_edge = np.array([len(poly) for poly in polytopes_filtered])
        poly_area = np.array([shapely_Polygon(poly).area/pix_per_um**2 for
poly in polytopes_filtered])

        # Draw Voronoi polytopes
        patches = [Polygon(poly[:, :2]) for poly in polytopes_filtered]
        patch_collection = PatchCollection(patches, edgecolors="w", alpha=1)
        patch_collection.set_array(poly_area)
        patch_collection.set_cmap('plasma')
        patch_collection.set_clim(10, 15)

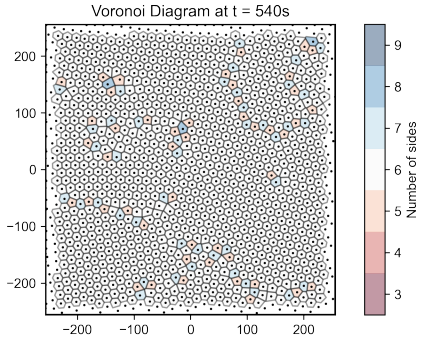
        ax.add_collection(patch_collection)
```

```
        # Draw box
        corners = [[0, 0, 0], [0, 1, 0], [1, 1, 0], [1, 0, 0]]
        # Need to copy the last point so that the box is closed.
        corners.append(corners[0])
        corners = box.make_absolute(corners)[:, :2]
        figpart1 = ax.plot(corners[:, 0], corners[:, 1], color="gray")
        points = systems[i][1]
        figpart2 = ax.scatter(points[:, 0], points[:, 1], s=0.5, c="gray")

        # Set title, limits, aspect
        #ax.set_title(f"Voronoi Diagram at t = {60*i}s")
        ax.set_xlim((np.min(corners[:, 0]), np.max(corners[:, 0])))
        ax.set_ylim((np.min(corners[:, 1]), np.max(corners[:, 1])))
        ax.set_aspect("equal", "datalim")

        # Add colorbar for number of sides

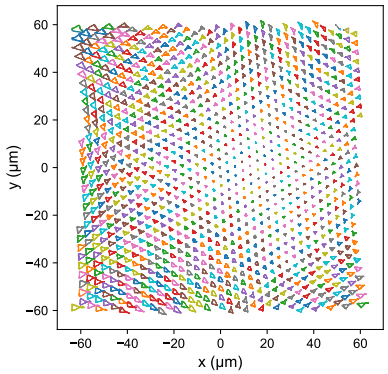
        ax_divider = make_axes_locatable(ax)
        cax = ax_divider.append_axes("right", size="7%", pad="10%")
        cb = Colorbar(cax, patch_collection)
        cb.set_label("Polygon Area (um*um)")
        #cb.set_ticks(bounds)
[out]:
```



A.2.5 Particle trajectory and average velocity (Python 3)

```
fig = plt.figure(figsize = (4.5,4.5))

for i in range(0,maxid+1):
    pid_frame =
corr_xyz_unfiltered_table[corr_xyz_unfiltered_table['Particle_ID']==i]
    if i in np.array(filtered_table['Particle_ID']):
        plt.plot(pid_frame['X'],pid_frame['Y'],linewidth=0.5)
plt.xlabel('x (\u03bcm)',fontsize=12)
plt.ylabel('y (\u03bcm)',fontsize=12)
[out]:
```




```
pid_array = corr_xyz_unfiltered_table['Particle_ID'].unique()

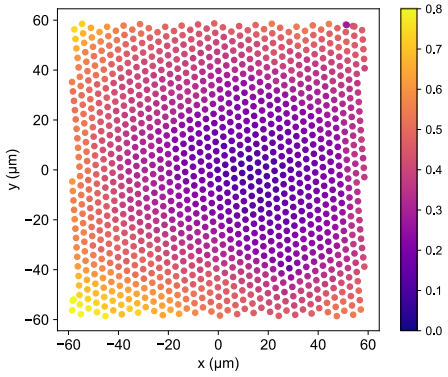
avg_vel = []
avg_X = []
avg_Y = []
incr = 10

for i in range(0,maxid+1):
    pid_frame =
corr_xyz_unfiltered_table[corr_xyz_unfiltered_table['Particle_ID']==i]
    Frame_array = np.array(pid_frame['Frame'])
    X_array = np.array(pid_frame['X'])
    Y_array = np.array(pid_frame['Y'])
    vel_list = []
    if len(Frame_array)-incr>end_frame:
        for j in range(0,end_frame):
            step_dis = ((X_array[j+incr]-X_array[j])**2+(Y_array[j+incr]-
Y_array[j])**2)**(1/2)
            step_vel = step_dis/(Frame_array[j+incr]-
Frame_array[j])*frame_rate
            vel_list.append(step_vel)
    else:
        for j in range(0,len(Frame_array)-incr):
            step_dis = ((X_array[j+incr]-X_array[j])**2+(Y_array[j+incr]-
Y_array[j])**2)**(1/2)
            step_vel = step_dis/(Frame_array[j+incr]-
Frame_array[j])*frame_rate
            vel_list.append(step_vel)
    avg_X.append(np.mean(X_array))
    avg_Y.append(np.mean(Y_array))
    avg_vel.append(np.mean(vel_list))

# filter boarder particles
xyvel = pd.DataFrame({'avg_X':list(avg_X), 'avg_Y':avg_Y, 'avg_vel':avg_vel})
xyvel_mask = (xyvel['avg_X']>=(-halfSize+threshold)) &
(xyvel['avg_X']<=(halfSize-threshold)) & (xyvel['avg_Y']>=(-
halfSize+threshold)) & (xyvel['avg_Y']<=(halfSize-threshold))
filtered_avg_vel = xyvel.loc[xyvel_mask]

fig = plt.figure()
ax = fig.add_subplot(111)
plt.scatter(filtered_avg_vel['avg_X'],filtered_avg_vel['avg_Y'],s=20,c=filter
ed_avg_vel['avg_vel'],vmin=0,vmax=0.8,cmap='plasma')
plt.colorbar()
plt.xlabel('x (\u03bcm)',fontsize=12)
```

```
plt.ylabel('y (\u03bcm)',fontsize=12)
ax.tick_params(axis='x', labelsize=12)
ax.tick_params(axis='y', labelsize=12)
ax.set_aspect('equal', adjustable='box')
```



A.2.6 Calculation of DEP force and active energy (MATLAB)

```
T_disp = T_disp_0;
theta = 0;
x0 = T_disp(:,2); y0 = T_disp(:,3); disp_x = T_disp(:,4); disp_y =
T_disp(:,5);

[x,y] = rotate_xy(theta,x0,y0,x_center,y_center); % rotate the x,y
conterclockwise
num_par = length(x0);
count = 0;
U_i = zeros(1,length(x));

for i = 1:num_par
    if ~isnan(disp_x(i))
        F_DEP_x0 = prf_Hz*prf_V*(4)*2*pi*a^3*eps_m*CM*sf_gradx(x(i)-
x_center,y(i)-y_center);
        F_DEP_y0 = prf_Hz*prf_V*(-4)*2*pi*a^3*eps_m*CM*sf_grady(x(i)-
x_center,y(i)-y_center);
        F_DEP_x(i) = F_DEP_x0*cos(theta) + F_DEP_y0*sin(theta);
        F_DEP_y(i) = F_DEP_x0*sin(-theta) + F_DEP_y0*cos(-theta);
        U_i(i) = (F_DEP_x(i)*disp_x(i)*10^-6+F_DEP_y(i)*disp_y(i)*10^-6);
    end
    count = count+1;
end

U_tot = sum(U_i);
U_avg = U_tot/count/kT
```

A.3 Optical spectrum from FDTD far field calculation

The codes included in this section import the MD simulated structure to Lumerical, compute the farfield response, and convert the intensity profile to optical spectrum.

A.3.1 Calculation of farfield intensity profile using MD simulated structure (Lumerical Scripting Language)

```
M = readdata("MD_structure.txt");
# M: (x,y,r)
imglength = 21.5;
r = 0.495e-6;
numpar = length(M(:,1));

addstructuregroup;
set("name","group1");
set("x",0);
set("y",0);
set("z",0);

for (i=1:numpar){
addsphere;
set("x",M(i,1)*1e-6);
set("y",M(i,2)*1e-6);
set("z",M(i,3)*1e-6);
set("radius",r);
set("material","PS");
addtogroup("group1");
}
```

A.3.2 Model structural color spectrum using farfield results (MATLAB)

```
function lumerical_farfield_to_spectrum
close all

load("farfield_by_FDTD.mat");
%note: the out matrix is in inverse order of the wavelength index

num_wave = 101;
frq = linspace(1/900,1/400,num_wave);
lambda = 1./frq;
theta = 30;%25:5:60; %deg
dphi = 1; %deg
phi = 0:dphi:360;
target_wavelength = 605;
loc = (900-target_wavelength)/5+1;
for k = 1:length(theta)
    angle = theta(k)
    for f = 1:num_wave
        r = length(out(:,:,f))/2*sin(deg2rad(angle));
        for i = 1:length(phi)
            x1 = r*sin(deg2rad(phi(i)));
            y1 = r*cos(deg2rad(phi(i)));
            x = length(out(:,:,f))/2+x1;
            y = length(out(:,:,f))/2+y1;
            I(i,1) = out(fix(y)+1,fix(x)+1,f);
        end
        meanI(f,k) = mean(I);
    end
end
```

Appendix B: Definitions and Units of Symbols

Symbols	Units	Physical meaning
A	V	Root-mean-square amplitude of AC electric field
A_H		Hamaker constant
a	m	Radius of a spherical particle
D	m	Interparticle separation
d	m	1-dimensional periodicity in grating or multilayer structure
E	V/m	DC electric field magnitude
E_{rms}	V	Root means square voltage of AC
$\boldsymbol{E}$	V	Position dependent AC voltage
e	C	Charge of electron, equal to 1.602×10^{-19} C
F	N	Force magnitude
$F(\boldsymbol{q})$		Mie Form factor
f	Hz	AC electric field frequency
g	m/s^2	Gravitational constant
$g(r)$		Radial distribution function
I		Light intensity
i	$\mu A \cdot cm^{-2}$	Applied current density or complex number
j		Particle index
k	m^{-1}	Wave vector or particle index
k_B	$J \cdot K^{-1}$	Boltzmann constant, equal to 1.38×10^{-23} J/K
l	m	Length
m		Diffraction order
N		Number of particles
n		Refractive index
n^0		Mean concentration of charge
Pe		Péclet number
p		p-value in statistics
$\mathrm{Re}\lvert K(\omega)\rvert$		Real part of Clausius-Mossotti factor
r	m	Distance from particle radius/surface
$\boldsymbol{S}$ *or* $\boldsymbol{S}^*$		Real or imaginary part of scattering matrix
$S(\boldsymbol{q})$		Static structure factor
T	K	Temperature or equivalent temperature
U		Coefficient of variation of light azimuthal intensity
u	m/s	Velocity of particle or fluid

V	J	Modeled particle pair potential
v	m/s	Average velocity of particle
W	J	Pair potential
W_a	J	Active energy injection by dielectrophoresis
x	m	Particle location in coordinates
y	m	Particle location in coordinates
z	m	Particle location in coordinates
$\langle \Delta r^2(\Delta t) \rangle$	m^2	Mean square displacement
$\delta_{6,j}$		Phase angle of six-fold bond orientational parameter of particle j
ε	$F \cdot m^{-1}$	Dielectric constant (absolute permittivity)
ε_o	$F \cdot m^{-1}$	Vacuum permittivity, equal to 8.854×10^{-12} $F \cdot m^{-1}$
ε_r		Relative permittivity of a material
ζ	mV	Zeta potential
η	Pa·s	Viscosity of liquid
κ^{-1}	m	Debye screening length
Π	Pa	Osmotic pressure
ρ	$kg \cdot m^{-3}$	Density
σ	S/m	Electrical conductivity
τ	s	Field cycling period
τ_{MW}	s	Maxwell-Wagner charge relaxation time
λ	m	Wavelength of light
θ	rad	Angle or polar angle of light
Φ		Volume fraction
ϕ	rad	Azimuthal angle of light
$\Psi_{6,j}$		Six-fold bond orientational parameter of particle j
ψ_s	V	Surface potential of colloidal particle
ψ_6		Global averaged hexatic order parameter
$\psi_{6,j}$		Local hexatic order parameter of particle j
ω	rad	Angular frequency of AC electric field

Bibliography

1. Bernardini, C., Stoyanov, S. D., Arnaudov, L. N. & Cohen Stuart, M. A. Colloids in Flatland: A perspective on 2D phase-separated systems, characterisation methods, and lineactant design. *Chem Soc Rev* **42**, 2100–2129 (2013).
2. Hiemenz, P. C. & Rajagopalan, R. *Principles of Colloid and Surface Chemistry, Revised and Expanded*. (CRC press, 2016).
3. Kim, J., Lee, D., Shum, H. C. & Weitz, D. A. Colloid surfactants for emulsion stabilization. *Advanced materials* **20**, 3239–3243 (2008).
4. Rathod, H. J. & Mehta, D. P. A review on pharmaceutical gel. *International Journal of Pharmaceutical Sciences* **1**, 33–47 (2015).
5. Larson, R. G. *The Structure and Rheology of Complex Fluids*. vol. 150 (Oxford university press New York, 1999).
6. Rueb, C. J. & Zukoski, C. F. Viscoelastic properties of colloidal gels. *J Rheol (N Y N Y)* **41**, 197–218 (1997).
7. Goerlitzer, E. S. A., Klupp Taylor, R. N. & Vogel, N. Bioinspired Photonic Pigments from Colloidal Self-Assembly. *Advanced Materials* **30**, 1706654 (2018).
8. Hassan, P. A., Rana, S. & Verma, G. Making Sense of Brownian Motion: Colloid Characterization by Dynamic Light Scattering. *Langmuir* **31**, 3–12 (2015).
9. Saud, K. T. & Solomon, M. J. Microdynamics of active particles in defect-rich colloidal crystals. *J Colloid Interface Sci* **641**, 950–960 (2023).
10. Poon, W. Colloids as Big Atoms. *Science (1979)* **304**, 830–831 (2004).
11. Piazza, R., Buzzaccaro, S. & Secchi, E. The unbearable heaviness of colloids: facts, surprises, and puzzles in sedimentation. *Journal of Physics: Condensed Matter* **24**, 284109 (2012).
12. Israelachvili, J. N. *Intermolecular and Surface Forces*. (Academic press, 2011).
13. Bard, A. J., Faulkner, L. R. & White, H. S. *Electrochemical Methods: Fundamentals and Applications*. (John Wiley & Sons, 2022).
14. Hoover, W. G. & Ree, F. H. Melting transition and communal entropy for hard spheres. *J Chem Phys* **49**, 3609 (1968).
15. Woodcock, L. V. Glass transition in the hard-sphere model and Kauzmann's paradox. *Ann. NY Acad. Sci* **371**, 274–298 (1981).
16. Liu, T., Vansaders, B., Glotzer, S. C. & Solomon, M. J. Effect of Defective Microstructure and Film Thickness on the Reflective Structural Color of Self-Assembled Colloidal Crystals. *ACS Appl Mater Interfaces* **12**, 9842–9850 (2020).
17. Liu, T., Liu, T., Gao, F., Glotzer, S. C. & Solomon, M. J. Structural Color Spectral Response of Dense Structures of Discoidal Particles Generated by Evaporative Assembly. *Journal of Physical Chemistry B* **126**, 1315–1324 (2022).

18. Shah, A. A., Ganesan, M., Jocz, J. & Solomon, M. J. Direct current electric field assembly of colloidal crystals displaying reversible structural color. *ACS Nano* **8**, 8095–8103 (2014).
19. Shah, A. A. *et al.* Liquid Crystal Order in Colloidal Suspensions of Spheroidal Particles by Direct Current Electric Field Assembly. *Small* **8**, 1551–1562 (2012).
20. Shah, A. A., Schultz, B., Zhang, W., Glotzer, S. C. & Solomon, M. J. Actuation of shape-memory colloidal fibres of Janus ellipsoids. *Nat Mater* **14**, 117–124 (2015).
21. Wang, M., He, L., Xu, W., Wang, X. & Yin, Y. Magnetic Assembly and Field-Tuning of Ellipsoidal-Nanoparticle-Based Colloidal Photonic Crystals. *Angewandte Chemie International Edition* **54**, 7077–7081 (2015).
22. Spatafora-Salazar, A., Lobmeyer, D. M., P Cunha, L. H., Joshi, K. I. & Lisa Biswal, S. Aligned colloidal clusters in an alternating rotating magnetic field elucidated by magnetic relaxation. **121**, (2024).
23. Park, J.-G. *et al.* Full-Spectrum Photonic Pigments with Non-iridescent Structural Colors through Colloidal Assembly. *Angewandte Chemie International Edition* **53**, 2899–2903 (2014).
24. Chen, M., Cölfen, H. & Polarz, S. Centrifugal field-induced colloidal assembly: From chaos to order. *ACS Nano* **9**, 6944–6950 (2015).
25. Li, J., Hill, E. H., Lin, L. & Zheng, Y. Optical nanoprinting of colloidal particles and functional structures. *ACS Nano* **13**, 3783–3795 (2019).
26. Chen, X., Lin, L., Li, Z. & Sun, H. Light-Directed Assembly of Colloidal Matter. *Adv Funct Mater* **32**, 2104649 (2022).
27. Menath, J. *et al.* Acoustic Crystallization of 2D Colloidal Crystals. *Advanced Materials* **35**, 2206593 (2023).
28. Katagiri, K. *et al.* Structural color coating films composed of an amorphous array of colloidal particles via electrophoretic deposition. *NPG Asia Mater* **9**, e355–e355 (2017).
29. Trau, M., Saville, D. A. & Aksay, I. A. Assembly of Colloidal Crystals at Electrode Interfaces. *Langmuir* **13**, 6375–6381 (1997).
30. Trau, M., Saville, D. A. & Aksay, I. A. Field-Induced Layering of Colloidal Crystals. *Science (1979)* **272**, 706–709 (1996).
31. Liu, T. & Solomon, M. J. Reconfigurable Grating Diffraction Structural Color in Self-Assembled Colloidal Crystals. *Small* **19**, 2301871 (2023).
32. Ferrar, J. A. & Solomon, M. J. Kinetics of colloidal deposition, assembly, and crystallization in steady electric fields. *Soft Matter* **11**, 3599–3611 (2015).
33. Kim, Y., Shah, A. A. & Solomon, M. J. Spatially and temporally reconfigurable assembly of colloidal crystals. *Nat Commun* **5**, (2014).
34. Lumsdon, S. O., Kaler, E. W. & Velev, O. D. Two-Dimensional Crystallization of Microspheres by a Coplanar AC Electric Field. *Langmuir* **20**, 2108–2116 (2004).
35. Mittal, M., Lele, P. P., Kaler, E. W. & Furst, E. M. Polarization and interactions of colloidal particles in ac electric fields. *Journal of Chemical Physics* **129**, 064513 (2008).
36. Oh, J., Hart, R., Capurro, J. & Noh, H. Comprehensive analysis of particle motion under non-uniform AC electric fields in a microchannel. *Lab Chip* **9**, 62–78 (2009).
37. Han, C.-H. & Jang, J. Integrated microfluidic platform with electrohydrodynamic focusing and a carbon-nanotube-based field-effect transistor immunosensor for continuous, selective, and label-free quantification of bacteria. *Lab Chip* **21**, 184–195 (2021).

38. Als-Nielsen, J. & McMorrow, D. *Elements of Modern X-Ray Physics*. (John Wiley & Sons, 2011).
39. Keim, P., Maret, G. & von Grünberg, H. H. Frank's constant in the hexatic phase. *Phys Rev E* **75**, 31402 (2007).
40. Chandler, D. & Percus, J. K. Introduction to modern statistical mechanics. Preprint at (1988).
41. Sorensen, C. M. Light scattering by fractal aggregates: a review. *Aerosol Science & Technology* **35**, 648–687 (2001).
42. Kao, P. K., VanSaders, B. J., Glotzer, S. C. & Solomon, M. J. Accelerated annealing of colloidal crystal monolayers by means of cyclically applied electric fields. *Sci Rep* **11**, 11042 (2021).
43. Kao, P. K., VanSaders, B. J., Durkin, M. D., Glotzer, S. C. & Solomon, M. J. Anisotropy effects on the kinetics of colloidal crystallization and melting: Comparison of spheres and ellipsoids. *Soft Matter* **15**, 7479–7489 (2019).
44. Engel, M. *et al.* Hard-disk equation of state: First-order liquid-hexatic transition in two dimensions with three simulation methods. *Phys Rev E* **87**, 42134 (2013).
45. Tang, X. *et al.* Optimal Feedback Controlled Assembly of Perfect Crystals. *ACS Nano* **10**, 6791–6798 (2016).
46. Romesburg, C. *Cluster Analysis for Researchers*. (Lulu. com, 2004).
47. Kaufman, L. & Rousseeuw, P. J. *Finding Groups in Data: An Introduction to Cluster Analysis*. (John Wiley & Sons, 2009).
48. Gao, F., Glaser, J. & Glotzer, S. C. The role of complementary shape in protein dimerization. *Soft Matter* **17**, 7376–7383 (2021).
49. Dshemuchadse, J., Damasceno, P. F., Phillips, C. L., Engel, M. & Glotzer, S. C. Moving beyond the constraints of chemistry via crystal structure discovery with isotropic multiwell pair potentials. *Proceedings of the National Academy of Sciences* **118**, e2024034118 (2021).
50. Wang, S. *et al.* The emergence of valency in colloidal crystals through electron equivalents. *Nat Mater* **21**, 580–587 (2022).
51. Lee, S., Vo, T. & Glotzer, S. C. Entropy compartmentalization stabilizes open host–guest colloidal clathrates. *Nat Chem* **15**, 905–912 (2023).
52. Salo-Ahen, O. M. H. *et al.* Molecular Dynamics Simulations in Drug Discovery and Pharmaceutical Development. *Processes* **9**, 71 (2021).
53. Anderson, J. A., Glaser, J. & Glotzer, S. C. HOOMD-blue: A Python package for high-performance molecular dynamics and hard particle Monte Carlo simulations. *Comput Mater Sci* **173**, 109363 (2020).
54. Hergert, W. & Wriedt, T. *The Mie Theory: Basics and Applications*. vol. 169 (Springer, 2012).
55. Lee, S. J., Kumar, S., Choi, J. W. & Lee, J. S. Coloration of colloidal polymer particles through selective extraction of Mie backscattering for cation-responsible colorimetric sensors. *J Colloid Interface Sci* **560**, 894–901 (2020).
56. Starr, C., Christine, A. E. & Lisa, S. *Biology: Concepts & Applications*. (Cengage Learning, 2018).
57. Li, Q. *et al.* Additive mixing and conformal coating of noniridescent structural colors with robust mechanical properties fabricated by atomization deposition. *ACS Nano* **12**, 3095–3102 (2018).

58. MacAdam, D. L. Subtractive color mixture and color reproduction. *JOSA* **28**, 466–480 (1938).
59. Britton, G. & Britton, G. *The Biochemistry of Natural Pigments*. (Cambridge University Press, 1983).
60. Siraj, N. *et al.* Fluorescence, Phosphorescence, and Chemiluminescence. *Anal Chem* **88**, 170–202 (2016).
61. Mao, Z. *et al.* Linearly Tunable Emission Colors Obtained from a Fluorescent–Phosphorescent Dual-Emission Compound by Mechanical Stimuli. *Angewandte Chemie* **127**, 6368–6371 (2015).
62. Kinoshita, S. & Yoshioka, S. Structural colors in nature: The role of regularity and irregularity in the structure. *ChemPhysChem* **6**, 1442–1459 (2005).
63. Kinoshita, S., Yoshioka, S. & Miyazaki, J. Physics of structural colors. *Reports on Progress in Physics* **71**, 076401 (2008).
64. Zhao, Y., Xie, Z., Gu, H., Zhu, C. & Gu, Z. Bio-inspired variable structural color materials. *Chem Soc Rev* **41**, 3297–3317 (2012).
65. Jana, S. *et al.* Aperiodic Bragg reflectors for tunable high-purity structural color based on phase change material. *Nano Lett* **24**, 3922–3929 (2024).
66. Yang, B. *et al.* Ultrahighly Saturated Structural Colors Enhanced by Multipolar-Modulated Metasurfaces. *Nano Lett* **19**, 4221–4228 (2019).
67. Vukusic, P. & Sambles, J. R. Photonic structures in biology. *Nature* **424**, 852–855 (2003).
68. Potyrailo, R. A. *et al.* Towards outperforming conventional sensor arrays with fabricated individual photonic vapour sensors inspired by Morpho butterflies. *Nat Commun* **6**, 7959 (2015).
69. Jia, Z. *et al.* Microstructural design for mechanical–optical multifunctionality in the exoskeleton of the flower beetle Torynorrhina flammea. *Proceedings of the National Academy of Sciences* **118**, e2101017118 (2021).
70. Zi, J. *et al.* Coloration strategies in peacock feathers. *Proceedings of the National Academy of Sciences* **100**, 12576–12578 (2003).
71. Williams, T. L. *et al.* Dynamic pigmentary and structural coloration within cephalopod chromatophore organs. *Nat Commun* **10**, 1004 (2019).
72. Teyssier, J., Saenko, S. V., Van Der Marel, D. & Milinkovitch, M. C. Photonic crystals cause active colour change in chameleons. *Nat Commun* **6**, 6368 (2015).
73. Fu, F., Shang, L., Chen, Z., Yu, Y. & Zhao, Y. Bioinspired living structural color hydrogels. *Sci Robot* **3**, 8580 (2018).
74. Wang, C., Lin, X., Schäfer, C. G., Hirsemann, S. & Ge, J. Spray Synthesis of Photonic Crystal Based Automotive Coatings with Bright and Angular-Dependent Structural Colors. *Adv Funct Mater* **31**, 2008601 (2021).
75. Nam, H., Song, K., Ha, D. & Kim, T. Inkjet Printing Based Mono-layered Photonic Crystal Patterning for Anti-counterfeiting Structural Colors. *Sci Rep* **6**, 30885 (2016).
76. Yang, W. *et al.* All-dielectric metasurface for high-performance structural color. *Nat Commun* **11**, 1864 (2020).
77. Chen, F. *et al.* Bio-inspired structural colors and their applications. *Chemical Communications* **57**, 13448–13464 (2021).
78. Faraji-Dana, M. *et al.* Compact folded metasurface spectrometer. *Nat Commun* **9**, 4196 (2018).

79. Parker, A. R. A vision for natural photonics. *Philosophical Transactions of the Royal Society of London. Series A: Mathematical, Physical and Engineering Sciences* **362**, 2709–2720 (2004).
80. Hsiung, B. K. *et al.* Rainbow peacock spiders inspire miniature super-iridescent optics. *Nat Commun* **8**, 2278 (2017).
81. Johansen, V. E. *et al.* Genetic manipulation of structural color in bacterial colonies. *Proceedings of the National Academy of Sciences* **115**, 2652–2657 (2018).
82. Kim, J. Bin, Lee, S. Y., Lee, J. M. & Kim, S. H. Designing Structural-Color Patterns Composed of Colloidal Arrays. *ACS Appl Mater Interfaces* **11**, 14485–14509 (2019).
83. Boys, C. V. *Soap Bubbles, Their Colours and the Forces Which Mold Them*. vol. 542 (Courier Corporation, 1959).
84. Lee, H. S., Shim, T. S., Hwang, H., Yang, S.-M. & Kim, S.-H. Colloidal Photonic Crystals toward Structural Color Palettes for Security Materials. *Chemistry of Materials* **25**, 2684–2690 (2013).
85. Schertel, L. *et al.* The Structural Colors of Photonic Glasses. *Adv Opt Mater* **7**, 1900442 (2019).
86. Sullivan, D. M. *Electromagnetic Simulation Using the FDTD Method*. (John Wiley & Sons, 2013).
87. Liu, F., Dong, B. Q., Liu, X. H., Zheng, Y. M. & Zi, J. Structural color change in longhorn beetles Tmesisternus isabellae. *Opt. Express* **17**, 16183–16191 (2009).
88. Lee, D. W. Ultrastructural basis and function of iridescent blue colour of fruits inElaeocarpus. *Nature* **349**, 260–262 (1991).
89. Srinivasarao, M. Nano-Optics in the Biological World: Beetles, Butterflies, Birds, and Moths. *Chem Rev* **99**, 1935–1961 (1999).
90. Lee, G. H., Sim, J. Y. & Kim, S. H. Polymeric Inverse Glasses for Development of Noniridescent Structural Colors in Full Visible Range. *ACS Appl Mater Interfaces* **8**, 12473–12480 (2016).
91. Xiao, M. *et al.* Investigating the trade-off between color saturation and angle-independence in photonic glasses. *Opt Express* **29**, 21212–21224 (2021).
92. Chen, F. *et al.* Superdurable and fire-retardant structural coloration of carbon nanotubes. *Sci Adv* **8**, 5882 (2022).
93. Kramer, R. M., Crookes-Goodson, W. J. & Naik, R. R. The self-organizing properties of squid reflectin protein. *Nat Mater* **6**, 533–538 (2007).
94. Ge, D. *et al.* A Robust Smart Window: Reversibly Switching from High Transparency to Angle-Independent Structural Color Display. *Advanced Materials* **27**, 2489–2495 (2015).
95. Kim, T. *et al.* Self-powered finger motion-sensing structural color display enabled by block copolymer photonic crystal. *Nano Energy* **92**, 106688 (2022).
96. Fan, W. *et al.* Iridescence-controlled and flexibly tunable retroreflective structural color film for smart displays. *Sci Adv* **5**, 8755 (2022).
97. Qin, M. *et al.* A Rainbow Structural-Color Chip for Multisaccharide Recognition. *Angewandte Chemie International Edition* **55**, 6911–6914 (2016).
98. Yuan, W., Zhou, N., Shi, L. & Zhang, K. Q. Structural Coloration of Colloidal Fiber by Photonic Band Gap and Resonant Mie Scattering. *ACS Appl Mater Interfaces* **7**, 14064–14071 (2015).
99. Gong, J. & Wu, N. Electric-Field Assisted Assembly of Colloidal Particles into Ordered Nonclose-Packed Arrays. *Langmuir* **33**, 5769–5776 (2017).

100. Luo, Y. *et al.* Electric field induced structural color changes of SiO2@TiO2 core–shell colloidal suspensions. *J. Mater. Chem. C* **2**, 1990–1994 (2014).
101. Cong, H. *et al.* Preparation of iridescent colloidal crystal coatings with variable structural colors. *Opt Express* **21**, 17831–17838 (2013).
102. Xu, M., Seago, A. E., Sutherland, T. D. & Weisman, S. Dual structural color mechanisms in a scarab beetle. *J Morphol* **271**, 1300–1305 (2010).
103. Halir, R. *et al.* Waveguide sub-wavelength structures: a review of principles and applications. *Laser Photon Rev* **9**, 25–49 (2015).
104. Tan, A. T. L. *et al.* In-Plane Direct-Write Assembly of Iridescent Colloidal Crystals. *Small* **16**, 1905519 (2020).
105. Vogel, N. *et al.* Color from hierarchy: Diverse optical properties of micron-sized spherical colloidal assemblies. *Proc Natl Acad Sci U S A* **112**, 10845–10850 (2015).
106. Fouquet, C. *et al.* Improving axial resolution in confocal microscopy with new high refractive index mounting media. *PLoS One* **10**, 0121096–0121096 (2015).
107. Piccolo, V. *et al.* 2D optical gratings based on hexagonal voids on transparent elastomeric substrate. *Micromachines (Basel)* **9**, 345 (2018).
108. Palmer, C. & Loewen, E. *DIFFRACTION GRATING HANDBOOK Sixth Edition*. http://www.newport.com/ (2005).
109. Loewen, E. G. & Popov, E. *Diffraction Gratings and Applications*. https://doi.org/10.1201/9781315214849 (1997).
110. Ding, H. *et al.* Responsive Colloidal Crystal for Spectrometer Grating. *ACS Photonics* **1**, 121–126 (2014).
111. Cao, Y. *et al.* Tunable Diffraction Gratings from Biosourced Lyotropic Liquid Crystals. *Advanced Materials* **32**, 1907376 (2020).
112. Zola, R. S. *et al.* Dynamic Control of Light Direction Enabled by Stimuli-Responsive Liquid Crystal Gratings. *Advanced Materials* **31**, 1806172 (2019).
113. Huang, S. Y., Huang, B. Y., Kang, C. C. & Kuo, C. T. Diffraction and polarization properties of electrically-tunable nematic liquid crystal grating. *Polymers (Basel)* **12**, 1929 (2020).
114. Lindquist, R. G. *et al.* High-resolution liquid-crystal phase grating formed by fringing fields from interdigitated electrodes. *Opt Lett* **19**, 670–672 (1994).
115. Schueller, O. J. A., Duffy, D. C., Rogers, J. A., Brittain, S. T. & Whitesides, G. M. Reconfigurable diffraction gratings based on elastomeric microfluidic devices. *Sens Actuators A Phys* **78**, 149–159 (1999).
116. Baek, K., Kim, Y., Mohd-Noor, S. & Hyun, J. K. Mie Resonant Structural Colors. *ACS Appl Mater Interfaces* **12**, 5300–5318 (2020).
117. Loose, W. & Ackerson, B. J. Model calculations for the analysis of scattering data from layered structures. *J Chem Phys* **101**, 7211–7220 (1994).
118. trackpy. http://soft-matter.github.io/trackpy/v0.5.0/ (2024).
119. Crocker, J. C. & Grier, D. G. Methods of Digital Video Microscopy for Colloidal Studies. *J Colloid Interface Sci* **179**, 298–310 (1996).
120. Barber, P. W. & Hill, S. C. *Light Scattering by Particles: Computational Methods*. *Advanced Series in Applied Physics* vol. Volume 2 (WORLD SCIENTIFIC, 1990).
121. Hwang, V. *et al.* Designing angle-independent structural colors using Monte Carlo simulations of multiple scattering. *Proceedings of the National Academy of Sciences* **118**, e2015551118 (2021).

122. Liu, T., Young, C.-M., Moore, T. C., Glotzer, S. C. & Solomon, M. J. Defect Structures in Colloidal Crystals and Their Effect on Grating Diffraction Structural Color. *ACS Appl Mater Interfaces* (2025) doi:10.1021/acsami.4c18558.
123. Mäthger, L. M., Denton, E. J., Marshall, N. J. & Hanlon, R. T. Mechanisms and behavioural functions of structural coloration in cephalopods. *J R Soc Interface* **6**, S149–S163 (2009).
124. Cao, X. *et al.* Replicating the Cynandra opis Butterfly's Structural Color for Bioinspired Bigrating Color Filters. *Advanced Materials* **34**, 2109161 (2022).
125. Li, Y. *et al.* Shear-Induced Assembly of Liquid Colloidal Crystals for Large-Scale Structural Coloration of Textiles. *Adv Funct Mater* **31**, 2010746 (2021).
126. Yu, Z., Wang, C.-F., Ling, L., Chen, L. & Chen, S. Triphase Microfluidic-Directed Self-Assembly: Anisotropic Colloidal Photonic Crystal Supraparticles and Multicolor Patterns Made Easy. *Angewandte Chemie International Edition* **51**, 2375–2378 (2012).
127. Zhu, Z. *et al.* Reduced Graphene Oxide Membrane Induced Robust Structural Colors toward Personal Thermal Management. *ACS Photonics* **6**, 116–122 (2019).
128. Foulger, S. H. *et al.* Photonic Crystal Composites with Reversible High-Frequency Stop Band Shifts. *Advanced Materials* **15**, 685–689 (2003).
129. Weissman, J. M., Sunkara, H. B., Tse, A. S. & Asher, S. A. Thermally Switchable Periodicities and Diffraction from Mesoscopically Ordered Materials. *Science (1979)* **274**, 959–963 (1996).
130. Wei, W., Zhang, Z., Wei, J., Li, X. & Guo, J. Phototriggered Selective Actuation and Self-Oscillating in Dual-Phase Liquid Crystal Photonic Actuators. *Adv Opt Mater* **6**, 1800131 (2018).
131. Xing, H., Li, J., Shi, Y., Guo, J. & Wei, J. Thermally Driven Photonic Actuator Based on Silica Opal Photonic Crystal with Liquid Crystal Elastomer. *ACS Appl Mater Interfaces* **8**, 9440–9445 (2016).
132. Zhang, H., Bu, X., Yip, S., Liang, X. & Ho, J. C. Self-Assembly of Colloidal Particles for Fabrication of Structural Color Materials toward Advanced Intelligent Systems. *Advanced Intelligent Systems* **2**, 190085 (2020).
133. Qian, W., Gu, Z. Z., Fujishima, A. & Sato, O. Three-dimensionally ordered macroporous polymer materials: An approach for biosensor applications. *Langmuir* **18**, 4526–4529 (2002).
134. Schöttle, M., Lauster, T., Roemling, L. J., Vogel, N. & Retsch, M. A Continuous Gradient Colloidal Glass. *Advanced Materials* **35**, (2023).
135. Zhang, J., Li, Y., Zhang, X. & Yang, B. Colloidal self-assembly meets nanofabrication: From two-dimensional colloidal crystals to nanostructure arrays. *Advanced Materials* **22**, 4249–4269 (2010).
136. Jiang, P. & McFarland, M. J. Large-Scale Fabrication of Wafer-Size Colloidal Crystals, Macroporous Polymers and Nanocomposites by Spin-Coating. *J Am Chem Soc* **126**, 13778–13786 (2004).
137. Cai, Z. *et al.* From colloidal particles to photonic crystals: advances in self-assembly and their emerging applications. *Chem Soc Rev* **50**, 5898–5951 (2021).
138. Hendley, R. S., Zhang, L. & Bevan, M. A. Multistate Dynamic Pathways for Anisotropic Colloidal Assembly and Reconfiguration. *ACS Nano* **17**, 20512–20524 (2023).
139. Yeh, S.-R., Seul, M. & Shraiman, B. I. Assembly of ordered colloidal aggregrates by electric-field-induced fluid flow. *Nature* **386**, 57–59 (1997).

140. Giersig, M. & Mulvaney, P. Preparation of ordered colloid monolayers by electrophoretic deposition. *Langmuir* **9**, 3408–3413 (1993).
141. Kotnala, A. & Zheng, Y. Digital Assembly of Colloidal Particles for Nanoscale Manufacturing. *Particle and Particle Systems Characterization* **36**, 1900152 (2019).
142. Solomentsev, Y., Böhmer, M. & Anderson, J. L. Particle Clustering and Pattern Formation during Electrophoretic Deposition: A Hydrodynamic Model. *Langmuir* **13**, 6058–6068 (1997).
143. Hayward, R. C., Saville, D. A. & Aksay, I. A. Electrophoretic assembly of colloidal crystals with optically tunable micropatterns. *Nature* **404**, 56–59 (2000).
144. Rogach, A. L., Kotov, N. A., Koktysh, D. S., Ostrander, J. W. & Ragoisha, G. A. Electrophoretic deposition of latex-based 3D colloidal photonic crystals: A technique for rapid production of high-quality opals. *Chemistry of Materials* **12**, 2721–2726 (2000).
145. Ganesan, M. & Solomon, M. J. High-density equilibrium phases of colloidal ellipsoids by application of optically enhanced, direct current electric fields. *Soft Matter* **13**, 3768–3776 (2017).
146. Fang, Y. *et al.* In Situ Dynamic Study of Color-Changing in Liquid Colloidal Crystals for Electrophoretic Displays. *ACS Appl Nano Mater* **5**, 11249–11261 (2022).
147. Ohnuki, R., Isoda, S., Sakai, M., Takeoka, Y. & Yoshioka, S. Grating Diffraction or Bragg Diffraction? Coloration Mechanisms of the Photonic Ball. *Adv Opt Mater* **7**, 1900227 (2019).
148. Vogel, N. *et al.* Color from hierarchy: Diverse optical properties of micron-sized spherical colloidal assemblies. *Proc Natl Acad Sci U S A* **112**, 10845–10850 (2015).
149. Liu, T., Vansaders, B., Keating, J. T., Glotzer, S. C. & Solomon, M. J. Effect of Particles of Irregular Size on the Microstructure and Structural Color of Self-Assembled Colloidal Crystals. *Langmuir* **37**, 13300–13308 (2021).
150. Allan, D. B., Caswell, T., Keim, N. C., der Wel, C. M. & Verweij, R. W. soft-matter/trackpy: Trackpy v0.5.0. https://doi.org/10.5281/zenodo.4682814 (2021) doi:10.5281/zenodo.4682814.
151. Ramasubramani, V. *et al.* freud: A software suite for high throughput analysis of particle simulation data. *Comput Phys Commun* **254**, 107275 (2020).
152. Bernard, E. P. & Krauth, W. Two-Step Melting in Two Dimensions: First-Order Liquid-Hexatic Transition. *Phys Rev Lett* **107**, 155704 (2011).
153. Rahmah, N. & Sitanggang, I. S. Determination of Optimal Epsilon (Eps) Value on DBSCAN Algorithm to Clustering Data on Peatland Hotspots in Sumatra. *IOP Conf Ser Earth Environ Sci* **31**, 12012 (2016).
154. Kim, Y., Jung, K., Cho, J. & Hyun, J. K. Realizing Vibrant and High-Contrast Reflective Structural Colors from Lossy Metals Supporting Dielectric Gratings. *ACS Nano* **13**, 10717–10726 (2019).
155. Lou, Z. *et al.* Exploring the structural color of micro-nano composite gratings with FDTD simulation and experimental validation. *Opt. Express* **32**, 2432–2451 (2024).
156. Higaki, T., Akita, K. & Katoh, K. Coefficient of variation as an image-intensity metric for cytoskeleton bundling. *Sci Rep* **10**, 22187 (2020).
157. van Blaaderen, A. & Wiltzius, P. Real-Space Structure of Colloidal Hard-Sphere Glasses. *Science (1979)* **270**, 1177–1179 (1995).

158. Zhang, L., Wang, W., Zheng, L., Wang, X. & Yan, Q. Quantitative Characterization of Mechanical Property of Annealed Monolayer Colloidal Crystal. *Langmuir* **32**, 451–459 (2016).
159. Ghosh, S., Saha, M. & De, S. K. Tunable surface plasmon resonance and enhanced electrical conductivity of in doped ZnO colloidal nanocrystals. *Nanoscale* **6**, 7039–7051 (2014).
160. Jangizehi, A., Schmid, F., Besenius, P., Kremer, K. & Seiffert, S. Defects and defect engineering in Soft Matter. *Soft Matter* **16**, 10809–10859 (2020).
161. Li, L. *et al.* Microscopic origins of the crystallographically preferred growth in evaporation-induced colloidal crystals. *Proceedings of the National Academy of Sciences* **118**, e2107588118 (2021).
162. Ramananarivo, S., Ducrot, E. & Palacci, J. Activity-controlled annealing of colloidal monolayers. *Nat Commun* **10**, 3380 (2019).
163. Baumgardner, W. J. *et al.* Pulsed Laser Annealing of Thin Films of Self-Assembled Nanocrystals. *ACS Nano* **5**, 7010–7019 (2011).
164. Zhang, J., Yang, J., Zhang, Y. & Bevan, M. A. Controlling colloidal crystals via morphing energy landscapes and reinforcement learning. *Sci. Adv* **6**, 6716 (2020).
165. Yakovlev, E. V *et al.* Tunable two-dimensional assembly of colloidal particles in rotating electric fields. *Sci Rep* **7**, 13727 (2017).
166. Tinevez, J.-Y. *et al.* TrackMate: An open and extensible platform for single-particle tracking. *Methods* **115**, 80–90 (2017).
167. Gavish, N. & Promislow, K. Dependence of the dielectric constant of electrolyte solutions on ionic concentration: A microfield approach. *Phys Rev E* **94**, 012611 (2016).
168. Kruželák, J., Kvasničáková, A., Hložeková, K. & Hudec, I. Progress in polymers and polymer composites used as efficient materials for EMI shielding. *Nanoscale Adv* **3**, 123–172 (2021).
169. Hueckel, T., Hocky, G. M. & Sacanna, S. Total synthesis of colloidal matter. *Nat Rev Mater* **6**, 1053–1069 (2021).
170. Yang, S.-M., Kim, S.-H., Lim, J.-M. & Yi, G.-R. Synthesis and assembly of structured colloidal particles. *J Mater Chem* **18**, 2177–2190 (2008).
171. Ferrar, J. A., Pavlovsky, L., Viges, E., Liu, Y. & Solomon, M. J. Two-step continuous production of monodisperse colloidal ellipsoids at rates of one gram per day. *AIChE Journal* **64**, 697–707 (2018).
172. Deng, T.-S. & Marlow, F. Synthesis of Monodisperse Polystyrene@Vinyl-SiO2 Core–Shell Particles and Hollow SiO2 Spheres. *Chemistry of Materials* **24**, 536–542 (2012).
173. Freitas, R. & Cao, Y. Machine-learning potentials for crystal defects. *MRS Commun* **12**, 510–520 (2022).
174. Lizano, A. & Tang, X. Convolutional neural network-based colloidal self-assembly state classification. *Soft Matter* **19**, 3450–3457 (2023).
175. Donev, A., Stillinger, F. H., Chaikin, P. M. & Torquato, S. Unusually Dense Crystal Packings of Ellipsoids. *Phys Rev Lett* **92**, 255506 (2004).
176. Singh, J. P., Lele, P. P., Nettesheim, F., Wagner, N. J. & Furst, E. M. One-and two-dimensional assembly of colloidal ellipsoids in ac electric fields. *Physical Review E—Statistical, Nonlinear, and Soft Matter Physics* **79**, 050401 (2009).